

1 **Enhanced metanephric specification to functional proximal tubule enables toxicity**
2 **screening and infectious disease modelling in kidney organoids**

3

4 Jessica M. Vanslambrouck^{1,2}, Sean B. Wilson^{1,2#}, Ker Sin Tan^{1#}, Ella Groenewegen¹, Rajeev
5 Rudraraju⁴, Jessica Neil⁴, Kynan T. Lawlor^{1,2}, Sophia Mah¹, Michelle Scurr¹, Sara E.
6 Howden^{1,2}, Kanta Subbarao⁴, Melissa H. Little^{1,2,3*}.

7

- 8 1. Murdoch Children's Research Institute, Flemington Rd, Parkville, VIC, Australia
9 2. Department of Paediatrics, The University of Melbourne, VIC, Australia.
10 3. Department of Anatomy and Neuroscience, The University of Melbourne, VIC, Australia.
11 4. Department of Microbiology and Immunology, The Peter Doherty Institute for Infection
12 and Immunity, The University of Melbourne, VIC, Australia.

13 [#] Equal contribution

14 * Author for correspondence:

15 M.H.L.: +61 3 9936 6206; melissa.little@mcri.edu.au

16

17 Running title: Enhanced proximal tubules

18 Keywords: proximal tubule, pluripotent stem cell, kidney organoid, nephron patterning

19

20

21 Abstract

22 While pluripotent stem cell-derived kidney organoids are now being used to model renal
23 disease, the proximal nephron remains immature with limited evidence for key functional
24 solute channels. This may reflect early mispatterning of the nephrogenic mesenchyme and/or
25 insufficient maturation. Here we show that enhanced specification to metanephric nephron
26 progenitors results in elongated and radially aligned proximalised nephrons with distinct S1 -
27 S3 proximal tubule cell types. Such PT-enhanced organoids possess improved albumin and
28 organic cation uptake, appropriate KIM-1 upregulation in response to cisplatin, and improved
29 expression of SARS-CoV-2 entry factors resulting in increased viral replication. The striking
30 proximo-distal orientation of nephrons resulted from localized WNT antagonism originating
31 from the organoid stromal core. PT-enhanced organoids represent an improved model to study
32 inherited and acquired proximal tubular disease as well as drug and viral responses.

33 **Introduction**

34 The proximal tubules (PTs) of the kidney represent a highly specialised portion of the
35 nephron performing the bulk of kidney reabsorption and secretion. This occurs via three
36 distinct functional and anatomical segments: the convoluted (S1 and S2) and the straight
37 (S3) segments that traverses the cortico-medullary boundary, with S1 exhibiting the highest
38 capacity for solute, sodium, amino acid, and fluid transport (Zhuo and Li, 2013). Their unique
39 roles and high metabolic activity render the PTs acutely vulnerable to toxins and metabolic
40 stress (Kirita, *et al.*, 2020). As such, accurately patterned and segmented PTs would represent
41 a critical tool for drug development, toxicology research, and studies of PT dysfunction.

42 We and others have established robust protocols for the directed differentiation of human
43 pluripotent stem cells to kidney (Freedman, *et al.*, 2015; Morizane, *et al.*, 2015; Taguchi and
44 Nishinakamura, 2017; Takasato, *et al.*, 2015; Toyohara, *et al.*, 2015). While these organoids
45 display a remarkable transcriptional similarity to the developing human kidney (Combes, *et*
46 *al.*, 2019; Howden, *et al.*, 2021; Subramanian, *et al.*, 2019; Wu, *et al.*, 2018), their nephron
47 patterning and segmentation remains immature, more closely resembling human trimester 1
48 fetal tissue (Takasato, *et al.*, 2015). PT maturation and functional segmentation is particularly
49 underdeveloped. Despite possessing nuclear HNF4A (responsible for driving early proximal
50 patterning [(Marable, *et al.*, 2020)]) and apical CUBILIN-MEGALIN complex expression,
51 organoid PTs lack a range of functional solute channels that define each PT subsegment (Wu,
52 *et al.*, 2018; Wilson, *et al.*, 2021). Expression levels of the principle water transporting channel,
53 AQP1, the organic anion transporters (OATs), and the organic cation transporters (OCTs) are
54 all low (Wilson, *et al.*, 2021).

55 Such suboptimal PT maturation may represent inappropriate anteroposterior/mediolateral
56 patterning, suboptimal maintenance of progenitor identity or incomplete maturation. In
57 response to distinct temporospatial signalling, the permanent (metanephric) kidney arises
58 during human embryogenesis as the final of three embryonic excretory organs, developing
59 sequentially from specific rostrocaudal regions of the intermediate mesoderm (Dressler, 2009).
60 Metanephric development, commencing during weeks 4 -5 of gestation, is preceded by the
61 formation of two more rostral transient organs; the pronephros (human gestation week 3 – 4)
62 and the mesonephros (human gestation week 4 – 10) (de Bakker, *et al.*, 2019). While the
63 mammalian pronephros is highly rudimentary, mesonephric nephrons also arise via MET and

64 show similar patterning and segmentation to early metanephric nephron. However, the
65 mesonephros possesses less definitive distal tubule segments and regresses around week 8
66 (Georgas, *et al.*, 2011; Mugford, *et al.*, 2008; Tiedemann, *et al.*, 1987).

67 Using fluorescent reporter lines and lineage tracing in human kidney organoids, we have
68 confirmed both the presence of a SIX2⁺ nephron progenitor population and the contribution of
69 these cells to nephrogenesis via MET in kidney organoids (Howden, *et al.*, 2019;
70 Vanslambrouck, *et al.*, 2019). However, the possibility exists that we are modelling
71 mesonephric rather than metanephric nephrogenesis, potentially contributing to poor PT
72 patterning and maturation (reviewed in (Little and Combes, 2019)). It is also possible that
73 suboptimal maintenance of progenitor identity during iPSC differentiation *in vitro* limits
74 nephron maturation. Several media have been described that are able to support the
75 maintenance of isolated nephron progenitors *in vitro* (Brown, *et al.*, 2015; Li, *et al.*, 2016;
76 Tanigawa, *et al.*, 2015; Tanigawa, *et al.*, 2016). While each media contains low levels of
77 canonical WNT activity and FGF2/9, distinct differences in nephron patterning result from the
78 inclusion of a variety of TGF β superfamily agonists (BMP4, BMP7, Activin A) and antagonists
79 (A83-01, LDN193189), NOTCH inhibition (DAPT), and other growth factors (TGF α , IGF1/2,
80 LIF). The inclusion of LDN193189 (inhibitor of BMP receptor-mediated SMAD1/5/8)
81 supported tubular patterning but not formation of glomeruli (Brown, *et al.*, 2015). In contrast,
82 the addition of LIF and either dual-SMAD inhibition (LDN193189 and A83-01) or NOTCH
83 inhibition (DAPT) resulted in the formation of nephrons with podocytes but different nephron
84 morphologies (Li, *et al.*, 2016; Tanigawa, *et al.*, 2016). Finally, while proximodistal nephron
85 patterning in mouse has previously been shown to be influenced by relative Wnt, Bmp, and
86 Notch signalling in mouse (Lindstrom, *et al.*, 2015), these data suggest that distinct nephron
87 progenitor states may show varying competence for different nephron segments, or that distinct
88 SIX2 populations give rise to different regions of the nephron.

89 In the current study, we sought to understand whether anteroposterior/mediolateral patterning,
90 or shifts in commitment state of the nephron progenitors, could influence ultimate PT identity
91 and maturation. Patterning to a posterior metanephric SIX2⁺ nephron progenitor population
92 by extending the duration of mesodermal patterning, while simultaneously enhancing nephron
93 progenitor expansion, specified progenitors with improved metanephric identity without
94 influencing anteroposterior/mediolateral patterning. These progenitors formed strongly
95 proximalised, elongated, and spatially aligned nephrons. The PTs within these nephrons

96 displayed distinct segmentation into S1, S2 and S3 cell types, upregulation of key solute
97 channels and transporters, and functional uptake of albumin and organic cations. Treatment
98 with cisplatin elicited upregulation of Kidney Injury Marker-1 (KIM-1), while increased
99 expression of key viral entry factors enabled improved SARS-CoV-2 infection and replication
100 compared to standard protocols. Notably, the striking nephron alignment was shown to result
101 from localised WNT antagonism, supporting a role for WNT gradients in human nephron
102 proximodistal patterning. Taken together, this study suggests a requirement for optimal
103 nephron progenitor commitment for appropriate PT identity. Such PT-enhanced kidney
104 organoids represent a model of the human proximal nephrons with likely applications for
105 infectious and genetic disease research, drug development, and nephrotoxicity evaluation.

106

107 **Results**

108 **Prolonged monolayer culture and delayed nephron induction supports nephron
109 progenitors**

110 As noted previously, optimisation of nephron progenitor maintenance *in vitro* has been
111 investigated by a range of studies using murine and human pluripotent stem cell-derived
112 nephron progenitors (Brown, *et al.*, 2015; Li, *et al.*, 2016; Tanigawa, *et al.*, 2016). While all
113 studies reported maintenance of nephron progenitors, variations were evident with respect to
114 the final patterning of resulting nephrons following induction. Given the clear influence that
115 initial differentiation conditions and timing can have on nephron progenitor survival and
116 subsequent nephron patterning, we hypothesised that expanding our nephron progenitor
117 population whilst delaying nephron initiation may create a more metanephric population
118 leading to organoids with improved patterning and PT maturation. We have previously shown
119 that SIX2 expression is not detected until day 10 of pluripotent stem cell differentiation
120 (Howden, *et al.*, 2019). Hence, the initial monolayer differentiation phase was prolonged to
121 between 12 – 14 days, along with culture in either of two previously defined nephron progenitor
122 (NP) maintenance media, NPSR (Li, *et al.*, 2016) and CDBLY (Tanigawa, *et al.*, 2016) from
123 day 7, which represents the point of intermediate mesoderm commitment (Takasato, *et al.*,
124 2015; Takasato, *et al.*, 2014) (Figure 1A). Compared to control media (TeSR-E6; E6), both
125 NPSR and CDBLY prevented spontaneous epithelialisation of the monolayer (Figure 1B).
126 However, very little epithelialisation and poor nephron commitment was observed after culture
127 in NPSR (Figure 1B). In contrast, CDBLY preserved the nephron-forming capacity of the
128 progenitor cells following their formation into a micromass and induction of nephrogenesis
129 with a pulse of canonical WNT signalling (Figure 1B). Nephrons of these organoids were also
130 observed to surround a stromal core region that stained positive for markers of kidney stroma
131 MEIS1/2/3 and SNAI2 (SLUG) (Supplementary Figure 1A) (England, *et al.*, 2020). Upon
132 prolonged organoid culture (> 14 days), portions of this core region formed patches of Alcian
133 blue-positive cartilage (Supplementary Figure 1B).

134 The prevention of spontaneous differentiation while preserving the nephrogenic capacity of the
135 NP cells was found to be primarily a response to the presence of CDB (CHIR, DAPT, BMP7),
136 with omission of LIF, Y27632, as well as the basal media component TGF α , found to produce
137 a similar result with respect to growth, morphology and nephron segmentation compared to

138 CDBLY (Figure 1C). The inhibition of monolayer epithelialisation with preserved nephrogenic
139 capacity was found to be consistent at monolayer differentiation lengths tested (10, 12, 13 and
140 14 days) (Supplementary Fig 1C). However, a monolayer differentiation length of 12 – 13 days
141 produced more consistent nephrogenesis between experiments, with 14 days observed to cause
142 frequent detachment of the differentiating monolayer. Subsequent studies proceeded using
143 prolonged culture in CDBLY noting the inclusion of an increased concentration of BMP7
144 (10ng/mL; CDBLY2) which improved the consistency of nephrogenesis between organoids
145 compared to standard CDBLY (5ng/mL BMP7) (Supplementary Figure 1D). This modified
146 differentiation protocol is detailed in Figure 1A.

147 Quantitative RT-PCR (qRT-PCR) of the extended monolayer differentiations in CDBLY2
148 confirmed an improved metanephric gene expression profile compared to standard
149 differentiations performed in parallel (7 day protocol in E6 (Howden, *et al.*, 2019; Takasato, *et*
150 *al.*, 2016)) (Figure 1D). Extended CDBLY2 monolayers showed a significant increase in
151 *SIX1/SIX2* (self-renewing to committed NPs) and *WNT4* (primed to committed NPs), while
152 *DAPL1* (self-renewing and primed NPs) was increased without significance and no change was
153 observed in *TMEM100* (self-renewing NPs). This suggested that the extended protocol
154 promotes a primed/committed, rather than self-renewing, NP population (Hochane, *et al.*,
155 2019; Lindstrom, *et al.*, 2018; Lindstrom, *et al.*, 2018). Extended differentiation in CDBLY2
156 was not found to alter mediolateral patterning, with no change in paraxial mesodermal marker
157 *PARAXIS* and unchanged or increased expression of intermediate mesoderm markers *HOXD11*
158 and *LHX1* (Mugford, *et al.*, 2008) (Figure 1D).

159 **Extended monolayer culture induces SIX2-derived proximalised nephrons**

160 Lineage tracing studies in mouse have shown that nephrons are derived entirely from Six2+
161 nephron progenitors (Kobayashi, *et al.*, 2008), with histological studies suggesting a similar
162 developmental process in human (Lindstrom, *et al.*, 2018; Lindstrom, *et al.*, 2018) (Kobayashi,
163 *et al.*, 2008). Using a *SIX2*^{Cre/Cre}:GAPDH^{dual} lineage tracing line, in which SIX2 expression
164 induces a permanent GFP/mCherry switch, we have previously shown that kidney organoid
165 nephrons contain cells derived from *SIX2*⁺, but also *SIX2*⁻, progenitor cells, resulting in a
166 chimeric appearance (Howden, *et al.*, 2019). To confirm and compare the competence of the
167 metanephric progenitor-enriched monolayer differentiation to contribute to nephron formation,
168 organoids were generated from both our standard protocol and the extended differentiation

169 protocol using the SIX2^{Cre/Cre}:GAPDH^{dual} lineage tracing line. Immunofluorescence re-
170 confirmed the chimeric contribution of SIX2⁺ and SIX2⁻ progenitor-derived cells to standard
171 organoid nephrons as shown previously (Howden, *et al.*, 2019) (Figure 2A). However, confocal
172 imaging suggested a larger contribution of SIX2⁺ cells to proximal nephrons in organoids
173 derived from the extended protocol compared to the standard protocol (7 days differentiation,
174 cultured in E6) (Howden, *et al.*, 2019), including contribution to NPHS1⁺ podocytes, LTL⁺
175 PTs, and to a lesser extent E-CADHERIN⁺ distal tubules (Figure 2A). To quantitatively
176 compare the contributions SIX2-derived cells to nephrons, dissociated SIX2^{Cre/Cre}:GAPDH^{dual}
177 standard and extended organoids (expressing endogenous SIX2-mCherry) were co-stained
178 with EPCAM to mark both proximal and distal nephron epithelium, then analysed via flow
179 cytometry (Figure 2Bi). In agreement with confocal imaging, SIX2-derived cell contribution
180 to EPCAM⁺ nephrons was significantly higher in organoids derived from the metanephric
181 progenitor-enriched extended monolayers compared to those derived from the standard 7 day
182 protocol in E6 media, suggesting improved metanephric identity of prolonged monolayers
183 exposed to CDBLY2 (Figure 2Bii).

184 The segmentation of nephrons within organoids derived from the extended protocol was
185 examined using a range of markers for podocytes, proximal, and distal tubules, revealing
186 distinct proximo-distal segmentation (Figure 2Ci). In contrast to the standard protocol which
187 produced organoids with a branching GATA3⁺ epithelium (Figure 2D), extended protocol-
188 derived organoids possessed few structures expressing the ureteric epithelium marker GATA3
189 (Figure 2Cii). The distribution of glomeruli, marked by NPHS1⁺ podocytes, also differed
190 between protocols, with extended protocol-derived organoids possessing a central ring of
191 glomeruli and elongated PTs radiating outwards that starkly opposed the more homogenous
192 distribution of these structures in standard organoids (Figure Ci and D). This unique organoid
193 morphology was observed in organoids derived from 6 different iPSC lines with or without
194 gene editing and from male or female iPSC sources (3 examples evidenced in Supplementary
195 Figure 1E).

196 In addition to differences in the segmentation of nephrons, organoids derived via extended
197 differentiation in CDBLY2 appeared to possess a larger proportion of LTL- and HNF4A-
198 positive PT compared to standard organoids (Figure 2Ci, Figure 2D, and Figure 3A). To
199 quantify and compare the proportion of PT cells in organoids derived from these two protocols,
200 organoids were generated using the HNF4A^{YFP} iPSC reporter line which reports the formation

201 of PT (Vanslambrouck, *et al.*, 2019) (Figure 3Bi). Flow cytometry revealed up to 6.2 times
202 higher average proportions of HNF4A^{YFP+} PT cells in organoids derived from the extended
203 monolayer protocol compared to the standard protocol (Figure 3Bii), confirming the use of
204 extended monolayer differentiation combined with progenitor-supportive media, CD63LY2, as
205 an effective method of generating proximal tubule-enhanced (PT-enhanced) kidney organoids.

206 **PT-enhanced organoids show improved proximal tubule patterning and maturation at
207 both a protein and gene level**

208 To establish the level of PT maturation within enhanced organoids, the expression and cellular
209 localisation of functionally important brush border membrane proteins and markers,
210 characteristic of mature PTs, were assessed via immunofluorescence (Figure 3C). Within LTL-
211 positive PTs, enhanced organoids showed strong expression of the protein transport complex
212 CUBILIN-MEGALIN (CUBN-MEG) and neutral amino acid transporter SLC6A19, with all
213 transporters displaying a highly-specific apical brush border membrane localisation (Figure
214 3Ci-ii). In contrast, the PTs of standard organoids possessed weaker and diffuse staining of the
215 CUBN-MEG complex (Figure 3Di). Furthermore, the majority of standard organoids lacked
216 SLC6A19 expression, with staining observed in just one of three independent experiments
217 (representative images in Figure 3Dii and Supplementary Figure 2A). Additional information
218 regarding the maturity of PT brush border membranes was afforded by high-resolution imaging
219 of LTL binding. LTL is a fucose-specific lectin widely used in the kidney field owing to its
220 high-affinity binding to α-linked L fucose-containing oligosaccharides of glycoconjugates that
221 abundantly line the brush border membrane of kidney PT cells (Hennigar, *et al.*, 1985). High-
222 resolution imaging of PTs within enhanced organoids showed LTL binding was highly
223 restricted to the apical membrane where it co-localised with SLC6A19, a characteristic of
224 correctly polarised, mature PT brush-border membranes (Supplementary Figure 2A). In
225 contrast, the PTs of standard organoids possessed LTL staining that was not highly apically-
226 restricted and instead diffuse throughout the PT, even in the instance where apical SLC6A19
227 was detected (Figure 2Dii and Supplementary Figure 2A). Taken together, these data suggested
228 a more immature PT phenotype and suboptimal brush border membrane development in
229 standard compared to enhanced organoids.

230 To provide a more comprehensive comparison with existing kidney organoid differentiation
231 protocols, as well as to gain a deeper insight into the complexity and maturity of cells derived

232 from the extended protocol, multiplexed single cell RNA sequencing (scRNAseq) with
233 antibody-based cell barcoding was performed on both monolayer (day 13) and resulting PT-
234 enhanced organoids (Figure 4). To account for variation, libraries were created from 4 separate
235 differentiated monolayers representing distinct starting pools of iPSCs (CRL1502.C32) that
236 were used to generate 4 separate batches of organoids (Figure 4A). Cells from the 4 replicates
237 (both at day 13 [D13] monolayer stage, prior to organoid formation, and day 14 of organoid
238 culture [D13+14]) were barcoded using hashing antibodies before being pooled. This approach
239 produced a single library for each timepoint (sample) which could be later deconvoluted to
240 retrieve replicate information.

241 The resulting D13 and D13+14 pooled replicate libraries resolved 19,956 and 15,852 individual
242 cell transcriptomes per timepoint, respectively. UMAP plots showed the resolution of distinct
243 clusters for both D13 monolayers and resulting PT-enhanced (D13+14) organoids (Figure 4B).
244 Gene expression analyses confirmed the expression of a range of markers for mesenchymal
245 cell states pre-kidney organogenesis in D13 monolayers, as well as markers of proximodistal
246 patterning, stroma, and endothelium in D13+14 organoids (Supplementary Figure 2BC and
247 Supplementary Tables 1 - 2). To enable unbiased comparisons of kidney cell types and gene
248 expression levels between D13/D13+14 samples, published stem cell-derived, and reference
249 reference human kidney datasets, datasets were analysed using the *DevKidCC* package
250 (Wilson, *et al.*, 2021). *DevKidCC* enables robust classification of novel developing human or
251 stem cell-derived kidney organoid datasets without the need for integration or prior
252 dimensional reduction or clustering. Using the *ComparePlot* function, kidney cell proportions
253 in D13 and D13+14 samples were directly compared, confirming distinct differences in cell
254 populations yet consistency between the 4 replicates within each sample (Figure 4C and
255 Supplementary Figure 3A). As anticipated, over 90% of cells within the D13 monolayer
256 differentiations were classified as nephron progenitor cells (NPC) or NPC-like, with a small
257 contribution of cells classified as early nephron (EN) (Figure 4C). In contrast, D13+14
258 organoids possessed a range of proximal, distal, and renal corpuscle cell types. Early proximal
259 tubule (EPT) formed the largest proportion of organoid nephron cell types (51% average across
260 4 samples), while two replicates possessed a small (<5%) fraction of maturing PT cells. By
261 contrast, previous studies of the standard organoid protocol show on average <25% EPT and
262 no PT (Takasato, *et al.*, 2015).

263 *DevKidCC* was next used to compare cell type-specific markers in D13 / D13+14 samples to
264 published stem cell-derived and reference human fetal kidney datasets (Figure 4DE). Analysis
265 of the NPC population within D13 samples confirmed strong gene signatures for committed
266 NPCs (*SIX1*, *SIX2*, and *LYPD1*) and the metanephric HOX code (*HOXC10/11*, *HOXA11*, and
267 *HOXD11*) compared to relevant published monolayer and nephrogenic-stage differentiations
268 (Subramanian, *et al.*, 2019; Wu, *et al.*, 2018; Low, *et al.*, 2019; Tran, *et al.*, 2019) that better
269 emulated the mixed reference dataset of human fetal kidneys (weeks 11, 13, 16, 18) (Hochane,
270 *et al.*, 2019; Tran, *et al.*, 2019; Holloway, *et al.*, 2020). PT-enhanced organoids derived from
271 these D13 monolayer differentiations possessed high and abundant expression of a range of
272 proximal nephron markers in their EPT population (Figure 4E). These included genes encoding
273 several membrane proteins critical for PT transport of proteins and amino acids (*CUBN*, *LRP2*,
274 *SLC3A1*, and *SLC3A2*), as well as auxiliary proteins and transcription factors required for
275 transporter regulation and functionality, such as *AMN*, *AGT*, and *HNF4A*. This gene signature
276 showed remarkable congruence to reference human fetal kidney and improved PT identity
277 compared to existing published kidney organoid datasets (Czerniecki, *et al.*, 2018; Harder, *et*
278 *al.*, 2019; Kumar, *et al.*, 2019) (Figure 4E).

279 An important anatomical feature of the mature PT is its segmentation into functionally and
280 morphologically distinct regions defined as the S1/S2 convoluted tubule segments and the S3
281 straight segment. In addition to differences in proliferation characteristics and protein
282 synthesis, the convoluted and straight segments display distinct differences in solute handling
283 to accommodate the declining concentration of solutes as the ultrafiltrate passes through the
284 nephron (Zhuo and Li, 2013; Avissar, *et al.*, 1994). As such, early S1 – S2 convoluted segments
285 express low-affinity/high-capacity transporters, with a gradual transition to high-affinity/low-
286 capacity transporters in the later S3 straight segment (Palacin, *et al.*, 2001; Schuh, *et al.*, 2018;
287 Verrey, *et al.*, 2005). To determine whether the PTs of enhanced organoids show evidence of
288 this segmentation, PT clusters from the 4 integrated D13+14 replicate datasets were isolated
289 and re-clustered, resolving 4740 PT cells across 6 distinct clusters (Supplementary Figure 3B).
290 The PT population was analysed for the expression of segment-specific PT markers with
291 critical functional roles, including solute carriers for ions (*SLC34A1/NPT2* (Fenollar-Ferrer, *et*
292 *al.*, 2015) expressed in S1>S2), glucose (*SLC2A2/GLUT2* and *SLC5A2/SGLT2* expressed in
293 S1>S2; *SLC2A1/GLUT1* and *SLC5A1/SGLT1* expressed in S2<S3 (Hummel, *et al.*, 2011;
294 Rahmoune, *et al.*, 2005; Wood and Trayhurn, 2003)), amino acids (*SLC7A9/b(0,+)*AT
295 transporter of cystine, aspartate, and glutamate expressed in S1/S2 > S3 (Nagamori, *et al.*,

296 2016), and cationic drugs/toxins (*SLC47A1/MATE1* expressed in S1/S2 > S3 (Otsuka, *et al.*,
297 2005)), as well as *AKAP12* (involved in cell cycle regulation, expressed in S2<S3 (Vogetseder,
298 *et al.*, 2008) and *GPX3* (glutathione peroxidase; secreted antioxidant synthesised in S1/S2>S3
299 (Avissar, *et al.*, 1994)) (Supplementary Figure 3C). UMAP plots revealed the largely opposing
300 distributions of cells expressing S1>S2 and S2>S3 gene signatures (Supplementary Figure 3C).
301 Cells expressing S1>S2 convoluted PT markers (*SLC34A1/MATE1*, *SLC2A2/GLUT2*, and
302 *SLC5A2/SGLT2*) were predominantly located in clusters 0, 3, and the lower portion of cluster
303 4, whereas cells expressing S2<S3 straight PT markers (*AKAP12*, *SLC2A1/GLUT1*, and
304 *SLC5A1/SGLT1*) were primarily within clusters 1, 2, and the upper portion of cluster 4. When
305 analysed for markers that exhibit a gradient of expression along the length of the nephron
306 (S1/S2>S3), UMAP plots for each gene revealed a similar graded expression pattern, with a
307 higher concentration of positive cells within the S1>S2 cluster (0) and decreasing in prevalence
308 within S2<S3 clusters (0, 2) (Supplementary Figure 3C). Together this suggested that, despite
309 the low expression of some markers indicating PT immaturity, the PTs of enhanced kidney
310 organoids show evidence of separation into the 3 anatomically distinct PT segments.

311 Comparison between organoids is confounded by the inherent variability of different organoid
312 protocols, technical variables, and individual cell line characteristics. To minimise potential
313 bias when comparing cell maturation, PT-enhanced organoid scRNASeq data were compared
314 to an existing standard organoid dataset derived from the same iPSC line and of equivalent
315 organoid age (Howden, *et al.*, 2019). Libraries from the PT-enhanced and standard organoid
316 samples resolved 6737 and 1879 cells, respectively. Datasets were integrated prior to quality
317 control measures to enable direct comparison of PT maturation and UMAP plots confirmed the
318 resolution of distinct kidney cell clusters for both samples (Supplementary Figure 3D). Violin
319 plots of the PT cluster alone in integrated datasets confirmed that the PT-enhanced organoid
320 dataset possessed higher and more abundant expression of genes critical for PT functionality
321 compared to the standard organoid (Figure 4FG). Examples included genes encoding
322 membrane transporters CUBILIN/CUBN and MEGALIN/LRP2 (important for protein uptake
323 (Nielsen, *et al.*, 2016), heavy-chain subunit solute carriers rBAT/*SLC3A1* and 4F2/*SLC3A2*
324 (required for heteromer formation and amino acid transport by SLC7 family members
325 (Kowalcuk, *et al.*, 2008), light-chain subunit solute carriers y+LAT-1/*SLC7A7* and
326 LAT2/*SLC7A8* (responsible for regulating intracellular amino acid pool via basolateral efflux
327 of basic and neutral amino acids for transport systems y+L and L, respectively (Kanai, *et al.*,
328 2000; Verrey, 2003), and solute carriers critical for PT metabolism and drug transport

329 (G6PT1/*SLC37A4* and MATE1/*SLC47A1* (Lee, *et al.*, 2015) (Figure 4F). Several auxiliary
330 proteins essential for correct apical localisation and transporter functionality also showed
331 higher expression in the PT-enhanced dataset, including *AMN* (Amnionless), *ACE2*, and
332 *TMEM27* (Collectrin) (Kowalcuk, *et al.*, 2008; Camargo, *et al.*, 2009; Fyfe, *et al.*, 2004;
333 Ahuja, *et al.*, 2008) (Figure 4G). Expression of genes encoding drug transporters *SLC22A2*
334 (OCT2) and *SLC22A6* (OAT1) were low in both conditions but increased in PT-enhanced
335 compared to standard organoids (Supplementary Figure 3E).

336 To investigate PT maturation further, an unbiased ToppFun GO Molecular Function analysis
337 was performed on genes that were significantly differentially expressed within the PT cluster
338 of PT-enhanced compared to standard organoids (945 input genes). This analysis revealed key
339 differences in genes involved in cell metabolism (Supplementary Figure 3F). PT-enhanced
340 organoid cells within the PT cluster showed increased expression of genes related to fatty acid
341 metabolism and its regulation, such as *PPARG*, *FABP3*, *PRKAA2*, and *FAT1* (Supplementary
342 Figure 3G). Given the known reliance of mature PT cells on fatty acid metabolism *in vivo*
343 (reviewed in (Zhuo and Li, 2013), this gene signature was suggestive of a more mature
344 metabolic profile in enhanced compared to standard organoid PT cells.

345 Together, these comprehensive scRNAseq analyses confirmed an increased abundance and
346 relative maturation of PT within this extended protocol. Analyses of D13 monolayers suggests
347 this higher-order PT patterning arises from improved NPC identity at the point of metanephric
348 specification.

349 **Radial nephron patterning and alignment is associated with localised stroma-associated
350 WNT antagonism**

351 Of interest was the characteristic radial patterning observed in all PT-enhanced organoids,
352 where tubules align with their glomeruli towards the centre of the organoid, surrounding a
353 central core region, and distal SLC12A1+ segments towards the organoid periphery (refer to
354 Figure 2C). This orientation was suggestive of a directional patterning cue emanating from the
355 core region, shown earlier to express stroma marker proteins MEIS1/2/3 and SNAI2
356 (Supplementary Figure 1A). Previous studies have not only suggested a role of
357 interstitial/stromal populations in nephron differentiation (England, *et al.*, 2020; Das, *et al.*,
358 2013), but have also indicated proximo-distal patterning is controlled by Wnt/β-catenin

359 signalling along the nephron axis, with lower WNT signalling leading to improved formation
360 and maturation of the proximal nephron (Lindstrom, *et al.*, 2015). In agreement with this, WNT
361 inhibition has been observed to promote podocyte commitment in PSC cultures (Yoshimura,
362 *et al.*, 2019). These findings suggested that the central core of PT-enhanced organoids may
363 possess stromal populations influencing nephron patterning and/or express a localised WNT
364 antagonist leading to directional signalling cues.

365 PT-enhanced scRNAseq datasets classified by *DevKidCC* were re-analysed to examine the
366 stromal populations at greater depth. In addition to nephron-related and endothelial
367 populations, previous classification of D13+14 organoids identified 48.2% of cells as stroma
368 (enriched for *CRABP1*, *COL3A1*, *COL1A1*, *COL1A2* and *CXCL12*) and 23.8% of cells as
369 unassigned but similarly enriched for collagens (e.g., *COL2A1* and *COL9A1*) (Supplementary
370 Figure 3A). Further analyses of D13+14 populations for defined markers of stromal zones
371 curated in mouse kidney (England, *et al.*, 2020) revealed the stromal cells of PT-enhanced
372 organoids were most like those of kidney cortex (Figure 5Ai). High expression of cortical
373 stroma (CS) markers, including *FIBN*, *DLK1*, *MEIS1/2*, and *SNAI2*, were observed
374 predominantly in the unassigned, stroma, and NPC-like subsets, while medullary stroma and
375 stromal progenitor markers were largely absent (Figure 5Ai). Unassigned and stroma clusters
376 also highly expressed the WNT antagonist Secreted Frizzled-Related Protein-2 (*SFRP2*) and
377 developing cartilage markers (*ONG*, *MGP*, and *COL2A1*) that been previously identified in
378 mouse kidney stromal cells (*ONG* and *MGP*) (Tanigawa, *et al.*, 2022) and nephrogenic
379 mesenchyme (*COL2A1*) (Menon, *et al.*, 2018; Zhu, *et al.*, 1999)(Figure 5Ai). When compared
380 to standard organoid datasets derived from a range of relevant published protocols, D13+14
381 PT-enhanced organoids possessed a similar cortical stroma gene signature to several datasets,
382 but notably higher expression of the WNT antagonist, *SFRP2*, and pre-cartilage markers,
383 within cortical stroma and unassigned populations (Figure 5Aii).

384 D13 monolayers were similarly re-analysed to determine at which stage of the differentiation
385 protocol (monolayer or 3D culture) stroma and pre-cartilage subtypes appear. Previously
386 shown to contain just 0.9% stromal cells (Supplementary Figure 3A), analysis of the D13
387 sample following *DevKidCC* classification confirmed a lack of stromal progenitor (SP) and
388 medullary stroma (MS) zone markers, while expression of cortical stroma (CS) and pre-
389 cartilage markers were limited (Figure 5Ai). This suggested that these definitive CS and pre-
390 cartilage populations arise during the organoid culture period, but possibly from precursor

391 NPC-like and/or unclassified cell populations in the D13 monolayer owing to their dominance
392 in the differentiations (83%) (Supplementary Figure 3A). Indeed, the NPC-like population in
393 D13 monolayers showed a high similarity to the NPC population without key NPC markers
394 (e.g. *PAX8* and *SIX2*), while Azimuth label transfer method using a human developmental
395 reference dataset (Cao, *et al.*, 2020) still classified the majority (~75%) of D13 monolayer cells
396 as ‘metanephric’ despite 52.3% being unclassified by *DevKidCC* (Supplementary Figure 3A,
397 Figure 5Aiii).

398 The cortical stromal gene expression, notably including the WNT antagonist *SFRP2*, suggested
399 that the central core region of PT-enhanced organoids may control WNT pathway-mediated
400 nephron patterning, in turn driving the observed radial alignment. To functionally test this
401 hypothesis, a WNT signalling gradient was recreated using agarose beads soaked in the
402 tankyrase inhibitor, IWR-1 (10 μ M), which antagonises canonical WNT/ β -catenin pathway
403 activity (Gunaydin, *et al.*, 2012)(Figure 5B). Following the 7 day (standard) differentiation
404 protocol, iPSC-derived kidney progenitors were bioprinted and cultured to create rectangular
405 patch organoids (Lawlor, *et al.*, 2021). At 5 days of organoid culture (D7+5), by which time
406 renal vesicle formation had occurred, IWR-1-soaked or control (PBS-soaked) beads were
407 added to the centre of the organoids where they made contact with the early epithelial structures
408 (Supplementary Figure 4A). After 9 days of organoid culture, organoids with IWR-1-soaked
409 beads exhibited visible differences in the morphology of structures surrounding the beads
410 compared to controls with PBS-soaked beads (Supplementary Figure 4B). This became more
411 apparent when these organoids were stained via immunofluorescence (Figure 5B). In control
412 organoids with PBS-soaked beads, beads were in contact with a mixture of proximal and distal
413 EPCAM-positive nephron epithelium, as well as NPHS1-positive podocytes of glomeruli
414 (Figure 5Bi). In contrast, IWR-1-soaked beads were predominantly surrounded by glomeruli,
415 with few distal structures (LTL-negative/EPCAM-positive) visible overall (Figure 5Bii). These
416 observations were confirmed by image quantification, showing that the percentage of NPHS1+
417 podocytes (glomeruli) was significantly higher in the region adjacent to IWR-1-soaked beads
418 compared to PBS-soaked control beads (Figure 5Ci-ii and Supplementary Table 3).

419 Taken together, these analyses supported establishment of a gradient arising from centralised
420 WNT antagonism as responsible for the nephron directionality and alignment in PT-enhanced
421 organoids.

422 **Mature transporter expression within PT-enhanced organoids enables nephron
423 functionality and drug screening**

424 The strong expression and apical cellular localisation of transporters in PT-enhanced organoids
425 was suggestive of nephron functionality. To test this, we firstly performed multiple substrate
426 uptake assays specific to PTs in both standard and PT-enhanced kidney organoids (Figure 6A).
427 While standard organoids showed evidence of uptake of fluorescently labelled albumin
428 (TRITC-albumin) into MEG-positive PTs (indicative of MEG-CUBN transport function), this
429 uptake was visibly higher in PT-enhanced organoids, with large portions of elongated PTs
430 displaying high-intensity TRITC-albumin fluorescence (Figure 6Ai). In addition, PTs of
431 enhanced organoids demonstrated robust uptake of 4',6-diamidino-2-phenylindole (DAPI),
432 which is an effective probe for evaluation of the PT-specific SLC47 family of organic cation/H⁺
433 antiporters, MATE-1 (Multidrug and Toxin Extrusion Protein 1) and MATE2-K (Multidrug
434 and Toxin Extrusion Protein 2K) (Yasujima, *et al.*, 2010) (Figure 6Aii). The uptake of DAPI
435 by PT cells was successfully inhibited via pre-treatment of organoids with the cation transporter
436 inhibitor Cimetidine, supporting the specificity of transport activity, while the absence of
437 DRAQ7 staining excluded the possibility of DAPI uptake in PTs due to cell death (Figure
438 6Aii). In contrast, standard organoids showed no uptake of DAPI, suggesting functional
439 immaturity of these same drug transporters (Figure 6Aii).

440 Having established albumin and organic cation transport capacity in PT-enhanced organoids,
441 we next assessed their response to nephrotoxic insult (Figure 6BCD). Several recent studies
442 have explored the suitability of kidney organoids as a human-relevant model of cisplatin-
443 induced nephrotoxicity (Freedman, *et al.*, 2015; Morizane, *et al.*, 2015; Takasato, *et al.*, 2015),
444 a common complication that limits usage of this chemotherapeutic agent (Ozkok and Edelstein,
445 2014; Yao, *et al.*, 2007). The biomarker KIM-1 is sensitive for early detection of PT injury in
446 humans and animals (Abdelsalam, *et al.*, 2018; Chiusolo, *et al.*, 2010; Sasaki, *et al.*, 2011;
447 Shinke, *et al.*, 2015; Vaidya, *et al.*, 2010) and has been shown to increase in response to
448 cisplatin in kidney organoids, despite conflicting reports regarding its PT-specificity
449 (Morizane, *et al.*, 2015; Takasato, *et al.*, 2016; Digby, *et al.*, 2020). This discrepancy may arise
450 from immature expression of the predominant cisplatin transporters, particularly
451 SLC22A2/OCT2 (Digby, *et al.*, 2020), combined with heterogeneity in cisplatin uptake
452 mechanisms. Re-analysis of our PT-enhanced and existing standard organoid scRNAseq
453 datasets (Howden, *et al.*, 2019) revealed higher expression of the majority of cisplatin influx

454 and efflux transporters in enhanced compared to standard organoid PT cells (Supplementary
455 Figure 4C), suggestive of cisplatin transport capacity. This included *SLC22A2/OCT2*,
456 previously reported to show low expression in kidney organoids (Digby, *et al.*, 2020). To
457 confirm the functionality of these transporters and appropriate injury response by PTs, iPSC
458 line-matched D7+14 (standard) and D13+14 (enhanced) organoids were derived from
459 monolayer differentiations across 3 independent experiments. Organoids were exposed to 20
460 μM cisplatin for 24 hours prior to assessment for expression of KIM1 protein its corresponding
461 gene, *HAVCR1*. Immunofluorescence revealed an upregulation of KIM-1 protein expression
462 within LTL-positive PTs of both standard and enhanced organoids compared to PBS-treated
463 controls (Figure 6Bi-ii). This was supported by a significant increase in KIM-1 gene (*HAVCR1*)
464 expression in PT-enhanced organoids compared to standard organoids (Figure 6C). Also
465 noteworthy was the similar *HAVCR1* expression levels in standard and PT-enhanced organoids
466 when gene level was expressed relative to the absolute amount of PT in each organoid (marked
467 by *HNF4A*). This suggested that the levels of *HAVCR1* upregulation may be dictated by
468 proximal tubule proportion (Figure 6D). However, in both standard and PT-enhanced
469 organoids, *HAVCR1* expression was significantly increased compared to control organoids
470 (Supplementary Figure 4D).

471 **PT-enhanced organoids represent an improved model for SARS-CoV-2 pathogenesis
472 research**

473 Kidney organoids have previously proven useful to model inherited, early-onset kidney disease
474 (Freedman, *et al.*, 2015; Taguchi and Nishinakamura, 2017; Czerniecki, *et al.*, 2018; Cruz, *et*
475 *al.*, 2017; Forbes, *et al.*, 2018; Hale, *et al.*, 2018; Hollywood, *et al.*, 2020; Mae, *et al.*, 2013;
476 Przepiorski, *et al.*, 2018; Tanigawa, *et al.*, 2018). More recently, organoids have been
477 successfully applied to understanding the pathogenesis of the infectious respiratory disease
478 COVID-19, with SARS-CoV-2 viral infection and replication being achieved in a range of
479 stem cell-derived tissues (Han, *et al.*, 2020; Marchiano, *et al.*, 2021; Mills, *et al.*, 2021; Sharma,
480 *et al.*, 2020; Tiwari, *et al.*, 2021). Driven by the occurrence of AKI in COVID-19 patients
481 (Huang, *et al.*, 2020; Kunutsor and Laukkanen, 2020; Yang, *et al.*, 2020; Zhou, *et al.*, 2020), a
482 handful of studies have explored kidney organoids as a potential model of COVID-19 (Monteil,
483 *et al.*, 2020; Wysocki, *et al.*, 2021). While it is still debated whether kidney damage results
484 from direct viral infection or a combination of inflammatory responses and drug nephrotoxicity
485 (reviewed in (Motavalli, *et al.*, 2021), human PTs show high expression of the key SARS-CoV-

486 2 receptor ACE2 (Kowalcuk, *et al.*, 2008; Hoffmann, *et al.*, 2020) and evidence of viral
487 infection (Braun, *et al.*, 2020; Farkash, *et al.*, 2020; Kissling, *et al.*, 2020; Puelles, *et al.*, 2020;
488 Su, *et al.*, 2020; Werion, *et al.*, 2020; Hanley, *et al.*, 2020).

489 Given the high proportion of PT in enhanced organoids, we investigated their suitability as a
490 model of SARS-CoV-2 infection and pathogenesis. Comprehensive analysis of scRNASeq data
491 from >15,800 D13+14 organoid cells revealed expression levels and cellular localisation of a
492 range of entry factors (receptors, proteases and binding proteins) previously implicated in
493 SARS-CoV-2 infection (Amraei, *et al.*, 2021; Singh, *et al.*, 2020) (Supplementary Figure 5A).
494 When comparing age- and line-matched organoids, all SARS-CoV-2 entry factors of the
495 proximal and distal tubular segments showed increased expression levels and abundance in PT-
496 enhanced organoids compared to our existing standard organoid dataset (Figure 7A). The two
497 most frequently reported viral entry factors in literature, ACE2/ACE2 and
498 TMPRSS2/TMPRSS2 (Hoffmann, *et al.*, 2020), were confirmed to be expressed at both a gene-
499 and protein-level in proximal and distal nephron compartments, respectively (Figure 7AB),
500 supporting previous reports *in vivo* and in kidney organoids (Kowalcuk, *et al.*, 2008; Camargo,
501 *et al.*, 2009; Han, *et al.*, 2020; Monteil, *et al.*, 2020; Wysocki, *et al.*, 2021).

502 Apical ACE2 expression was also identified in epithelial cells lining the initial portion of
503 Bowman's capsule transitioning from the S1 segment of the PT (Supplementary Figure 5C).
504 Previous studies in mice have identified these transitionary cells as cuboidal and intermediate
505 parietal epithelial cells (cuPECs and iPECs), making up the most proximal part of the PT prior
506 to transitioning to flat PECs that line Bowmans's capsule (Kuppe, *et al.*, 2019; Wang, 2019).
507 Accordingly, high ACE2 gene expression correlated with a subset of cells co-expressing
508 general PEC markers with a cuPEC/iPEC-specific profile (*PAX8*+, *AKAP12*+, *PROM1*-)
509 (Supplementary Figure 5D). This region also partly coincided with the
510 *SLC34A1*^{Hi}/*HNF4A*⁺/*SLC36A2*⁺ population marking early (S1) PT cells (Lee, *et al.*, 2015;
511 Broer, *et al.*, 2008) (Supplementary Figure 5E), which, along with LTL-positivity of the early
512 Bowmans capsule epithelium (Supplementary Figure 5C), agreed with the known S1-PEC
513 transitionary phenotype reported for cPECs and iPECs (Kuppe, *et al.*, 2019). However, ACE2
514 was absent from podocytes (cluster 12; Supplementary Figure 5ACD). These expression
515 patterns were further supported by analyses of human fetal kidney, with expression of SARS-
516 CoV-2 entry factors exhibiting a highly similar expression pattern to our extended kidney

517 organoids, including low levels of ACE2 in human fetal kidney PECs (Supplementary Figure
518 6AB).

519 Having confirmed the expression of viral entry factors, PT-enhanced and standard organoids
520 were assessed for infectivity following incubation with SARS-CoV-2. Viral infection of kidney
521 organoids was confirmed by visualisation of GFP-expressing SARS-CoV-2 reporter virus
522 (marking replicating virus) (Hou, *et al.*, 2020) in combination with immunofluorescence
523 staining for the spike protein (S; the transmembrane protein responsible for host cell binding
524 and viral entry) (Supplementary Figure 5D). To confirm the presence of viral genome, culture
525 media from standard and PT-enhanced organoids were harvested every second day post-
526 infection for qRT-PCR of SARS-CoV-2 viral envelope gene expression (*E*; genome copies per
527 mL) (Figure 7Ci) and virus titration in Vero cells to calculate median Tissue Culture Infectious
528 Dose (TCID₅₀) (Figure 7Cii). Infectious virus was detected earlier in PT-enhanced compared
529 to standard organoids (at 2 days post-infection) across independent experiments replicated
530 using the same iPSC line and organoid conditions. In both instances, infectious virus levels
531 reached significance at 4 days post-infection ($P = 0.0297$ and $P = 0.0457$, respectively) (Figure
532 7Ci-ii).

533 To determine the kidney cell types targeted by SARS-CoV-2 in PT-enhanced organoids,
534 infected organoids were analysed via immunofluorescence for double stranded RNA (dsRNA)
535 and nephron-specific markers 6 days post-infection (Figure 7D). In agreement with scRNAseq
536 analyses of ACE2 receptor expression (Supplementary Figures 5ABC and 6B), infected
537 organoids showed dsRNA predominantly in LTL-positive PTs, as well as Bowman's capsule
538 surrounding NPHS1-positive podocytes (undetectable in podocytes themselves) and some
539 detection in SLC12A1-positive Loops of Henle (Figure 7Di-iii). The specificity of this staining
540 was confirmed by immunofluorescence of uninfected control organoids, which showed no
541 staining for dsRNA (Supplementary Figure 6D). Despite their infection, tubular epithelium in
542 organoids exposed to SARS-CoV-2 retained key characteristics such as apically-restricted LTL
543 and SLC12A1, as well as membrane-bound EPCAM staining (Figure 7Di and iii,
544 Supplementary Figure 6Ei). However, upregulation of KIM-1 was observed in infected
545 organoids and found to be significantly higher than mock (uninfected) control organoids at a
546 gene level, complementing results of previous publications (Supplementary Figure 6Ei-ii)
547 (Chen, *et al.*, 2021; Jansen, *et al.*, 2022).

548 **Discussion**

549 The utility of human PSC-derived kidney organoids as accurate models for disease research
550 applications will rely upon their nephron maturation and functionality. To date, proximal
551 tubules characterised within kidney organoids have lacked significant evidence of functional
552 solute transport. In this study, we have shown that prolonged maintenance and delayed
553 epithelialisation of the nephron progenitor population improved PT maturation and
554 functionality compared to standard organoid protocols. Critically, this approach promoted
555 development of distinct S1, S2, and S3 cell populations within the PT, a feature not previously
556 identified in a kidney organoid. The application of *DevKidCC* in the current study enabled an
557 unbiased and quantitative transcriptional comparison to previous published kidney organoid
558 and human fetal kidney datasets, providing a reliable readout of cell identity and maturation
559 and minimising the caveats associated with comparing restricted marker panels (Wilson, *et al.*,
560 2021).

561 Treatment strategies for coronavirus infections, including SARS-CoV and MERS-CoV, are
562 still in their infancy with progress reliant upon an improved understanding of virus biology and
563 interaction with host factors (V'Kovski, *et al.*, 2021). Despite the rapid accumulation of
564 information on SARS-CoV-2, findings have often been conflicting or challenging to interpret,
565 including reported heterogeneity in the expression of viral entry factors and the correlation
566 between expression levels and disease outcome (Zlacka, *et al.*, 2021; Jackson, *et al.*, 2022;
567 Muus, *et al.*, 2021). PT-enhanced organoids exhibited a robust response to the nephrotoxic
568 chemotherapeutic cisplatin and superior infectivity with SARS-CoV-2 compared to standard
569 organoids. This enhanced patterning and functionality underscores the advantage of PT-
570 enriched organoids for drug screening and disease modelling applications, including as a model
571 of infectious disease in the kidney.

572 PT-enhanced organoids exhibited improved expression of a range of previously identified viral
573 entry factors compared to standard organoids, including the key SARS-CoV-2 receptor (ACE2)
574 on the apical membrane of PT cells. This translated to higher virus replication levels in PT-
575 enhanced organoids, determined by both dsRNA quantification and infectious viral genome
576 copies across multiple timepoints, replicates, and independent experiments. Previous kidney
577 organoid studies have reported podocyte SARS-CoV-2 infection using stem cell-derived
578 kidney models (Jansen, *et al.*, 2022; Kalejaiye, *et al.*, 2022). In contrast, we saw limited viral

579 entry factor expression and no evidence of *ACE2*/*ACE2* within podocytes of PT-enhanced
580 organoids and human fetal kidney. It is possible that reports of podocyte infection reflected
581 viral entry in more immature podocytes or parietal cells, given the reported variation in genuine
582 podocyte gene expression arising from the use of different cellular models/formats (Hale, *et*
583 *al.*, 2018; Kalejaiye, *et al.*, 2022). In addition, while previous transcriptional profiling of
584 infected organoids claimed the presence of virus within most cell populations (Jansen, *et al.*,
585 2022), no viral entry factor expression was observed in any cell cluster within that study. Here
586 again we conclude that PT-enhanced organoids represent a more accurate model of the mature
587 nephron.

588 It remains to be seen whether the enhanced PT development in these organoids results from
589 improved nephron progenitor expansion or sufficient time to form a more metanephric nephron
590 progenitor population. Transcriptional profiling of day 13 monolayers exposed to CDLY2
591 showed a high proportion of nephron progenitors with a significant increase in nephron
592 progenitor gene expression (*SIX1*, *LYPDI*) and metanephric HOX ortholog expression
593 (*HOX11A/C/D*) in comparison to other relevant published scRNAseq datasets. One unique
594 feature critical to the overall outcome of this modified protocol included the addition of
595 nephron progenitor maintenance media that prolongs low-level canonical WNT signalling
596 (CHIR), suppresses NOTCH signalling (DAPT), and increases BMP7 activity (BMP7)
597 (Tanigawa, *et al.*, 2016). Inclusion of these factors agreed with mouse studies which have
598 shown a requirement for Notch to initiate nephron progenitor commitment and nephron
599 formation, as well as demonstration that Notch2 supports proximal nephron patterning (Chung,
600 *et al.*, 2017; Surendran, *et al.*, 2010). In addition, low levels of canonical Wnt activity and
601 Bmp/BMP signalling via MAPK and PI3K pathways have been proposed to support nephron
602 progenitor survival (Brown, *et al.*, 2015; Karner, *et al.*, 2011; Park, *et al.*, 2007; Blank, *et al.*,
603 2009; Lindstrom, *et al.*, 2015; Muthukrishnan, *et al.*, 2015). Despite containing both low CHIR
604 and BMP7, the alternate nephron progenitor maintenance media NPSR was unable to support
605 subsequent nephron formation in the resulting organoids, possibly due to the inclusion of BMP
606 and TGF β receptor inhibitors (dual inhibition of SMAD1/5/8 and SMAD2/3) (Li, *et al.*, 2016),
607 which may maintain a less competent nephron progenitor population (Tanigawa, *et al.*, 2019).

608 The influence of timing on protocol outcome also cannot be discounted. Recent studies of the
609 relative timing of PSC differentiation suggest that development and maturation *in vitro* is
610 influenced by a predetermined species-specific biological clock. This has been elegantly

611 demonstrated by Matsuda *et al* (2020), showing that the markedly different paces of
612 differentiation exhibited by mouse and human PSCs can be attributed to biochemical rate
613 variations that influence the segmentation clock (Matsuda, *et al.*, 2020). Indeed, brain
614 organoids require months in culture to develop specific neural subtypes, akin to human
615 gestation (Lancaster, *et al.*, 2013; Velasco, *et al.*, 2019). While our PT-enhanced kidney
616 organoid protocol already shows considerable improvements in maturation after only 3 – 4
617 weeks, there is likely room for additional improvements including the timing of growth factor
618 exposure and optimisation of metabolic conditions beyond the monolayer differentiation phase.

619 Despite enhancing PT development, this protocol faces some limitations with respect to
620 nephron patterning and off-target populations. While providing a powerful model of PT
621 function, reduced patterning to distal tubular segments highlights the challenge of
622 simultaneously generating all kidney cell types in a single protocol, as previously described in
623 mouse ((Freedman, *et al.*, 2015; Morizane, *et al.*, 2015; Toyohara, *et al.*, 2015; Taguchi, *et al.*,
624 2014). In addition, the formation of pre-cartilage cells is problematic for any potential clinical
625 application, albeit not unique to this approach. Cartilage development has been observed in
626 organoids from several protocols following transplantation (Bantounas, *et al.*, 2020; Nam, *et*
627 *al.*, 2019; van den Berg, *et al.*, 2018). In PT-enhanced organoids, this may represent a side-
628 effect of prolonged BMP signalling that could potentially be suppressed through timed
629 SMAD1/5/8 inhibition. The presence of central pre-cartilage within the cortical stroma
630 population of the organoid core resulted in strong central WNT antagonism (*SFRP2*) that
631 contributed to the striking nephron alignment observed. The establishment of a sink and source
632 of WNT activity along the length of the tubule, driving nephron directionality, is in agreement
633 with our current understanding of proximodistal patterning during mouse development
634 (Lindstrom, *et al.*, 2015), while the cortical stroma population likely supports and promotes the
635 proximal nephron development (Das, *et al.*, 2013). Interestingly, while standard organoids
636 develop regions of cartilage post transplantation, they do not display this characteristic nephron
637 spatial arrangement either before or after transplant. It is possible that this core is the result of
638 altered biophysical parameters. We have previously shown that higher density standard
639 organoids favour the development of a central unpatterned core, whereas a bioprinted sheet
640 does not (Lawlor, *et al.*, 2021). Such observations indicate that an interplay between cell
641 deposition density and the patterning of the mesodermal population in the enhanced protocol
642 facilitated the strong centralised source of WNT antagonism. Together this suggests an

643 approach to further control the spatial organisation of bioengineered tissue through
644 manipulation of signalling gradients.

645 In conclusion, we describe here a protocol that enabled improved patterning and maturation of
646 proximal tubules within kidney organoids. These show significant advantages for modelling
647 an appropriate damage response following drug-induced injury and SARS-CoV-2 infection,
648 underscoring the utility of this approach as a platform to model a range of proximal tubular
649 disease states.

650

651 **Methods**

652 ***iPSC lines and maintenance***

653 iPSC lines used in this study include CRL1502.C32 (Takasato, *et al.*, 2015; Briggs, *et al.*, 2013)
654 CRL-2429/SIX2^{Cre/Cre}:GAPDH^{dual} (Howden, *et al.*, 2019), PCS-201-010/HNF4A^{YFP}
655 (Vanslambrouck, *et al.*, 2019), and PB010/MCRIi010-A (Vlahos, *et al.*, 2019). All iPSC lines
656 were maintained and expanded at 37°C, 5% CO₂ and 5% O₂ in Essential 8 medium (Thermo
657 Fisher Scientific, Waltham, MA) on Matrigel- (BioStrategy, Victoria, Australia) coated plates
658 with daily media changes and passaged every 2 – 3 days with EDTA in 1X PBS as described
659 previously (Chen, *et al.*, 2011).

660 ***Directed differentiation and kidney organoid generation***

661 For standard organoid production, differentiation of iPSC lines and organoid culture was
662 performed as described previously (Howden, *et al.*, 2019), with minor variations in the
663 concentration of Laminin-521 (BioLamina, Sundbyberg, Sweden) used to coat 12-well plates,
664 initial iPSC seeding density within 12-well plates, and CHIR99021 (R&D Systems)
665 concentration and duration of exposure according to the iPSC line used (CRL1502.C32, CRL-
666 2429/SIX2^{Cre/Cre}:GAPDH^{dual} and PB010/MCRIi010-A were seeded at 25,000 cells/well and
667 exposed to 6μM CHIR for 5 days; PCS-201-010/HNF4A^{YFP} was seeded at 40,000 cells/well
668 and exposed to 6μM CHIR for 4 days; CRL1502.C32, CRL-2429/SIX2^{Cre/Cre}:GAPDH^{dual} were
669 seeded with 20μL/mL Laminin-521; PB010/MCRIi010-A and PCS-201-010/HNF4A^{YFP} were
670 seeded with 40μL/mL Laminin-521). Standard bioprinted patch organoids were generated as
671 described previously (Lawlor, *et al.*, 2021).

672 For PT-enhanced organoids, Matrigel concentrations and iPSC seeding density for
673 differentiation in 12-well plates were as stated for standard organoids above. iPSCs were then
674 subjected to prolonged monolayer differentiation in 6μM CHIR for 5 days, followed by
675 200ng/mL FGF9 (R&D Systems) and 1μg/mL heparin (Sigma Aldrich) until day 8, refreshing
676 the media every second day. At day 8, the monolayer was exposed to 1mL/well nephron
677 progenitor maintenance media, NPSR or CDLY (Li, *et al.*, 2016; Tanigawa, *et al.*, 2016),
678 refreshing these media daily. Final PT-enhanced organoid conditions utilised CDLY2,

679 containing 2X concentration of BMP7. Organoids were generated and cultured as described
680 previously (Takasato, *et al.*, 2016).

681 ***Immunofluorescence and confocal microscopy***

682 For immunofluorescence, organoids were fixed and stained as previously described
683 (Vanslambrouck, *et al.*, 2019) using the antibodies detailed in Table 1, diluted in 0.1% TX-
684 100/PBS. Imaging was performed on the ZEISS LSM 780 confocal microscope (Carl Zeiss,
685 Oberkochen, Germany) with acquisition and processing performed using ZEISS ZEN Black
686 software (Zeiss Microscopy, Thornwood, NY) and Fiji ImageJ (Schindelin, *et al.*, 2012).

687 ***Flow cytometry***

688 Flow cytometry of reporter line-derived organoids using endogenous fluorescence was
689 performed and analysed as described previously (Vanslambrouck, *et al.*, 2019). To determine
690 the contribution of SIX2-mCherry + cells to EPCAM+ populations in organoids derived from
691 the SIX2^{Cre} lineage tracing iPSC line, dissociated and strained cells were stained using directly
692 conjugated anti-EPCAM Alexa Fluor-647 antibody (see Table 1) diluted 1:100 in 100 µL of
693 FACS wash (1% fetal calf serum [FCS] in PBS) for every 5 x10⁵ cells. Following 30 minutes
694 incubation on ice, cells were washed 3 times in 2mL FACS wash via centrifugation prior to
695 flow cytometry.

696 ***Histology***

697 For Alcian Blue detection of cartilage, organoids were fixed in 4% PFA as described above
698 and processed for routine paraffin embedding using the Excelsior AS Tissue Processor (rapid
699 biopsy setting; Thermo Fisher Scientific). Samples were embedded in wax and 5µm sections
700 cut using a Waterfall HM325 microtome (Thermo Fisher Scientific). Sections were dewaxed,
701 hydrated through graded alcohols to running water, then covered with Alcian Blue Solution
702 (1% Alcian blue in 3% acetic acid, pH 2.5). After 10 minutes, sections were washed in tap
703 water for 2 minutes and counterstained for 7 minutes in Nuclear Fast Red stain (0.1% Nuclear
704 Fast Red [Sigma Aldrich, St Louise, MO] and 5% ammonium potassium sulfate in water).
705 Following staining, sections were dehydrated in graded alcohols, cleared in Safsolvent (Bacto

706 Laboratories, NSW, Australia), and coverslipped. Images were acquired on a Zeiss Axio
707 Imager A2 with Zeiss Zen software (Zeiss Microscopy, Thornwood, NY).

708 ***Real-time quantitative reverse transcription PCR (qRT-PCR)***

709 RNA extraction, cDNA synthesis and quantitative RT-PCR (qRT-PCR) were performed using
710 the Bioline Isolate II Mini/Micro RNA Extraction Kit, SensiFAST cDNA Synthesis Kit and
711 the SensiFAST SYBR Lo-ROX Kit (Bioline, NSW, Australia), respectively, as per
712 manufacturer's instructions. Each qRT-PCR reaction was performed in triplicate using the
713 primer pairs detailed in Table 2. Data were graphed and analysed in Prism 8 (GraphPad).

714 ***Single cell RNA sequencing (scRNAseq) and dataset generation***

715 The D13+12 dataset was generated using the CRL-2429/SIX2^{Cre/Cre}:GAPDH^{dual} iPSC line. The
716 D13 and D13+14 organoids were generated using the CRL1502.C32 with four replicates per
717 time point, where each replicate was derived from an independent well. Cells were dissociated
718 following previously published methods (Lawlor, *et al.*, 2021). For the D13 and D13+14
719 samples, replicates were multiplexed following the method of Soeckius *et al.* (Stoeckius, *et al.*,
720 2018). Cells were stained for 20 minutes on ice with 1µg of BioLegend TotalSeq-A anti-human
721 hashtag oligo antibody (BioLegend TotalSeq-A0251 to A0258). Cells were washed 3 times
722 then pooled at equal ratios for sequencing. A single library was generated for each
723 suspension/condition, composed of equally sized pools of each replicate (Set 1 – 4). Libraries
724 were generated following the standard 10x Chromium Next GEM Single Cell 3' Reagent Kits
725 v3.1 protocol except that 'superloading' of the 10x device was performed with ~30k cells. Hash
726 tag oligo (HTO) libraries were generated following the BioLegend manufacturer protocol.
727 Sequencing was performed using an Illumina Novoseq.

728 10x mRNA libraries were demultiplexed using CellRanger (3.1.0) to generate matrices of UMI
729 counts per cell. HTO libraries were demultiplexed using Cite-seq-count (1.4.3) to generate
730 matrices of HTO counts per cell barcode. All data were loaded into Seurat (3.1.4) and HTO
731 libraries were matched to mRNA libraries. Seurat was used to normalise HTO counts and
732 determine cut-offs to assign HTO identity per cell using the *HTODemux* function with the
733 positive.quantile parameter set at 0.99. HTO doublet and unassigned cells were removed, as
734 were cells with mitochondrial content greater than 35% accounting for the increased metabolic

735 activity of renal epithelium (Ransick, *et al.*, 2019), number of genes per cell greater than 500
736 and the number of UMIs less than 100000, to obtain filtered datasets (D13 replicates: 3694
737 cells [A0251], 3545 cells [A0252], 3785 cells [A0253], 3641 cells [A0254]; D13+14 replicates:
738 3415 cells [A0255], 2350 cells [A0256], 2904 cells [A0257], 2578 cells [A0258]). The
739 combined datasets contained a median of 3915 genes expressed per cell, with a median of
740 16352 UMI counts per cell.

741 ***Analysis of scRNAseq datasets***

742 Data was normalised using the SCTransform method (Hafemeister and Satija, 2019) including
743 the regression of cell cycle scores. A 30 component Principal Component Analysis (PCA) was
744 performed, followed by Uniform Manifold Approximation and Projection (UMAP) using these
745 PCA components. Seurat's graph-based clustering approach was used to identify, with
746 resolutions of 0.7 (D13) and 0.5 (D13+14) chosen for downstream analysis. Marker analysis
747 was performed using the Seurat *FindMarkers* function, using student's t-test, limited to positive
748 markers (i.e. increased expression within a cluster) above 0.25 log fold-change expressed in at
749 least 10% of cells within a cluster. Marker lists were exported and cluster identities were
750 determined by comparison with published human single cell data (Howden, *et al.*, 2019) or
751 Gene ontology analysis using ToppFun (<https://toppgene.cchmc.org/enrichment.jsp>). The PT
752 cluster was isolated and reanalysed as above to further investigate any subpopulations.

753 The D13+12 dataset was integrated with an age- and line-matched published dataset (Howden,
754 *et al.*, 2019) using the anchor-based method within Seurat (Butler, *et al.*, 2018; Stuart, *et al.*,
755 2019). This integrated dataset was analysed as above, isolating the PT cluster and comparing
756 gene expression of cells from both samples within this population.

757 For DevKidCC analyses, The D13 and D13p14 samples were analysed using DevKidCC
758 (v0.0.3); a hierarchical set of machine-learning binary classifiers trained on a human fetal
759 kidney reference dataset. The classified dataset was then compared to relevant existing single
760 cell organoid datasets using the *DotPlotCompare* function.

761 For Azimuth analyses, cells were uploaded to the online Azimuth portal at
762 <https://app.azimuth.hubmapconsortium.org/app/human-fetus> and instructions were followed
763 as per the website for the analysis.

764 ***Agarose bead-mediated morphogen signalling assay***

765 Bioprinted patch organoids were generated and cultured as described previously prior to the
766 addition of morphogen-soaked beads at D7+5 (Lawlor, *et al.*, 2021). The day before bead
767 addition, 100 μ L of Affi-Gel Blue Gel 100 – 200 mesh crosslinked agarose beads (Bio-Rad
768 Laboratories, Hercules, CA), were washed 3 times in PBS via centrifugation. Washed beads
769 were resuspended in 100 μ L of PBS (control) or 10 μ M IWR-1 (stock reconstituted according
770 to manufacturer's instructions; Sigma Aldrich) and incubated for 1 hour at room temperature
771 prior to overnight storage at 4°C. On day 7+5, suspensions were agitated to resuspend beads
772 and 0.3 μ L was added to the centre of each patch organoid with the aid of a P2 pipette and
773 dissecting microscope (Leica Microsystems, Wetzlar, Germany). Organoid media (TeSR-E6
774 [STEMCELL Technologies, Vancouver Canada]) was refreshed every second day prior to
775 harvest at D7+9 for immunofluorescence.

776 ***Quantification of tissue patterning changes in response to IWR soaked beads***

777 Tissue patterning within the radius of beads was quantified using custom Python (3.10.2)
778 scripts, with method as follows. Images ($n = 3$ per condition, IWR soaked and control) were
779 loaded as Numpy (1.22.1) (Harris, *et al.*, 2020) arrays using the Czifile library (2019.7.2) and
780 masks of bead location were generated by manually segmenting each bead using the Napari
781 (0.4.13) labels layer feature. Nephron segments were segmented by applying a gaussian filter
782 to each channel (sigma of 5 pixels) followed by Otsu thresholding (for NPHS1 staining) or
783 multi-otsu thresholding (for LTL, EPCAM) using the second threshold value. All processing
784 was implemented using functions in scikit-image (0.19.2) (van der Walt, *et al.*, 2014). The
785 distance of each pixel in the image from the bead edge was calculated using the Euclidian
786 distance transform in Scipy (1.7.3) (Virtanen, *et al.*, 2020). These values were used to define
787 the total region within 200 pixels of the bead surface, including the beads themselves. The
788 percentage of pixels assigned to each nephron marker as a proportion of total nephron tissue
789 (defined by the total pixels that were segmented as NPHS1 or EPCAM positive), within the
790 200 pixel region of each image was then calculated. Scipy was used to conduct t-tests,
791 Matplotlib (3.5.1) was used to generate plots and Napari was used to generate composite
792 images.

793 ***Cisplatin toxicity assay***

794 D13+14 PT-enhanced organoids were exposed through the basolateral compartment of the
795 Transwell tissue culture plate (Corning Incorporated, Corning, NY) to 1mL per well of 20 µM
796 Cisplatin (Accord Healthcare, Durham, NC), or an equivalent volume of PBS, in TeSR-E6 for
797 24 hours (37°C, 5% CO₂ and 5% O₂). Following incubation, organoids within Transwells were
798 washed with PBS and harvested for flow cytometry as described above.

799 ***Fluorescent substrate uptake assays***

800 For albumin uptake assays, D13+14 PT-enhanced organoids (triplicate wells per condition)
801 were incubated in TRITC albumin (1:1000, Sigma Aldrich) and anti-MEGALIN/LRP2 (1:500,
802 pre-incubated with an alpaca Nano-secondary Alexa Fluor 647 secondary antibody diluted in
803 TeSR-E6 culture media via the basolateral compartment of Transwell tissue culture plates and
804 incubated overnight (37°C, 5% CO₂ and 5% O₂). Control organoids were incubated in
805 secondary antibody alone. After incubation, plates containing organoids were washed in at least
806 3 changes of Hanks' Balanced Salt Solution (HBSS; Thermo Fisher Scientific) for 30 minutes
807 and live-imaged immediately using a ZEISS LSM 780 confocal microscope. For organic
808 cation transport assays, D13+14 PT-enhanced organoids (triplicate wells per condition) were
809 incubated in 4',6-diamindino-2-phenylindole substrate (DAPI; 1:1000 [Thermo Fisher
810 Scientific]) with 1:500 DRAQ7 dead cell label (Thermo Fisher Scientific) diluted in TeSR-E6
811 for 1 hour (37°C, 5% CO₂ and 5% O₂). Control organoids were pre-incubated for 15 minutes
812 in 100 µM Cimetidine inhibitor (Sigma Aldrich) prior to incubation for 1 hour in TeSR-E6
813 containing both inhibitor, substrate, and dead cell label (1:1000 DAPI, 1:500 DRAQ7, 100 µM
814 Cimetidine). Following incubation, substrate and substrate + inhibitor solutions were replaced
815 with HBSS and live-imaged immediately using a ZEISS LSM 780 confocal microscope.

816 ***Viral infection assays***

817 Standard and PT-enhanced organoids grown on Transwells were infected with 10⁴ tissue-
818 culture infectious dose 50 (TCID₅₀) of SARS-CoV-2 (Australia/VIC01/2020) in TeSR-E6
819 media added above the Transwell for 3 hours (virus titration experiments) or below the
820 Transwell with a drop ontop of the organoid for 1 hour (virus localisation experiments).
821 Following incubation (37°C and 5% CO₂), the viral inoculum was removed and replaced with
822 1mL of plain TeSR-E6 medium beneath the Transwell as for typical organoid culture
823 (Takasato, *et al.*, 2016). Culture medium was collected on days 0, 2, 4, and 6 post-infection for

824 viral titer quantification and replaced with fresh medium. Median TCID₅₀ in supernatants were
825 determined, as detailed below, by 10- fold serial dilution in Vero cells and calculated using the
826 Reed and Muench method. Organoids were harvested at 6 days post-infection and fixed with
827 4% PFA fixation for immunofluorescence.

828 ***Infectious virus titration (Median Tissue Culture Infectious Dose assay; TCID₅₀)***

829 Viral titrations were performed on confluent monolayers of Vero cells in 96-well plates. Wells
830 were washed with plain minimum essential media (MEM) and replaced with 180µl of infection
831 media (MEM, 50U/ml Penicillin, 50µg/ml Streptomycin, 2mM GlutaMax, 15mM HEPES and
832 1µg/ml TPCK-treated Trypsin). 20µl of the samples to be titred were added to four wells and
833 10-fold serial dilutions were made. Plates were incubated at 37°C and 5% CO₂. Four days post-
834 infection, SARS-CoV-2-induced cytopathic effect was assessed by microscopy.

835 ***RT-qPCR for SARS-CoV-2 genome***

836 RNA was extracted from supernatant culture media using the QIAamp 96 Virus QIAcube HT
837 Kit (Qiagen). E-gene expression was determined using the SensiFAST Probe No-Rox One Step
838 Kit (Bioline) and the following primers/probes: Fwd: 5'-
839 ACAGGTACGTTAATAGTTAATAGCGT'-3, Rev: ATATTGCAGCAGTACGCACACA
840 and Probe: FAM-ACACTAGCCATCCTACTGCGCTTCG-BBQ. Viral genome copies were
841 interpolated using a standard curve generated by using a plasmid vector containing the *E*-gene.

842

843

844

845

846 **Tables**

847 **Table 1.** Antibodies used in immunofluorescence studies.

Specificity	Host species	Dilution range	Manufacturer and identifier
ACE2	Rabbit	1:300	Abcam (ab15348)
CUBILIN	Goat	1:300	Santa Cruz Biotechnology (sc-20607)
dsRNA	Mouse	1:300	Absolute Antibody (Ab01299-2.0)
ECADHERIN	Mouse	1:300	BD Biosciences (610181)
EpCAM (Alexa488 or Alexa647 conjugate)	Mouse	1:300	BioLegend (324210 and 324212)
GATA3	Goat or rabbit	1:300	R&D Systems (AF2605) and Cell Signalling Technology (95852S)
GFP	Chicken	1:200 - 1:300	Sapphire Bioscience (ab13970)
HNF4A	Mouse	1:300	Life Technologies (MA1-199)
KIM-1	Goat	1:300	R&D Systems (AF1750)
mCherry (RFP)	Rabbit	1:300 – 1:400	MBL Medical & Biological Laboratories Co. Ltd. (PM005)
MEGALIN	Rabbit	1:300	Sapphire Bioscience (NBP2-39033)
NEPHRIN	Sheep	1:300	R&D Systems (AF4269)
Proximal tubule brush border membrane	<i>Lotus tetragonobulus</i> lectin (LTL)	1:300 – 1:500	Vector Laboratories (B-1325)
TMPRSS2	Mouse	1:300	Merck (MABF2158-25UG)
S2 subunit of SARS-CoV-2 spike protein (stain: Sin2774)	Rabbit	1:300	GeneTex/Sapphire Bioscience (GTX632604)
SLC6A19	Chicken	1:100 – 1:200	Aves Laboratories (custom antibody)
SLC12A1	Rabbit	1:300 – 1:400	Proteintech (18970-1-AP)

848

849

850 **Table 2.** Forward and reverse primers used for qRT-PCR.

Gene	Forward primer (5'-3')	Reverse primer (5'-3')
DAPL1	CTCGGAAAGGGGGACATCCT	AGTTGAGCTTCTCCAGTGCG
GAPDH	CTCTCTGCTCCTCCTGTCGA	TGAGCGATGTGGCTCGGCT
GATA3	GCCCCTCATTAAGCCCAAG	TTGTGGTGGTCTGACAGTCG
HAVCR1	GTTCCTCCAATGCCTTGCC	CGGTGTCATTCCATCTGTTG
HNF4A	ACCCTCGTCGACATGGACA	GCCTTCTGATGGGGACGTG
HOXD11	GCCAGTGTGCTGTCGTTCCC	CTTCCTACAGACCCGCCGT
LHX1	CGTCATTCAAGGTCTGGTTCC	CCCGTAGTACTCGCTCTGGT
PARAXIS	GGGGGTGGCCGTCGT	CAGGCTGAATGGATCCTCAC
SIX1	AAAGGGAAGGAGAACAAAGGATAG	GGAGCCTACATGATTACTGGG
SIX2	TCCTGGTCCCTCCGTATGTA	TAGGGGCAGATAGACCACCA
TMEM-100	CAGGCGTTGCTGTTCTTGT	CAGGGTGAAAGCTGGAGAG
WNT4	AACTGCTCCACACTCGACTC	TGACCACTGGAAGCCCTGT

851

852 **Acknowledgements**

853 This work was supported by the National Health and Medical Research Council
854 (GNT1156440), the National Institutes of Health (UH3DK107344) and the Victorian State
855 Government (DJPR/COVID-19). MHL is an NHMRC Senior Principal Research Fellow
856 (GNT1136085). We acknowledge the Stafford Fox Medical Research Foundation MCRI
857 genome editing facility for the generation of all pluripotent stem cell lines. We thank Maelle
858 Le Moing and the Murdoch Children's Research Institute Translational Genomics Unit for 10x
859 single cell and hash-tag oligo library preparation and sequencing, and bulk-RNAseq
860 sequencing; Matthew Burton and the Murdoch Children's Research Institute Microscopy Core;
861 Professor John Rasko and Dr Charles Bailey for providing the SLC6A19 antibody; Dr Dad

862 Abu-Bonsrah for providing the dsRNA antibody; Professor Ralph Baric for providing the GFP-
863 tagged SARS-CoV-2.

864

865 **Author Contributions**

866 JMV, MHL, and KS contributed to experimental design and planning. JMV, KST, EG, RR,
867 JN, SM, MS, and SEH performed experiments and developed reagents and methods. SBW and
868 JMV performed bioinformatics analyses. KL performed image analyses. JMV, MHL, and
869 SBW contributed to manuscript preparation. JMV and MHL wrote the manuscript.

870 **Data availability**

871 All transcriptional profiling datasets have been submitted to GEO (GSE184928). These include
872 scRNAseq from D13 monolayer differentiation, D13+14 PT-enhanced kidney organoids, and
873 D13+12 PT-enhanced kidney organoid. Code and raw data for scRNAseq and image analyses
874 are available through the Github repository
875 (<https://github.com/KidneyRegeneration/Vanslambrouck2022>).

876 **Competing interests**

877 The authors declare they have no competing interests.

878

879 **References**

- 880 1 Zhuo, J. L. & Li, X. C. Proximal nephron. *Compr Physiol* **3**, 1079-1123,
881 doi:10.1002/cphy.c110061 (2013).
- 882 2 Kirita, Y., Wu, H., Uchimura, K., Wilson, P. C. & Humphreys, B. D. Cell profiling of
883 mouse acute kidney injury reveals conserved cellular responses to injury. *Proc Natl
884 Acad Sci U S A* **117**, 15874-15883, doi:10.1073/pnas.2005477117 (2020).
- 885 3 Freedman, B. S., Brooks, C. R., Lam, A. Q., Fu, H., Morizane, R., Agrawal, V., Saad,
886 A. F., Li, M. K., Hughes, M. R., Werff, R. V., Peters, D. T., Lu, J., Baccei, A., Siedlecki,
887 A. M., Valerius, M. T., Musunuru, K., McNagny, K. M., Steinman, T. I., Zhou, J.,
888 Lerou, P. H. & Bonventre, J. V. Modelling kidney disease with CRISPR-mutant kidney
889 organoids derived from human pluripotent epiblast spheroids. *Nature communications*
890 **6**, 8715, doi:10.1038/ncomms9715 (2015).
- 891 4 Morizane, R., Lam, A. Q., Freedman, B. S., Kishi, S., Valerius, M. T. & Bonventre, J.
892 V. Nephron organoids derived from human pluripotent stem cells model kidney
893 development and injury. *Nature biotechnology* **33**, 1193-1200, doi:10.1038/nbt.3392
894 (2015).
- 895 5 Taguchi, A. & Nishinakamura, R. Higher-Order Kidney Organogenesis from
896 Pluripotent Stem Cells. *Cell Stem Cell* **21**, 730-746 e736,
897 doi:10.1016/j.stem.2017.10.011 (2017).
- 898 6 Takasato, M., Er, P. X., Chiu, H. S., Maier, B., Baillie, G. J., Ferguson, C., Parton, R.
899 G., Wolvetang, E. J., Roost, M. S., Chuva de Sousa Lopes, S. M. & Little, M. H. Kidney
900 organoids from human iPS cells contain multiple lineages and model human
901 nephrogenesis. *Nature* **526**, 564-568, doi:10.1038/nature15695 (2015).
- 902 7 Toyohara, T., Mae, S., Sueta, S., Inoue, T., Yamagishi, Y., Kawamoto, T., Kasahara,
903 T., Hoshina, A., Toyoda, T., Tanaka, H., Araoka, T., Sato-Otsubo, A., Takahashi, K.,
904 Sato, Y., Yamaji, N., Ogawa, S., Yamanaka, S. & Osafune, K. Cell Therapy Using
905 Human Induced Pluripotent Stem Cell-Derived Renal Progenitors Ameliorates Acute
906 Kidney Injury in Mice. *Stem cells translational medicine* **4**, 980-992,
907 doi:10.5966/sctm.2014-0219 (2015).

- 908 8 Combes, A. N., Phipson, B., Lawlor, K. T., Dorison, A., Patrick, R., Zappia, L., Harvey,
909 R. P., Oshlack, A. & Little, M. H. Single cell analysis of the developing mouse kidney
910 provides deeper insight into marker gene expression and ligand-receptor crosstalk.
911 *Development* **146**, doi:10.1242/dev.178673 (2019).
- 912 9 Howden, S. E., Wilson, S. B., Groenewegen, E., Starks, L., Forbes, T. A., Tan, K. S.,
913 Vanslambrouck, J. M., Holloway, E. M., Chen, Y. H., Jain, S., Spence, J. R. & Little,
914 M. H. Plasticity of distal nephron epithelia from human kidney organoids enables the
915 induction of ureteric tip and stalk. *Cell Stem Cell* **28**, 671-684 e676,
916 doi:10.1016/j.stem.2020.12.001 (2021).
- 917 10 Subramanian, A., Sidhom, E. H., Emani, M., Vernon, K., Sahakian, N., Zhou, Y., Kost-
918 Alimova, M., Slyper, M., Waldman, J., Dionne, D., Nguyen, L. T., Weins, A., Marshall,
919 J. L., Rosenblatt-Rosen, O., Regev, A. & Greka, A. Single cell census of human kidney
920 organoids shows reproducibility and diminished off-target cells after transplantation.
921 *Nature communications* **10**, 5462, doi:10.1038/s41467-019-13382-0 (2019).
- 922 11 Wu, H., Uchimura, K., Donnelly, E. L., Kirita, Y., Morris, S. A. & Humphreys, B. D.
923 Comparative Analysis and Refinement of Human PSC-Derived Kidney Organoid
924 Differentiation with Single-Cell Transcriptomics. *Cell Stem Cell* **23**, 869-881 e868,
925 doi:10.1016/j.stem.2018.10.010 (2018).
- 926 12 Marable, S. S., Chung, E. & Park, J. S. Hnf4a Is Required for the Development of Cdh6-
927 Expressing Progenitors into Proximal Tubules in the Mouse Kidney. *J Am Soc Nephrol*
928 **31**, 2543-2558, doi:10.1681/ASN.2020020184 (2020).
- 929 13 Wilson, S. B., Howden, S. E., Vanslambrouck, J. M., Dorison, A., Alquicira-
930 Hernandez, J., Powell, J. E. & Little, M. H. DevKidCC allows for robust classification
931 and direct comparisons of kidney organoid datasets. *bioRxiv*,
932 doi:10.1101/2021.01.20.427346 (2021).
- 933 14 Dressler, G. R. Advances in early kidney specification, development and patterning.
934 *Development* **136**, 3863-3874, doi:10.1242/dev.034876 (2009).
- 935 15 de Bakker, B. S., van den Hoff, M. J. B., Vize, P. D. & Oostra, R. J. The Pronephros; a
936 Fresh Perspective. *Integr Comp Biol* **59**, 29-47, doi:10.1093/icb/icz001 (2019).

- 937 16 Georgas, K. M., Chiu, H. S., Lesieur, E., Rumballe, B. A. & Little, M. H. Expression
938 of metanephric nephron-patterning genes in differentiating mesonephric tubules. *Dev
939 Dyn* **240**, 1600-1612, doi:10.1002/dvdy.22640 (2011).
- 940 17 Mugford, J. W., Sipila, P., Kobayashi, A., Behringer, R. R. & McMahon, A. P. Hoxd11
941 specifies a program of metanephric kidney development within the intermediate
942 mesoderm of the mouse embryo. *Dev Biol* **319**, 396-405,
943 doi:10.1016/j.ydbio.2008.03.044 (2008).
- 944 18 Tiedemann, K., Welling, L. W. & Basto, P. Structural and functional comparison of
945 mesonephric and metanephric proximal tubules. *Pediatr Nephrol* **1**, 297-305,
946 doi:10.1007/BF00849227 (1987).
- 947 19 Howden, S. E., Vanslambrouck, J. M., Wilson, S. B., Tan, K. S. & Little, M. H.
948 Reporter-based fate mapping in human kidney organoids confirms nephron lineage
949 relationships and reveals synchronous nephron formation. *EMBO Rep*,
950 doi:10.15252/embr.201847483 (2019).
- 951 20 Vanslambrouck, J. M., Wilson, S. B., Tan, K. S., Soo, J. Y., Scurr, M., Spijker, H. S.,
952 Starks, L. T., Neilson, A., Cui, X., Jain, S., Little, M. H. & Howden, S. E. A Toolbox
953 to Characterize Human Induced Pluripotent Stem Cell-Derived Kidney Cell Types and
954 Organoids. *J Am Soc Nephrol* **30**, 1811-1823, doi:10.1681/ASN.2019030303 (2019).
- 955 21 Little, M. H. & Combes, A. N. Kidney organoids: accurate models or fortunate
956 accidents. *Genes Dev* **33**, 1319-1345, doi:10.1101/gad.329573.119 (2019).
- 957 22 Brown, A. C., Muthukrishnan, S. D. & Oxburgh, L. A synthetic niche for nephron
958 progenitor cells. *Developmental cell* **34**, 229-241, doi:10.1016/j.devcel.2015.06.021
959 (2015).
- 960 23 Li, Z., Araoka, T., Wu, J., Liao, H. K., Li, M., Lazo, M., Zhou, B., Sui, Y., Wu, M. Z.,
961 Tamura, I., Xia, Y., Beyret, E., Matsusaka, T., Pastan, I., Rodriguez Esteban, C.,
962 Guillen, I., Guillen, P., Campistol, J. M. & Izpisua Belmonte, J. C. 3D Culture Supports
963 Long-Term Expansion of Mouse and Human Nephrogenic Progenitors. *Cell Stem Cell*
964 **19**, 516-529, doi:10.1016/j.stem.2016.07.016 (2016).
- 965 24 Tanigawa, S., Sharma, N., Hall, M. D., Nishinakamura, R. & Perantoni, A. O.
966 Preferential Propagation of Competent SIX2+ Nephronic Progenitors by LIF/ROCKi

- 967 Treatment of the Metanephric Mesenchyme. *Stem Cell Reports* **5**, 435-447,
968 doi:10.1016/j.stemcr.2015.07.015 (2015).
- 969 25 Tanigawa, S., Taguchi, A., Sharma, N., Perantoni, A. O. & Nishinakamura, R. Selective
970 In Vitro Propagation of Nephron Progenitors Derived from Embryos and Pluripotent
971 Stem Cells. *Cell reports* **15**, 801 - 813, doi:10.1016/j.celrep.2016.03.076 (2016).
- 972 26 Lindstrom, N. O., Lawrence, M. L., Burn, S. F., Johansson, J. A., Bakker, E. R.,
973 Ridgway, R. A., Chang, C. H., Karolak, M. J., Oxburgh, L., Headon, D. J., Sansom, O.
974 J., Smits, R., Davies, J. A. & Hohenstein, P. Integrated beta-catenin, BMP, PTEN, and
975 Notch signalling patterns the nephron. *eLife* **3**, e04000, doi:10.7554/eLife.04000
976 (2015).
- 977 27 Takasato, M., Er, P. X., Becroft, M., Vanslambrouck, J. M., Stanley, E. G., Elefanty,
978 A. G. & Little, M. H. Directing human embryonic stem cell differentiation towards a
979 renal lineage generates a self-organizing kidney. *Nature cell biology* **16**, 118-126,
980 doi:10.1038/ncb2894 (2014).
- 981 28 England, A. R., Chaney, C. P., Das, A., Patel, M., Malewska, A., Armendariz, D., Hon,
982 G. C., Strand, D. W., Drake, K. A. & Carroll, T. J. Identification and characterization
983 of cellular heterogeneity within the developing renal interstitium. *Development* **147**,
984 doi:10.1242/dev.190108 (2020).
- 985 29 Takasato, M., Er, P. X., Chiu, H. S. & Little, M. H. Generation of kidney organoids
986 from human pluripotent stem cells. *Nature protocols* **11**, 1681-1692,
987 doi:10.1038/nprot.2016.098 (2016).
- 988 30 Hochane, M., van den Berg, P. R., Fan, X., Berenger-Currias, N., Adegeest, E.,
989 Bialecka, M., Nieveen, M., Menschaart, M., Chuva de Sousa Lopes, S. M. & Semrau,
990 S. Single-cell transcriptomics reveals gene expression dynamics of human fetal kidney
991 development. *PLoS Biol* **17**, e3000152, doi:10.1371/journal.pbio.3000152 (2019).
- 992 31 Lindstrom, N. O., De Sena Brandine, G., Tran, T., Ransick, A., Suh, G., Guo, J., Kim,
993 A. D., Parvez, R. K., Ruffins, S. W., Rutledge, E. A., Thornton, M. E., Grubbs, B.,
994 McMahon, J. A., Smith, A. D. & McMahon, A. P. Progressive Recruitment of
995 Mesenchymal Progenitors Reveals a Time-Dependent Process of Cell Fate Acquisition
996 in Mouse and Human Nephrogenesis. *Developmental cell* **45**, 651-660 e654,
997 doi:10.1016/j.devcel.2018.05.010 (2018).

- 998 32 Lindstrom, N. O., Guo, J., Kim, A. D., Tran, T., Guo, Q., De Sena Brandine, G.,
999 Ransick, A., Parvez, R. K., Thornton, M. E., Basking, L., Grubbs, B., McMahon, J. A.,
1000 Smith, A. D. & McMahon, A. P. Conserved and Divergent Features of Mesenchymal
1001 Progenitor Cell Types within the Cortical Nephrogenic Niche of the Human and Mouse
1002 Kidney. *J Am Soc Nephrol* **29**, 806-824, doi:10.1681/ASN.2017080890 (2018).
- 1003 33 Kobayashi, A., Valerius, M. T., Mugford, J. W., Carroll, T. J., Self, M., Oliver, G. &
1004 McMahon, A. P. Six2 defines and regulates a multipotent self-renewing nephron
1005 progenitor population throughout mammalian kidney development. *Cell Stem Cell* **3**,
1006 169-181, doi:10.1016/j.stem.2008.05.020 (2008).
- 1007 34 Lindstrom, N. O., McMahon, J. A., Guo, J., Tran, T., Guo, Q., Rutledge, E., Parvez, R.
1008 K., Saribekyan, G., Schuler, R. E., Liao, C., Kim, A. D., Abdelhalim, A., Ruffins, S.
1009 W., Thornton, M. E., Baskin, L., Grubbs, B., Kesselman, C. & McMahon, A. P.
1010 Conserved and Divergent Features of Human and Mouse Kidney Organogenesis. *J Am
1011 Soc Nephrol* **29**, 785-805, doi:10.1681/ASN.2017080887 (2018).
- 1012 35 Lindstrom, N. O., Tran, T., Guo, J., Rutledge, E., Parvez, R. K., Thornton, M. E.,
1013 Grubbs, B., McMahon, J. A. & McMahon, A. P. Conserved and Divergent Molecular
1014 and Anatomic Features of Human and Mouse Nephron Patterning. *J Am Soc Nephrol*
1015 **29**, 825-840, doi:10.1681/ASN.2017091036 (2018).
- 1016 36 Hennigar, R. A., Schulte, B. A. & Spicer, S. S. Heterogeneous distribution of
1017 glycoconjugates in human kidney tubules. *The Anatomical record* **211**, 376-390,
1018 doi:10.1002/ar.1092110403 (1985).
- 1019 37 Low, J. H., Li, P., Chew, E. G. Y., Zhou, B., Suzuki, K., Zhang, T., Lian, M. M., Liu,
1020 M., Aizawa, E., Rodriguez Esteban, C., Yong, K. S. M., Chen, Q., Campistol, J. M.,
1021 Fang, M., Khor, C. C., Foo, J. N., Izpisua Belmonte, J. C. & Xia, Y. Generation of
1022 Human PSC-Derived Kidney Organoids with Patterned Nephron Segments and a De
1023 Novo Vascular Network. *Cell Stem Cell* **25**, 373-387 e379,
1024 doi:10.1016/j.stem.2019.06.009 (2019).
- 1025 38 Tran, T., Lindstrom, N. O., Ransick, A., De Sena Brandine, G., Guo, Q., Kim, A. D.,
1026 Der, B., Peti-Peterdi, J., Smith, A. D., Thornton, M., Grubbs, B., McMahon, J. A. &
1027 McMahon, A. P. In Vivo Developmental Trajectories of Human Podocyte Inform In

- 1028 Vitro Differentiation of Pluripotent Stem Cell-Derived Podocytes. *Developmental cell*
1029 **50**, 102-116 e106, doi:10.1016/j.devcel.2019.06.001 (2019).
- 1030 39 Holloway, E. M., Wu, J. H., Czerwinski, M., Sweet, C. W., Wu, A., Tsai, Y. H., Huang,
1031 S., Stoddard, A. E., Capeling, M. M., Glass, I. & Spence, J. R. Differentiation of Human
1032 Intestinal Organoids with Endogenous Vascular Endothelial Cells. *Developmental cell*
1033 **54**, 516-528 e517, doi:10.1016/j.devcel.2020.07.023 (2020).
- 1034 40 Czerniecki, S. M., Cruz, N. M., Harder, J. L., Menon, R., Annis, J., Otto, E. A., Gulieva,
1035 R. E., Islas, L. V., Kim, Y. K., Tran, L. M., Martins, T. J., Pippin, J. W., Fu, H., Kretzler,
1036 M., Shankland, S. J., Himmelfarb, J., Moon, R. T., Paragas, N. & Freedman, B. S. High-
1037 Throughput Screening Enhances Kidney Organoid Differentiation from Human
1038 Pluripotent Stem Cells and Enables Automated Multidimensional Phenotyping. *Cell*
1039 *Stem Cell* **22**, 929-940 e924, doi:10.1016/j.stem.2018.04.022 (2018).
- 1040 41 Harder, J. L., Menon, R., Otto, E. A., Zhou, J., Eddy, S., Wys, N. L., O'Connor, C.,
1041 Luo, J., Nair, V., Cebrian, C., Spence, J. R., Bitzer, M., Troyanskaya, O. G., Hodgin, J.
1042 B., Wiggins, R. C., Freedman, B. S., Kretzler, M., European Renal c, D. N. A. B. &
1043 Nephrotic Syndrome Study, N. Organoid single cell profiling identifies a transcriptional
1044 signature of glomerular disease. *JCI Insight* **4**, doi:10.1172/jci.insight.122697 (2019).
- 1045 42 Kumar, S. V., Er, P. X., Lawlor, K. T., Motazedian, A., Scurr, M., Ghobrial, I., Combes,
1046 A. N., Zappia, L., Oshlack, A., Stanley, E. G. & Little, M. H. Kidney micro-organoids
1047 in suspension culture as a scalable source of human pluripotent stem cell-derived
1048 kidney cells. *Development* **146**, doi:10.1242/dev.172361 (2019).
- 1049 43 Avissar, N., Ornt, D. B., Yagil, Y., Horowitz, S., Watkins, R. H., Kerl, E. A., Takahashi,
1050 K., Palmer, I. S. & Cohen, H. J. Human kidney proximal tubules are the main source
1051 of plasma glutathione peroxidase. *Am J Physiol* **266**, C367-375,
1052 doi:10.1152/ajpcell.1994.266.2.C367 (1994).
- 1053 44 Palacin, M., Fernandez, E., Chillaron, J. & Zorzano, A. The amino acid transport system
1054 b(o,+) and cystinuria. *Mol Membr Biol* **18**, 21-26 (2001).
- 1055 45 Schuh, C. D., Polesel, M., Platonova, E., Haenni, D., Gassama, A., Tokonami, N.,
1056 Ghazi, S., Bugarski, M., Devuyst, O., Ziegler, U. & Hall, A. M. Combined Structural
1057 and Functional Imaging of the Kidney Reveals Major Axial Differences in Proximal

- 1058 Tubule Endocytosis. *J Am Soc Nephrol* **29**, 2696-2712, doi:10.1681/ASN.2018050522
1059 (2018).
- 1060 46 Verrey, F., Ristic, Z., Romeo, E., Ramadan, T., Makrides, V., Dave, M. H., Wagner, C.
1061 A. & Camargo, S. M. Novel renal amino acid transporters. *Annu Rev Physiol* **67**, 557-
1062 572, doi:10.1146/annurev.physiol.67.031103.153949 (2005).
- 1063 47 Fenollar-Ferrer, C., Forster, I. C., Patti, M., Knoepfel, T., Werner, A. & Forrest, L. R.
1064 Identification of the first sodium binding site of the phosphate cotransporter NaPi-IIa
1065 (SLC34A1). *Biophys J* **108**, 2465-2480, doi:10.1016/j.bpj.2015.03.054 (2015).
- 1066 48 Hummel, C. S., Lu, C., Loo, D. D., Hirayama, B. A., Voss, A. A. & Wright, E. M.
1067 Glucose transport by human renal Na+/D-glucose cotransporters SGLT1 and SGLT2.
1068 *Am J Physiol Cell Physiol* **300**, C14-21, doi:10.1152/ajpcell.00388.2010 (2011).
- 1069 49 Rahmoune, H., Thompson, P. W., Ward, J. M., Smith, C. D., Hong, G. & Brown, J.
1070 Glucose transporters in human renal proximal tubular cells isolated from the urine of
1071 patients with non-insulin-dependent diabetes. *Diabetes* **54**, 3427-3434,
1072 doi:10.2337/diabetes.54.12.3427 (2005).
- 1073 50 Wood, I. S. & Trayhurn, P. Glucose transporters (GLUT and SGLT): expanded families
1074 of sugar transport proteins. *Br J Nutr* **89**, 3-9, doi:10.1079/BJN2002763 (2003).
- 1075 51 Nagamori, S., Wiriyasermkul, P., Guarch, M. E., Okuyama, H., Nakagomi, S.,
1076 Tadagaki, K., Nishinaka, Y., Bodoy, S., Takafuji, K., Okuda, S., Kurokawa, J., Ohgaki,
1077 R., Nunes, V., Palacin, M. & Kanai, Y. Novel cystine transporter in renal proximal
1078 tubule identified as a missing partner of cystinuria-related plasma membrane protein
1079 rBAT/SLC3A1. *Proc Natl Acad Sci U S A* **113**, 775-780, doi:10.1073/pnas.1519959113
1080 (2016).
- 1081 52 Otsuka, M., Matsumoto, T., Morimoto, R., Arioka, S., Omote, H. & Moriyama, Y. A
1082 human transporter protein that mediates the final excretion step for toxic organic
1083 cations. *Proc Natl Acad Sci U S A* **102**, 17923-17928, doi:10.1073/pnas.0506483102
1084 (2005).
- 1085 53 Vogetseder, A., Picard, N., Gaspert, A., Walch, M., Kaissling, B. & Le Hir, M.
1086 Proliferation capacity of the renal proximal tubule involves the bulk of differentiated

- 1087 epithelial cells. *Am J Physiol Cell Physiol* **294**, C22-28,
1088 doi:10.1152/ajpcell.00227.2007 (2008).
- 1089 54 Nielsen, R., Christensen, E. I. & Birn, H. Megalin and cubilin in proximal tubule protein
1090 reabsorption: from experimental models to human disease. *Kidney Int* **89**, 58-67,
1091 doi:10.1016/j.kint.2015.11.007 (2016).
- 1092 55 Kowalcuk, S., Broer, A., Tietze, N., Vanslambrouck, J. M., Rasko, J. E. & Broer, S.
1093 A protein complex in the brush-border membrane explains a Hartnup disorder allele.
1094 *FASEB J* **22**, 2880-2887, doi:fj.08-107300 [pii]
- 1095 10.1096/fj.08-107300 (2008).
- 1096 56 Kanai, Y., Fukasawa, Y., Cha, S. H., Segawa, H., Chairoungdua, A., Kim, D. K.,
1097 Matsuo, H., Kim, J. Y., Miyamoto, K., Takeda, E. & Endou, H. Transport properties of
1098 a system y+L neutral and basic amino acid transporter. Insights into the mechanisms of
1099 substrate recognition. *J Biol Chem* **275**, 20787-20793, doi:10.1074/jbc.M000634200
1100 (2000).
- 1101 57 Verrey, F. System L: heteromeric exchangers of large, neutral amino acids involved in
1102 directional transport. *Pflugers Arch* **445**, 529-533, doi:10.1007/s00424-002-0973-z
1103 (2003).
- 1104 58 Lee, J. W., Chou, C. L. & Knepper, M. A. Deep Sequencing in Microdissected Renal
1105 Tubules Identifies Nephron Segment-Specific Transcriptomes. *J Am Soc Nephrol* **26**,
1106 2669-2677, doi:10.1681/ASN.2014111067 (2015).
- 1107 59 Camargo, S. M., Singer, D., Makrides, V., Huggel, K., Pos, K. M., Wagner, C. A.,
1108 Kuba, K., Danilczyk, U., Skovby, F., Kleta, R., Penninger, J. M. & Verrey, F. Tissue-
1109 specific amino acid transporter partners ACE2 and collectrin differentially interact with
1110 hartnup mutations. *Gastroenterology* **136**, 872-882, doi:10.1053/j.gastro.2008.10.055
1111 (2009).
- 1112 60 Fyfe, J. C., Madsen, M., Hojrup, P., Christensen, E. I., Tanner, S. M., de la Chapelle,
1113 A., He, Q. & Moestrup, S. K. The functional cobalamin (vitamin B12)-intrinsic factor
1114 receptor is a novel complex of cubilin and amnionless. *Blood* **103**, 1573-1579,
1115 doi:10.1182/blood-2003-08-2852 (2004).

- 1116 61 Ahuja, R., Yammani, R., Bauer, J. A., Kalra, S., Seetharam, S. & Seetharam, B.
1117 Interactions of cubilin with megalin and the product of the amnionless gene (AMN):
1118 effect on its stability. *Biochem J* **410**, 301-308, doi:10.1042/BJ20070919 (2008).
- 1119 62 Das, A., Tanigawa, S., Karner, C. M., Xin, M., Lum, L., Chen, C., Olson, E. N.,
1120 Perantoni, A. O. & Carroll, T. J. Stromal-epithelial crosstalk regulates kidney
1121 progenitor cell differentiation. *Nature cell biology* **15**, 1035-1044,
1122 doi:10.1038/ncb2828 (2013).
- 1123 63 Yoshimura, Y., Taguchi, A., Tanigawa, S., Yatsuda, J., Kamba, T., Takahashi, S.,
1124 Kurihara, H., Mukoyama, M. & Nishinakamura, R. Manipulation of Nephron-
1125 Patterning Signals Enables Selective Induction of Podocytes from Human Pluripotent
1126 Stem Cells. *J Am Soc Nephrol* **30**, 304-321, doi:10.1681/ASN.2018070747 (2019).
- 1127 64 Tanigawa, S., Tanaka, E., Miike, K., Ohmori, T., Inoue, D., Cai, C. L., Taguchi, A.,
1128 Kobayashi, A. & Nishinakamura, R. Generation of the organotypic kidney structure by
1129 integrating pluripotent stem cell-derived renal stroma. *Nature communications* **13**, 611,
1130 doi:10.1038/s41467-022-28226-7 (2022).
- 1131 65 Menon, R., Otto, E. A., Kokoruda, A., Zhou, J., Zhang, Z., Yoon, E., Chen, Y. C.,
1132 Troyanskaya, O., Spence, J. R., Kretzler, M. & Cebrian, C. Single-cell analysis of
1133 progenitor cell dynamics and lineage specification in the human fetal kidney.
1134 *Development* **145**, doi:10.1242/dev.164038 (2018).
- 1135 66 Zhu, Y., Oganesian, A., Keene, D. R. & Sandell, L. J. Type IIA procollagen containing
1136 the cysteine-rich amino propeptide is deposited in the extracellular matrix of
1137 prechondrogenic tissue and binds to TGF-beta1 and BMP-2. *J Cell Biol* **144**, 1069-
1138 1080, doi:10.1083/jcb.144.5.1069 (1999).
- 1139 67 Cao, J., O'Day, D. R., Pliner, H. A., Kingsley, P. D., Deng, M., Daza, R. M., Zager, M.
1140 A., Aldinger, K. A., Blecher-Gonen, R., Zhang, F., Spielmann, M., Palis, J., Doherty,
1141 D., Steemers, F. J., Glass, I. A., Trapnell, C. & Shendure, J. A human cell atlas of fetal
1142 gene expression. *Science* **370**, doi:10.1126/science.aba7721 (2020).
- 1143 68 Gunaydin, H., Gu, Y. & Huang, X. Novel binding mode of a potent and selective
1144 tankyrase inhibitor. *PLoS One* **7**, e33740, doi:10.1371/journal.pone.0033740 (2012).

- 1145 69 Lawlor, K. T., Vanslambrouck, J. M., Higgins, J. W., Chambon, A., Bishard, K., Arndt,
1146 D., Er, P. X., Wilson, S. B., Howden, S. E., Tan, K. S., Li, F., Hale, L. J., Shepherd, B.,
1147 Pentoney, S., Presnell, S. C., Chen, A. E. & Little, M. H. Cellular extrusion bioprinting
1148 improves kidney organoid reproducibility and conformation. *Nat Mater* **20**, 260-271,
1149 doi:10.1038/s41563-020-00853-9 (2021).
- 1150 70 Yasujima, T., Ohta, K. Y., Inoue, K., Ishimaru, M. & Yuasa, H. Evaluation of 4',6'-
1151 diaminido-2-phenylindole as a fluorescent probe substrate for rapid assays of the
1152 functionality of human multidrug and toxin extrusion proteins. *Drug Metab Dispos* **38**,
1153 715-721, doi:10.1124/dmd.109.030221 (2010).
- 1154 71 Ozkok, A. & Edelstein, C. L. Pathophysiology of cisplatin-induced acute kidney injury.
1155 *Biomed Res Int* **2014**, 967826, doi:10.1155/2014/967826 (2014).
- 1156 72 Yao, X., Panichpisal, K., Kurtzman, N. & Nugent, K. Cisplatin nephrotoxicity: a
1157 review. *Am J Med Sci* **334**, 115-124, doi:10.1097/MAJ.0b013e31812dfe1e (2007).
- 1158 73 Abdelsalam, M., Elmorsy, E., Abdelwahab, H., Alghary, O., Naguib, M., El Wahab,
1159 A. A., Eldeeb, A., Eltoraby, E., Abdelsalam, A., Sabry, A., El-Metwally, M., Akl, M.,
1160 Anber, N., El Sayed Zaki, M., Almutairi, F. & Mansour, T. Urinary biomarkers for
1161 early detection of platinum based drugs induced nephrotoxicity. *BMC Nephrol* **19**, 219,
1162 doi:10.1186/s12882-018-1022-2 (2018).
- 1163 74 Chiusolo, A., Defazio, R., Zanetti, E., Mongillo, M., Mori, N., Cristofori, P. & Trevisan,
1164 A. Kidney injury molecule-1 expression in rat proximal tubule after treatment with
1165 segment-specific nephrotoxicants: a tool for early screening of potential kidney
1166 toxicity. *Toxicol Pathol* **38**, 338-345, doi:10.1177/0192623310362244 (2010).
- 1167 75 Sasaki, D., Yamada, A., Umeno, H., Kurihara, H., Nakatsuji, S., Fujihira, S., Tsubota,
1168 K., Ono, M., Moriguchi, A., Watanabe, K. & Seki, J. Comparison of the course of
1169 biomarker changes and kidney injury in a rat model of drug-induced acute kidney
1170 injury. *Biomarkers* **16**, 553-566, doi:10.3109/1354750X.2011.613123 (2011).
- 1171 76 Shinke, H., Masuda, S., Togashi, Y., Ikemi, Y., Ozawa, A., Sato, T., Kim, Y. H.,
1172 Mishima, M., Ichimura, T., Bonventre, J. V. & Matsubara, K. Urinary kidney injury
1173 molecule-1 and monocyte chemotactic protein-1 are noninvasive biomarkers of
1174 cisplatin-induced nephrotoxicity in lung cancer patients. *Cancer Chemother Pharmacol*
1175 **76**, 989-996, doi:10.1007/s00280-015-2880-y (2015).

- 1176 77 Vaidya, V. S., Ozer, J. S., Dieterle, F., Collings, F. B., Ramirez, V., Troth, S.,
1177 Muniappa, N., Thudium, D., Gerhold, D., Holder, D. J., Bobadilla, N. A., Marrer, E.,
1178 Perentes, E., Cordier, A., Vonderscher, J., Maurer, G., Goering, P. L., Sistare, F. D. &
1179 Bonventre, J. V. Kidney injury molecule-1 outperforms traditional biomarkers of
1180 kidney injury in preclinical biomarker qualification studies. *Nature biotechnology* **28**,
1181 478-485, doi:10.1038/nbt.1623 (2010).
- 1182 78 Digby, J. L. M., Vanichapol, T., Przepiorski, A., Davidson, A. J. & Sander, V.
1183 Evaluation of cisplatin-induced injury in human kidney organoids. *Am J Physiol Renal
1184 Physiol* **318**, F971-F978, doi:10.1152/ajprenal.00597.2019 (2020).
- 1185 79 Cruz, N. M., Song, X., Czerniecki, S. M., Gulieva, R. E., Churchill, A. J., Kim, Y. K.,
1186 Winston, K., Tran, L. M., Diaz, M. A., Fu, H., Finn, L. S., Pei, Y., Himmelfarb, J. &
1187 Freedman, B. S. Organoid cystogenesis reveals a critical role of microenvironment in
1188 human polycystic kidney disease. *Nat Mater* **16**, 1112-1119, doi:10.1038/nmat4994
1189 (2017).
- 1190 80 Forbes, T. A., Howden, S. E., Lawlor, K., Phipson, B., Maksimovic, J., Hale, L.,
1191 Wilson, S., Quinlan, C., Ho, G., Holman, K., Bennetts, B., Crawford, J., Trnka, P.,
1192 Oshlack, A., Patel, C., Mallett, A., Simons, C. & Little, M. H. Patient-iPSC-Derived
1193 Kidney Organoids Show Functional Validation of a Ciliopathic Renal Phenotype and
1194 Reveal Underlying Pathogenetic Mechanisms. *Am J Hum Genet* **102**, 816-831,
1195 doi:10.1016/j.ajhg.2018.03.014 (2018).
- 1196 81 Hale, L. J., Howden, S. E., Phipson, B., Lonsdale, A., Er, P. X., Ghobrial, I., Hosawi,
1197 S., Wilson, S., Lawlor, K. T., Khan, S., Oshlack, A., Quinlan, C., Lennon, R. & Little,
1198 M. H. 3D organoid-derived human glomeruli for personalised podocyte disease
1199 modelling and drug screening. *Nature communications* **9**, 5167, doi:10.1038/s41467-
1200 018-07594-z (2018).
- 1201 82 Hollywood, J. A., Przepiorski, A., D'Souza, R. F., Sreebhavan, S., Wolvetang, E. J.,
1202 Harrison, P. T., Davidson, A. J. & Holm, T. M. Use of Human Induced Pluripotent
1203 Stem Cells and Kidney Organoids To Develop a Cysteamine/mTOR Inhibition
1204 Combination Therapy for Cystinosis. *J Am Soc Nephrol* **31**, 962-982,
1205 doi:10.1681/ASN.2019070712 (2020).

- 1206 83 Mae, S., Shono, A., Shiota, F., Yasuno, T., Kajiwara, M., Gotoda-Nishimura, N., Arai,
1207 S., Sato-Otubo, A., Toyoda, T., Takahashi, K., Nakayama, N., Cowan, C. A., Aoi, T.,
1208 Ogawa, S., McMahon, A. P., Yamanaka, S. & Osafune, K. Monitoring and robust
1209 induction of nephrogenic intermediate mesoderm from human pluripotent stem cells.
1210 *Nature communications* **4**, 1367, doi:10.1038/ncomms2378 (2013).
- 1211 84 Przepiorski, A., Sander, V., Tran, T., Hollywood, J. A., Sorrenson, B., Shih, J. H.,
1212 Wolvetang, E. J., McMahon, A. P., Holm, T. M. & Davidson, A. J. A Simple
1213 Bioreactor-Based Method to Generate Kidney Organoids from Pluripotent Stem Cells.
1214 *Stem Cell Reports* **11**, 470-484, doi:10.1016/j.stemcr.2018.06.018 (2018).
- 1215 85 Tanigawa, S., Islam, M., Sharmin, S., Naganuma, H., Yoshimura, Y., Haque, F., Era,
1216 T., Nakazato, H., Nakanishi, K., Sakuma, T., Yamamoto, T., Kurihara, H., Taguchi, A.
1217 & Nishinakamura, R. Organoids from Nephrotic Disease-Derived iPSCs Identify
1218 Impaired NEPHRIN Localization and Slit Diaphragm Formation in Kidney Podocytes.
1219 *Stem Cell Reports* **11**, 727-740, doi:10.1016/j.stemcr.2018.08.003 (2018).
- 1220 86 Han, L., Wei, X., Liu, C., Volpe, G., Wang, Z., Pan, T., Yuan, Y., Lei, Y., Lai, Y.,
1221 Ward, C., Yu, Y., Wang, M., Shi, Q., Wu, T., Wu, L., Liu, Y., Wang, C., Zhang, Y.,
1222 Sun, H., Yu, H., Zhuang, Z., Tang, T., Huang, Y., Lu, H., Xu, L., Xu, J., Cheng, M.,
1223 Liu, Y., Wong, C. W., Tan, T., Ji, W., Maxwell, P. H., Yang, H., Wang, J., Zhu, S., Liu,
1224 S., Xu, X., Hou, Y., Esteban, M. A., Liu, L. & Consortium, S. C. G. B. A.-S. C. Single-
1225 cell atlas of a non-human primate reveals new pathogenic mechanisms of COVID-19.
1226 2020.2004.2010.022103, doi:10.1101/2020.04.10.022103 %J bioRxiv (2020).
- 1227 87 Marchiano, S., Hsiang, T. Y., Khanna, A., Higashi, T., Whitmore, L. S., Bargehr, J.,
1228 Davaapil, H., Chang, J., Smith, E., Ong, L. P., Colzani, M., Reinecke, H., Yang, X.,
1229 Pabon, L., Sinha, S., Najafian, B., Sniadecki, N. J., Bertero, A., Gale, M., Jr. & Murry,
1230 C. E. SARS-CoV-2 Infects Human Pluripotent Stem Cell-Derived Cardiomyocytes,
1231 Impairing Electrical and Mechanical Function. *Stem Cell Reports* **16**, 478-492,
1232 doi:10.1016/j.stemcr.2021.02.008 (2021).
- 1233 88 Mills, R. J., Humphrey, S. J., Fortuna, P. R. J., Lor, M., Foster, S. R., Quaife-Ryan, G.
1234 A., Johnston, R. L., Dumenil, T., Bishop, C., Rudraraju, R., Rawle, D. J., Le, T., Zhao,
1235 W., Lee, L., Mackenzie-Kludas, C., Mehdiabadi, N. R., Halliday, C., Gilham, D., Fu,
1236 L., Nicholls, S. J., Johansson, J., Sweeney, M., Wong, N. C. W., Kulikowski, E.,
1237 Sokolowski, K. A., Tse, B. W. C., Devilee, L., Voges, H. K., Reynolds, L. T.,

- 1238 Krumeich, S., Mathieson, E., Abu-Bonsrah, D., Karavendzas, K., Griffen, B., Titmarsh,
1239 D., Elliott, D. A., McMahon, J., Suhrbier, A., Subbarao, K., Porrello, E. R., Smyth, M.
1240 J., Engwerda, C. R., MacDonald, K. P. A., Bald, T., James, D. E. & Hudson, J. E. BET
1241 inhibition blocks inflammation-induced cardiac dysfunction and SARS-CoV-2
1242 infection. *Cell* **184**, 2167-2182 e2122, doi:10.1016/j.cell.2021.03.026 (2021).
- 1243 89 Sharma, A., Garcia, G., Jr., Wang, Y., Plummer, J. T., Morizono, K., Arumugaswami,
1244 V. & Svendsen, C. N. Human iPSC-Derived Cardiomyocytes Are Susceptible to
1245 SARS-CoV-2 Infection. *Cell Rep Med* **1**, 100052, doi:10.1016/j.xcrm.2020.100052
1246 (2020).
- 1247 90 Tiwari, S. K., Wang, S., Smith, D., Carlin, A. F. & Rana, T. M. Revealing Tissue-
1248 Specific SARS-CoV-2 Infection and Host Responses using Human Stem Cell-Derived
1249 Lung and Cerebral Organoids. *Stem Cell Reports* **16**, 437-445,
1250 doi:10.1016/j.stemcr.2021.02.005 (2021).
- 1251 91 Huang, C., Wang, Y., Li, X., Ren, L., Zhao, J., Hu, Y., Zhang, L., Fan, G., Xu, J., Gu,
1252 X., Cheng, Z., Yu, T., Xia, J., Wei, Y., Wu, W., Xie, X., Yin, W., Li, H., Liu, M., Xiao,
1253 Y., Gao, H., Guo, L., Xie, J., Wang, G., Jiang, R., Gao, Z., Jin, Q., Wang, J. & Cao, B.
1254 Clinical features of patients infected with 2019 novel coronavirus in Wuhan, China.
1255 *Lancet* **395**, 497-506, doi:10.1016/S0140-6736(20)30183-5 (2020).
- 1256 92 Kunutsor, S. K. & Laukkanen, J. A. Renal complications in COVID-19: a systematic
1257 review and meta-analysis. *Ann Med* **52**, 345-353, doi:10.1080/07853890.2020.1790643
1258 (2020).
- 1259 93 Yang, X., Yu, Y., Xu, J., Shu, H., Xia, J., Liu, H., Wu, Y., Zhang, L., Yu, Z., Fang, M.,
1260 Yu, T., Wang, Y., Pan, S., Zou, X., Yuan, S. & Shang, Y. Clinical course and outcomes
1261 of critically ill patients with SARS-CoV-2 pneumonia in Wuhan, China: a single-
1262 centered, retrospective, observational study. *Lancet Respir Med* **8**, 475-481,
1263 doi:10.1016/S2213-2600(20)30079-5 (2020).
- 1264 94 Zhou, F., Yu, T., Du, R., Fan, G., Liu, Y., Liu, Z., Xiang, J., Wang, Y., Song, B., Gu,
1265 X., Guan, L., Wei, Y., Li, H., Wu, X., Xu, J., Tu, S., Zhang, Y., Chen, H. & Cao, B.
1266 Clinical course and risk factors for mortality of adult inpatients with COVID-19 in
1267 Wuhan, China: a retrospective cohort study. *Lancet* **395**, 1054-1062,
1268 doi:10.1016/S0140-6736(20)30566-3 (2020).

- 1269 95 Monteil, V., Kwon, H., Prado, P., Hagelkruys, A., Wimmer, R. A., Stahl, M., Leopoldi,
1270 A., Garreta, E., Hurtado Del Pozo, C., Prosper, F., Romero, J. P., Wirnsberger, G.,
1271 Zhang, H., Slutsky, A. S., Conder, R., Montserrat, N., Mirazimi, A. & Penninger, J. M.
1272 Inhibition of SARS-CoV-2 Infections in Engineered Human Tissues Using Clinical-
1273 Grade Soluble Human ACE2. *Cell* **181**, 905-913 e907, doi:10.1016/j.cell.2020.04.004
1274 (2020).
- 1275 96 Wysocki, J., Ye, M., Hassler, L., Gupta, A. K., Wang, Y., Nicoleascu, V., Randall, G.,
1276 Wertheim, J. A. & Batlle, D. A Novel Soluble ACE2 Variant with Prolonged Duration
1277 of Action Neutralizes SARS-CoV-2 Infection in Human Kidney Organoids. *J Am Soc
1278 Nephrol*, doi:10.1681/ASN.2020101537 (2021).
- 1279 97 Motavalli, R., Abdelbasset, W. K., Rahman, H. S., Achmad, M. H., Sergeevna, N. K.,
1280 Zekiy, A. O., Adili, A., Khiavi, F. M., Marofi, F., Yousefi, M., Ghoreishizadeh, S.,
1281 Shomali, N., Etemadi, J. & Jarahian, M. The lethal internal face of the coronaviruses:
1282 Kidney tropism of the SARS, MERS, and COVID19 viruses. *IUBMB Life* **73**, 1005-
1283 1015, doi:10.1002/iub.2516 (2021).
- 1284 98 Hoffmann, M., Kleine-Weber, H., Schroeder, S., Kruger, N., Herrler, T., Erichsen, S.,
1285 Schiergens, T. S., Herrler, G., Wu, N. H., Nitsche, A., Muller, M. A., Drosten, C. &
1286 Pohlmann, S. SARS-CoV-2 Cell Entry Depends on ACE2 and TMPRSS2 and Is
1287 Blocked by a Clinically Proven Protease Inhibitor. *Cell* **181**, 271-280 e278,
1288 doi:10.1016/j.cell.2020.02.052 (2020).
- 1289 99 Braun, F., Lutgehetmann, M., Pfefferle, S., Wong, M. N., Carsten, A., Lindenmeyer,
1290 M. T., Norz, D., Heinrich, F., Meissner, K., Wichmann, D., Kluge, S., Gross, O.,
1291 Pueschel, K., Schroder, A. S., Edler, C., Aepfelbacher, M., Puelles, V. G. & Huber, T.
1292 B. SARS-CoV-2 renal tropism associates with acute kidney injury. *Lancet* **396**, 597-
1293 598, doi:10.1016/S0140-6736(20)31759-1 (2020).
- 1294 100 Farkash, E. A., Wilson, A. M. & Jentzen, J. M. Ultrastructural Evidence for Direct
1295 Renal Infection with SARS-CoV-2. *J Am Soc Nephrol* **31**, 1683-1687,
1296 doi:10.1681/ASN.2020040432 (2020).
- 1297 101 Kissling, S., Rotman, S., Gerber, C., Halfon, M., Lamoth, F., Comte, D., Lhopitallier,
1298 L., Sadallah, S. & Fakhouri, F. Collapsing glomerulopathy in a COVID-19 patient.
1299 *Kidney Int* **98**, 228-231, doi:10.1016/j.kint.2020.04.006 (2020).

- 1300 102 Puelles, V. G., Lutgehetmann, M., Lindenmeyer, M. T., Sperhake, J. P., Wong, M. N.,
1301 Allweiss, L., Chilla, S., Heinemann, A., Wanner, N., Liu, S., Braun, F., Lu, S., Pfefferle,
1302 S., Schroder, A. S., Edler, C., Gross, O., Glatzel, M., Wichmann, D., Wiech, T., Kluge,
1303 S., Pueschel, K., Aepfelbacher, M. & Huber, T. B. Multiorgan and Renal Tropism of
1304 SARS-CoV-2. *N Engl J Med* **383**, 590-592, doi:10.1056/NEJMc2011400 (2020).
- 1305 103 Su, H., Yang, M., Wan, C., Yi, L. X., Tang, F., Zhu, H. Y., Yi, F., Yang, H. C., Fogo,
1306 A. B., Nie, X. & Zhang, C. Renal histopathological analysis of 26 postmortem findings
1307 of patients with COVID-19 in China. *Kidney Int* **98**, 219-227,
1308 doi:10.1016/j.kint.2020.04.003 (2020).
- 1309 104 Werion, A., Belkhir, L., Perrot, M., Schmit, G., Aydin, S., Chen, Z., Penaloza, A., De
1310 Greef, J., Yildiz, H., Pothen, L., Yombi, J. C., Dewulf, J., Scohy, A., Gerard, L.,
1311 Wittebole, X., Laterre, P. F., Miller, S. E., Devuyst, O., Jadoul, M., Morelle, J. &
1312 Cliniques universitaires Saint-Luc, C.-R. G. SARS-CoV-2 causes a specific
1313 dysfunction of the kidney proximal tubule. *Kidney Int* **98**, 1296-1307,
1314 doi:10.1016/j.kint.2020.07.019 (2020).
- 1315 105 Hanley, B., Naresh, K. N., Roufosse, C., Nicholson, A. G., Weir, J., Cooke, G. S.,
1316 Thursz, M., Manousou, P., Corbett, R., Goldin, R., Al-Sarraj, S., Abdolrasouli, A.,
1317 Swann, O. C., Baillon, L., Penn, R., Barclay, W. S., Viola, P. & Osborn, M.
1318 Histopathological findings and viral tropism in UK patients with severe fatal COVID-
1319 19: a post-mortem study. *Lancet Microbe* **1**, e245-e253, doi:10.1016/S2666-
1320 5247(20)30115-4 (2020).
- 1321 106 Amraei, R., Yin, W., Napoleon, M. A., Suder, E. L., Berrigan, J., Zhao, Q., Olejnik, J.,
1322 Chandler, K. B., Xia, C., Feldman, J., Hauser, B. M., Caradonna, T. M., Schmidt, A.
1323 G., Gummuluru, S., Muhlberger, E., Chitalia, V., Costello, C. E. & Rahimi, N.
1324 CD209L/L-SIGN and CD209/DC-SIGN act as receptors for SARS-CoV-2. *bioRxiv*,
1325 doi:10.1101/2020.06.22.165803 (2021).
- 1326 107 Singh, M., Bansal, V. & Feschotte, C. A Single-Cell RNA Expression Map of Human
1327 Coronavirus Entry Factors. *Cell reports* **32**, 108175, doi:10.1016/j.celrep.2020.108175
1328 (2020).
- 1329 108 Kuppe, C., Leuchtle, K., Wagner, A., Kabgani, N., Saritas, T., Puelles, V. G., Smeets,
1330 B., Hakroush, S., van der Vlag, J., Boor, P., Schiffer, M., Grone, H. J., Fogo, A., Floege,

- 1331 J. & Moeller, M. J. Novel parietal epithelial cell subpopulations contribute to focal
1332 segmental glomerulosclerosis and glomerular tip lesions. *Kidney Int* **96**, 80-93,
1333 doi:10.1016/j.kint.2019.01.037 (2019).
- 1334 109 Wang, M. Not your usual parietal cell. *Nature reviews. Nephrology* **15**, 318,
1335 doi:10.1038/s41581-019-0141-8 (2019).
- 1336 110 Broer, S., Bailey, C. G., Kowalcuk, S., Ng, C., Vanslambrouck, J. M., Rodgers, H.,
1337 Auray-Blais, C., Cavanaugh, J. A., Broer, A. & Rasko, J. E. Iminoglycinuria and
1338 hyperglycinuria are discrete human phenotypes resulting from complex mutations in
1339 proline and glycine transporters. *J Clin Invest* **118**, 3881-3892, doi:10.1172/JCI36625
1340 36625 [pii] (2008).
- 1341 111 Hou, Y. J., Okuda, K., Edwards, C. E., Martinez, D. R., Asakura, T., Dinnon, K. H.,
1342 3rd, Kato, T., Lee, R. E., Yount, B. L., Mascenik, T. M., Chen, G., Olivier, K. N., Ghio,
1343 A., Tse, L. V., Leist, S. R., Gralinski, L. E., Schafer, A., Dang, H., Gilmore, R., Nakano,
1344 S., Sun, L., Fulcher, M. L., Livraghi-Butrico, A., Nicely, N. I., Cameron, M., Cameron,
1345 C., Kelvin, D. J., de Silva, A., Margolis, D. M., Markmann, A., Bartelt, L., Zumwalt,
1346 R., Martinez, F. J., Salvatore, S. P., Borczuk, A., Tata, P. R., Sontake, V., Kimple, A.,
1347 Jaspers, I., O'Neal, W. K., Randell, S. H., Boucher, R. C. & Baric, R. S. SARS-CoV-2
1348 Reverse Genetics Reveals a Variable Infection Gradient in the Respiratory Tract. *Cell*
1349 **182**, 429-446 e414, doi:10.1016/j.cell.2020.05.042 (2020).
- 1350 112 Chen, Z., Hu, J., Liu, L., Chen, R., Wang, M., Xiong, M., Li, Z. Q., Zhao, Y., Li, H.,
1351 Guan, C., Zhang, J., Liu, L., Chen, K. & Wang, Y. M. SARS-CoV-2 Causes Acute
1352 Kidney Injury by Directly Infecting Renal Tubules. *Front Cell Dev Biol* **9**, 664868,
1353 doi:10.3389/fcell.2021.664868 (2021).
- 1354 113 Jansen, J., Reimer, K. C., Nagai, J. S., Varghese, F. S., Overheul, G. J., de Beer, M.,
1355 Roverts, R., Daviran, D., Fermin, L. A. S., Willemse, B., Beukenboom, M., Djurdjaj,
1356 S., von Stillfried, S., van Eijk, L. E., Mastik, M., Bulthuis, M., Dunnen, W. D., van
1357 Goor, H., Hillebrands, J. L., Triana, S. H., Alexandrov, T., Timm, M. C., van den Berge,
1358 B. T., van den Broek, M., Nlandu, Q., Heijnert, J., Bindels, E. M. J., Hoogenboezem,
1359 R. M., Mooren, F., Kuppe, C., Miesen, P., Grunberg, K., Ijzermans, T., Steenbergen,
1360 E. J., Czogalla, J., Schreuder, M. F., Sommerdijk, N., Akiva, A., Boor, P., Puelles, V.
1361 G., Floege, J., Huber, T. B., consortium, C. M., van Rij, R. P., Costa, I. G., Schneider,

- 1362 R. K., Smeets, B. & Kramann, R. SARS-CoV-2 infects the human kidney and drives
1363 fibrosis in kidney organoids. *Cell Stem Cell* **29**, 217-231 e218,
1364 doi:10.1016/j.stem.2021.12.010 (2022).
- 1365 114 V'Kovski, P., Kratzel, A., Steiner, S., Stalder, H. & Thiel, V. Coronavirus biology and
1366 replication: implications for SARS-CoV-2. *Nat Rev Microbiol* **19**, 155-170,
1367 doi:10.1038/s41579-020-00468-6 (2021).
- 1368 115 Zlacka, J., Stebelova, K., Zeman, M. & Herichova, I. Interactions of renin-angiotensin
1369 system and COVID-19: the importance of daily rhythms in ACE2, ADAM17 and
1370 TMPRSS2 expression. *Physiol Res* **70**, S177-S194, doi:10.33549/physiolres.934754
1371 (2021).
- 1372 116 Jackson, C. B., Farzan, M., Chen, B. & Choe, H. Mechanisms of SARS-CoV-2 entry
1373 into cells. *Nat Rev Mol Cell Biol* **23**, 3-20, doi:10.1038/s41580-021-00418-x (2022).
- 1374 117 Muus, C., Luecken, M. D., Eraslan, G., Sikkema, L., Waghray, A., Heimberg, G.,
1375 Kobayashi, Y., Vaishnav, E. D., Subramanian, A., Smillie, C., Jagadeesh, K. A.,
1376 Duong, E. T., Fiskin, E., Torlai Triglia, E., Ansari, M., Cai, P., Lin, B., Buchanan, J.,
1377 Chen, S., Shu, J., Haber, A. L., Chung, H., Montoro, D. T., Adams, T., Aliee, H., Allon,
1378 S. J., Andrusivova, Z., Angelidis, I., Ashenberg, O., Bassler, K., Becavin, C., Benhar,
1379 I., Bergenstrahle, J., Bergenstrahle, L., Bolt, L., Braun, E., Bui, L. T., Callori, S.,
1380 Chaffin, M., Chichelnitskiy, E., Chiou, J., Conlon, T. M., Cuoco, M. S., Cuomo, A. S.
1381 E., Deprez, M., Duclos, G., Fine, D., Fischer, D. S., Ghazanfar, S., Gillich, A., Giotti,
1382 B., Gould, J., Guo, M., Gutierrez, A. J., Habermann, A. C., Harvey, T., He, P., Hou, X.,
1383 Hu, L., Hu, Y., Jaiswal, A., Ji, L., Jiang, P., Kapellos, T. S., Kuo, C. S., Larsson, L.,
1384 Leney-Greene, M. A., Lim, K., Litvinukova, M., Ludwig, L. S., Lukassen, S., Luo, W.,
1385 Maatz, H., Madissoon, E., Mamanova, L., Manakongtreeeep, K., Leroy, S., Mayr, C.
1386 H., Mbano, I. M., McAdams, A. M., Nabhan, A. N., Nyquist, S. K., Penland, L.,
1387 Poirion, O. B., Poli, S., Qi, C., Queen, R., Reichart, D., Rosas, I., Schupp, J. C., Shea,
1388 C. V., Shi, X., Sinha, R., Sit, R. V., Slowikowski, K., Slyper, M., Smith, N. P.,
1389 Sountoulidis, A., Strunz, M., Sullivan, T. B., Sun, D., Talavera-Lopez, C., Tan, P.,
1390 Tantivit, J., Travaglini, K. J., Tucker, N. R., Vernon, K. A., Wadsworth, M. H.,
1391 Waldman, J., Wang, X., Xu, K., Yan, W., Zhao, W., Ziegler, C. G. K., Consortium, N.
1392 L. & Human Cell Atlas Lung Biological, N. Single-cell meta-analysis of SARS-CoV-

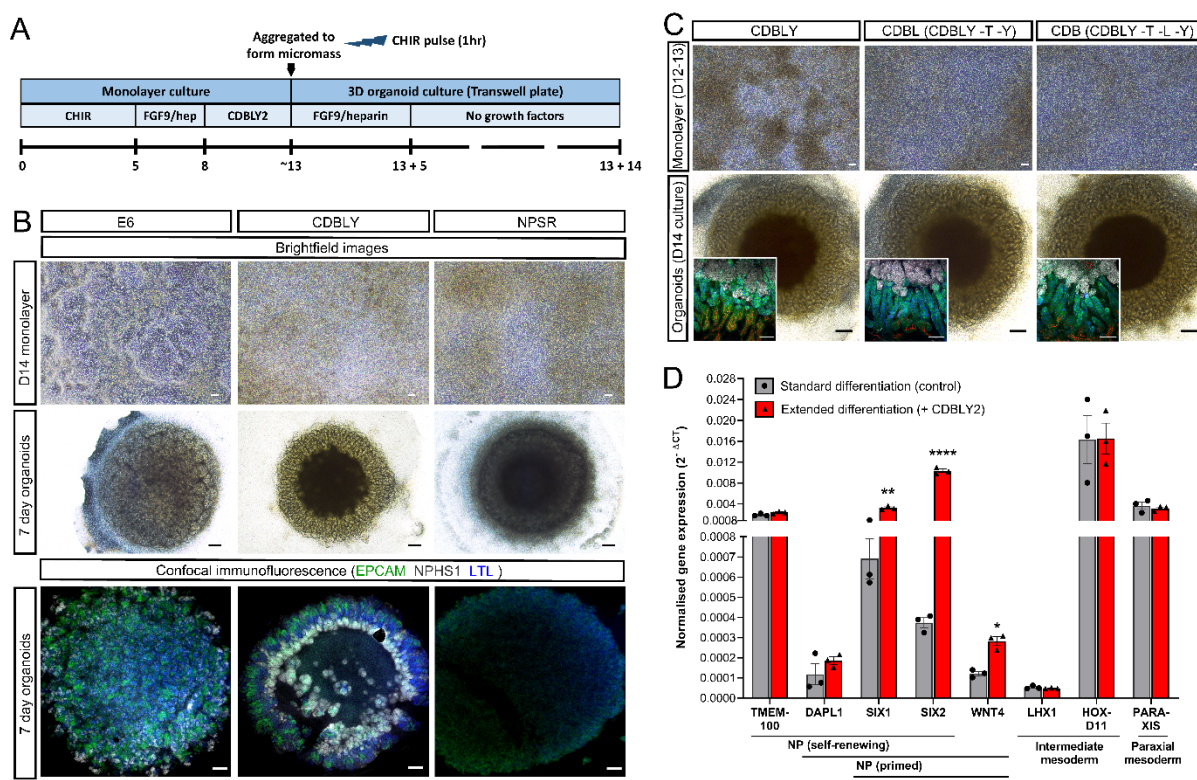
- 1393 2 entry genes across tissues and demographics. *Nat Med* **27**, 546-559,
1394 doi:10.1038/s41591-020-01227-z (2021).
- 1395 118 Kalejaiye, T. D., Bhattacharya, R., Burt, M. A., Travieso, T., Okafor, A. E., Mou, X.,
1396 Blasi, M. & Musah, S. SARS-CoV-2 Employ BSG/CD147 and ACE2 Receptors to
1397 Directly Infect Human Induced Pluripotent Stem Cell-Derived Kidney Podocytes.
1398 *Front Cell Dev Biol* **10**, 855340, doi:10.3389/fcell.2022.855340 (2022).
- 1399 119 Chung, E., Deacon, P. & Park, J. S. Notch is required for the formation of all nephron
1400 segments and primes nephron progenitors for differentiation. *Development* **144**, 4530-
1401 4539, doi:10.1242/dev.156661 (2017).
- 1402 120 Surendran, K., Boyle, S., Barak, H., Kim, M., Stomberski, C., McCright, B. & Kopan,
1403 R. The contribution of Notch1 to nephron segmentation in the developing kidney is
1404 revealed in a sensitized Notch2 background and can be augmented by reducing Mint
1405 dosage. *Dev Biol* **337**, 386-395, doi:10.1016/j.ydbio.2009.11.017 (2010).
- 1406 121 Karner, C. M., Das, A., Ma, Z., Self, M., Chen, C., Lum, L., Oliver, G. & Carroll, T. J.
1407 Canonical Wnt9b signaling balances progenitor cell expansion and differentiation
1408 during kidney development. *Development* **138**, 1247-1257, doi:10.1242/dev.057646
1409 (2011).
- 1410 122 Park, J. S., Valerius, M. T. & McMahon, A. P. Wnt/beta-catenin signaling regulates
1411 nephron induction during mouse kidney development. *Development* **134**, 2533-2539,
1412 doi:10.1242/dev.006155 (2007).
- 1413 123 Blank, U., Brown, A., Adams, D. C., Karolak, M. J. & Oxburgh, L. BMP7 promotes
1414 proliferation of nephron progenitor cells via a JNK-dependent mechanism.
1415 *Development* **136**, 3557-3566, doi:10.1242/dev.036335 (2009).
- 1416 124 Lindstrom, N. O., Carragher, N. O. & Hohenstein, P. The PI3K pathway balances self-
1417 renewal and differentiation of nephron progenitor cells through beta-catenin signaling.
1418 *Stem Cell Reports* **4**, 551-560, doi:10.1016/j.stemcr.2015.01.021 (2015).
- 1419 125 Muthukrishnan, S. D., Yang, X., Friesel, R. & Oxburgh, L. Concurrent BMP7 and
1420 FGF9 signalling governs AP-1 function to promote self-renewal of nephron progenitor
1421 cells. *Nature communications* **6**, 10027, doi:10.1038/ncomms10027 (2015).

- 1422 126 Tanigawa, S., Naganuma, H., Kaku, Y., Era, T., Sakuma, T., Yamamoto, T., Taguchi, A. & Nishinakamura, R. Activin Is Superior to BMP7 for Efficient Maintenance of Human iPSC-Derived Nephron Progenitors. *Stem Cell Reports* **13**, 322-337, doi:10.1016/j.stemcr.2019.07.003 (2019).
- 1426 127 Matsuda, M., Hayashi, H., Garcia-Ojalvo, J., Yoshioka-Kobayashi, K., Kageyama, R., Yamanaka, Y., Ikeya, M., Toguchida, J., Alev, C. & Ebisuya, M. Species-specific segmentation clock periods are due to differential biochemical reaction speeds. *Science* **369**, 1450-1455, doi:10.1126/science.aba7668 (2020).
- 1430 128 Lancaster, M. A., Renner, M., Martin, C. A., Wenzel, D., Bicknell, L. S., Hurles, M. E., Homfray, T., Penninger, J. M., Jackson, A. P. & Knoblich, J. A. Cerebral organoids model human brain development and microcephaly. *Nature* **501**, 373-379, doi:10.1038/nature12517 (2013).
- 1434 129 Velasco, S., Kedaigle, A. J., Simmons, S. K., Nash, A., Rocha, M., Quadrato, G., Paulsen, B., Nguyen, L., Adiconis, X., Regev, A., Levin, J. Z. & Arlotta, P. Individual brain organoids reproducibly form cell diversity of the human cerebral cortex. *Nature* **570**, 523-527, doi:10.1038/s41586-019-1289-x (2019).
- 1438 130 Taguchi, A., Kaku, Y., Ohmori, T., Sharmin, S., Ogawa, M., Sasaki, H. & Nishinakamura, R. Redefining the in vivo origin of metanephric nephron progenitors enables generation of complex kidney structures from pluripotent stem cells. *Cell Stem Cell* **14**, 53-67, doi:10.1016/j.stem.2013.11.010 (2014).
- 1442 131 Bantounas, I., Silajdzic, E., Woolf, A. S. & Kimber, S. J. Formation of Mature Nephrons by Implantation of Human Pluripotent Stem Cell-Derived Progenitors into Mice. *Methods in molecular biology* **2067**, 309-322, doi:10.1007/978-1-4939-9841-8_19 (2020).
- 1446 132 Nam, S. A., Seo, E., Kim, J. W., Kim, H. W., Kim, H. L., Kim, K., Kim, T. M., Ju, J. H., Gomez, I. G., Uchimura, K., Humphreys, B. D., Yang, C. W., Lee, J. Y., Kim, J., Cho, D. W., Freedman, B. S. & Kim, Y. K. Graft immaturity and safety concerns in transplanted human kidney organoids. *Exp Mol Med* **51**, 1-13, doi:10.1038/s12276-019-0336-x (2019).
- 1451 133 van den Berg, C. W., Ritsma, L., Avramut, M. C., Wiersma, L. E., van den Berg, B. M., Leuning, D. G., Lievers, E., Koning, M., Vanslambrouck, J. M., Koster, A. J.,

- 1453 Howden, S. E., Takasato, M., Little, M. H. & Rabelink, T. J. Renal Subcapsular
1454 Transplantation of PSC-Derived Kidney Organoids Induces Neo-vasculogenesis and
1455 Significant Glomerular and Tubular Maturation In Vivo. *Stem Cell Reports* **10**, 751-
1456 765, doi:10.1016/j.stemcr.2018.01.041 (2018).
- 1457 134 Briggs, J. A., Sun, J., Shepherd, J., Ovchinnikov, D. A., Chung, T. L., Nayler, S. P.,
1458 Kao, L. P., Morrow, C. A., Thakar, N. Y., Soo, S. Y., Peura, T., Grimmond, S. &
1459 Wolvetang, E. J. Integration-free induced pluripotent stem cells model genetic and
1460 neural developmental features of down syndrome etiology. *Stem Cells* **31**, 467-478,
1461 doi:10.1002/stem.1297 (2013).
- 1462 135 Vlahos, K., Sourris, K., Mayberry, R., McDonald, P., Bruveris, F. F., Schiesser, J. V.,
1463 Bozaoglu, K., Lockhart, P. J., Stanley, E. G. & Elefanty, A. G. Generation of iPSC lines
1464 from peripheral blood mononuclear cells from 5 healthy adults. *Stem Cell Res* **34**,
1465 101380, doi:10.1016/j.scr.2018.101380 (2019).
- 1466 136 Chen, G., Gulbranson, D. R., Hou, Z., Bolin, J. M., Ruotti, V., Probasco, M. D., Smuga-
1467 Otto, K., Howden, S. E., Diol, N. R., Propson, N. E., Wagner, R., Lee, G. O.,
1468 Antosiewicz-Bourget, J., Teng, J. M. & Thomson, J. A. Chemically defined conditions
1469 for human iPSC derivation and culture. *Nat Methods* **8**, 424-429,
1470 doi:10.1038/nmeth.1593 (2011).
- 1471 137 Schindelin, J., Arganda-Carreras, I., Frise, E., Kaynig, V., Longair, M., Pietzsch, T.,
1472 Preibisch, S., Rueden, C., Saalfeld, S., Schmid, B., Tinevez, J. Y., White, D. J.,
1473 Hartenstein, V., Eliceiri, K., Tomancak, P. & Cardona, A. Fiji: an open-source platform
1474 for biological-image analysis. *Nat Methods* **9**, 676-682, doi:10.1038/nmeth.2019
1475 (2012).
- 1476 138 Stoeckius, M., Zheng, S., Houck-Loomis, B., Hao, S., Yeung, B. Z., Mauck, W. M.,
1477 3rd, Smibert, P. & Satija, R. Cell Hashing with barcoded antibodies enables
1478 multiplexing and doublet detection for single cell genomics. *Genome Biol* **19**, 224,
1479 doi:10.1186/s13059-018-1603-1 (2018).
- 1480 139 Ransick, A., Lindstrom, N. O., Liu, J., Zhu, Q., Guo, J. J., Alvarado, G. F., Kim, A. D.,
1481 Black, H. G., Kim, J. & McMahon, A. P. Single-Cell Profiling Reveals Sex, Lineage,
1482 and Regional Diversity in the Mouse Kidney. *Developmental cell* **51**, 399-413 e397,
1483 doi:10.1016/j.devcel.2019.10.005 (2019).

- 1484 140 Hafemeister, C. & Satija, R. Normalization and variance stabilization of single-cell
1485 RNA-seq data using regularized negative binomial regression. *Genome Biol* **20**, 296,
1486 doi:10.1186/s13059-019-1874-1 (2019).
- 1487 141 Butler, A., Hoffman, P., Smibert, P., Papalexi, E. & Satija, R. Integrating single-cell
1488 transcriptomic data across different conditions, technologies, and species. *Nature
1489 biotechnology* **36**, 411-420, doi:10.1038/nbt.4096 (2018).
- 1490 142 Stuart, T., Butler, A., Hoffman, P., Hafemeister, C., Papalexi, E., Mauck, W. M., 3rd,
1491 Hao, Y., Stoeckius, M., Smibert, P. & Satija, R. Comprehensive Integration of Single-
1492 Cell Data. *Cell* **177**, 1888-1902 e1821, doi:10.1016/j.cell.2019.05.031 (2019).
- 1493 143 Harris, C. R., Millman, K. J., van der Walt, S. J., Gommers, R., Virtanen, P.,
1494 Cournapeau, D., Wieser, E., Taylor, J., Berg, S., Smith, N. J., Kern, R., Picus, M.,
1495 Hoyer, S., van Kerkwijk, M. H., Brett, M., Haldane, A., Del Rio, J. F., Wiebe, M.,
1496 Peterson, P., Gerard-Marchant, P., Sheppard, K., Reddy, T., Weckesser, W., Abbasi,
1497 H., Gohlke, C. & Oliphant, T. E. Array programming with NumPy. *Nature* **585**, 357-
1498 362, doi:10.1038/s41586-020-2649-2 (2020).
- 1499 144 van der Walt, S., Schonberger, J. L., Nunez-Iglesias, J., Boulogne, F., Warner, J. D.,
1500 Yager, N., Gouillart, E., Yu, T. & scikit-image, c. scikit-image: image processing in
1501 Python. *PeerJ* **2**, e453, doi:10.7717/peerj.453 (2014).
- 1502 145 Virtanen, P., Gommers, R., Oliphant, T. E., Haberland, M., Reddy, T., Cournapeau, D.,
1503 Burovski, E., Peterson, P., Weckesser, W., Bright, J., van der Walt, S. J., Brett, M.,
1504 Wilson, J., Millman, K. J., Mayorov, N., Nelson, A. R. J., Jones, E., Kern, R., Larson,
1505 E., Carey, C. J., Polat, I., Feng, Y., Moore, E. W., VanderPlas, J., Laxalde, D., Perktold,
1506 J., Cimrman, R., Henriksen, I., Quintero, E. A., Harris, C. R., Archibald, A. M., Ribeiro,
1507 A. H., Pedregosa, F., van Mulbregt, P. & SciPy, C. SciPy 1.0: fundamental algorithms
1508 for scientific computing in Python. *Nat Methods* **17**, 261-272, doi:10.1038/s41592-019-
1509 0686-2 (2020).
- 1510
- 1511

1512 **Figures and legends**



1513

1514 **Figure 1: Extended monolayer culture in CDBLY supports nephron progenitors and**
1515 **preserves nephrogenic capacity.** A. Schematic depicting the extended differentiation protocol

1516 in CDBLY2. B. Brightfield and confocal immunofluorescence images of extended monolayer

1517 differentiations in E6, CDBLY and NPSR, and resulting organoids. Immunofluorescence

1518 depicts nephrons (EPCAM; green), podocytes of glomeruli (NPHS1; grey), and proximal

1519 tubules (LTL; blue). Scale bars represent 100μm (monolayers) and 200μm (organoids). C.

1520 Brightfield images of extended monolayer differentiations using CDBLY variations and

1521 resulting organoids, with inset confocal immunofluorescence images highlighting organoid

1522 nephron alignment and patterning. Immunofluorescence depicts nephrons (EPCAM; green),

1523 podocytes of glomeruli (NPHS1; grey), proximal tubules (HNF4A; blue), and Loop of Henle

1524 (SLC12A1; red). Scale bars represent 100μm (monolayer brightfields and organoid

1525 immunofluorescence) and 200μm (organoid brightfields). D. qRT-PCR analysis of standard

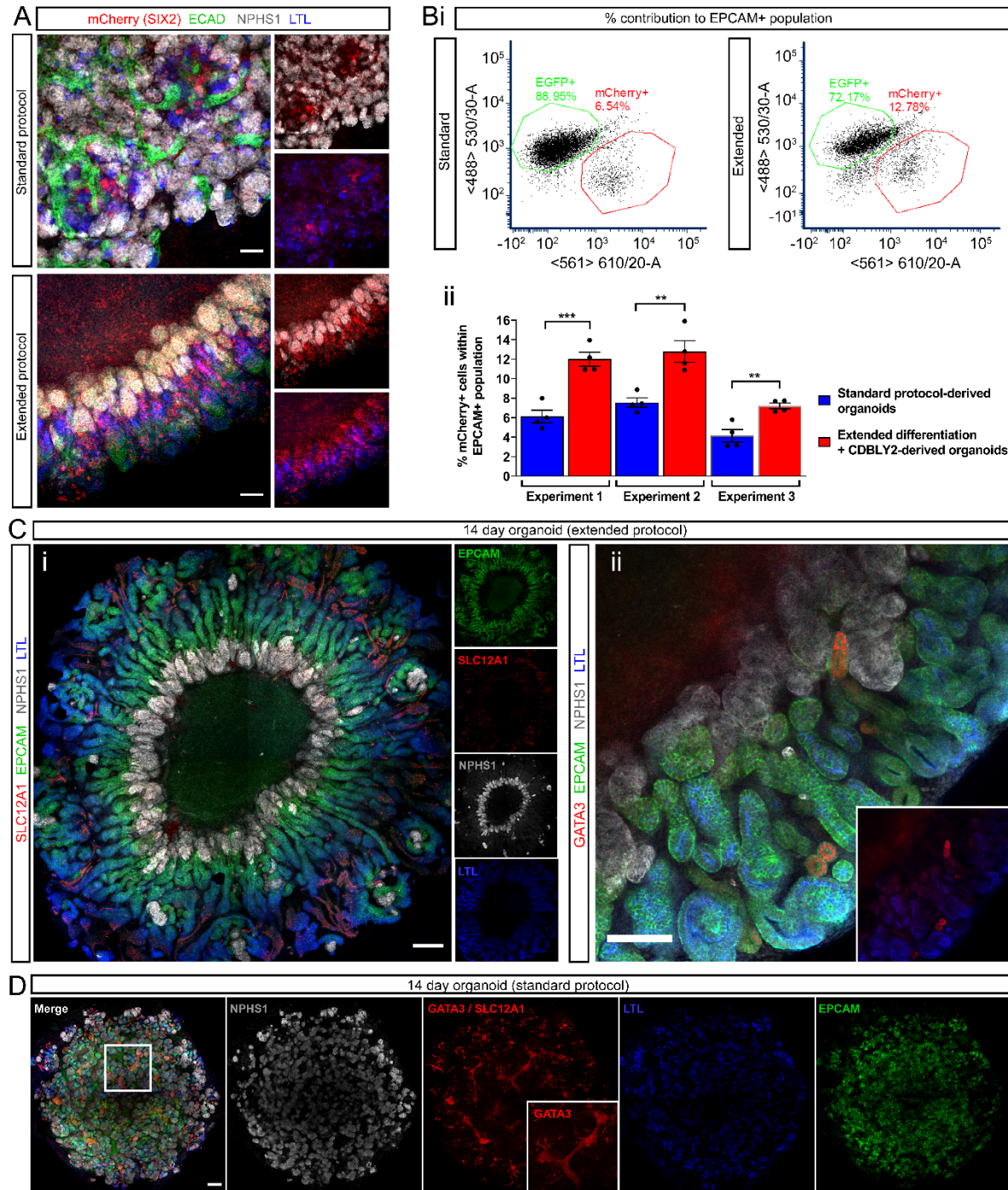
1526 and extended monolayer differentiations. Error bars represent SEM from n = 3 biological

1527 replicates. Statistical significance was determined using an unpaired t test. Asterisks represent

1528 P values adjusted for multiple comparisons using the Holm-Sidak method, alpha = 0.05 (*; P

1529 ≤ 0.05, **; P ≤ 0.01, ***; P ≤ 0.001, ****; P ≤ 0.0001).

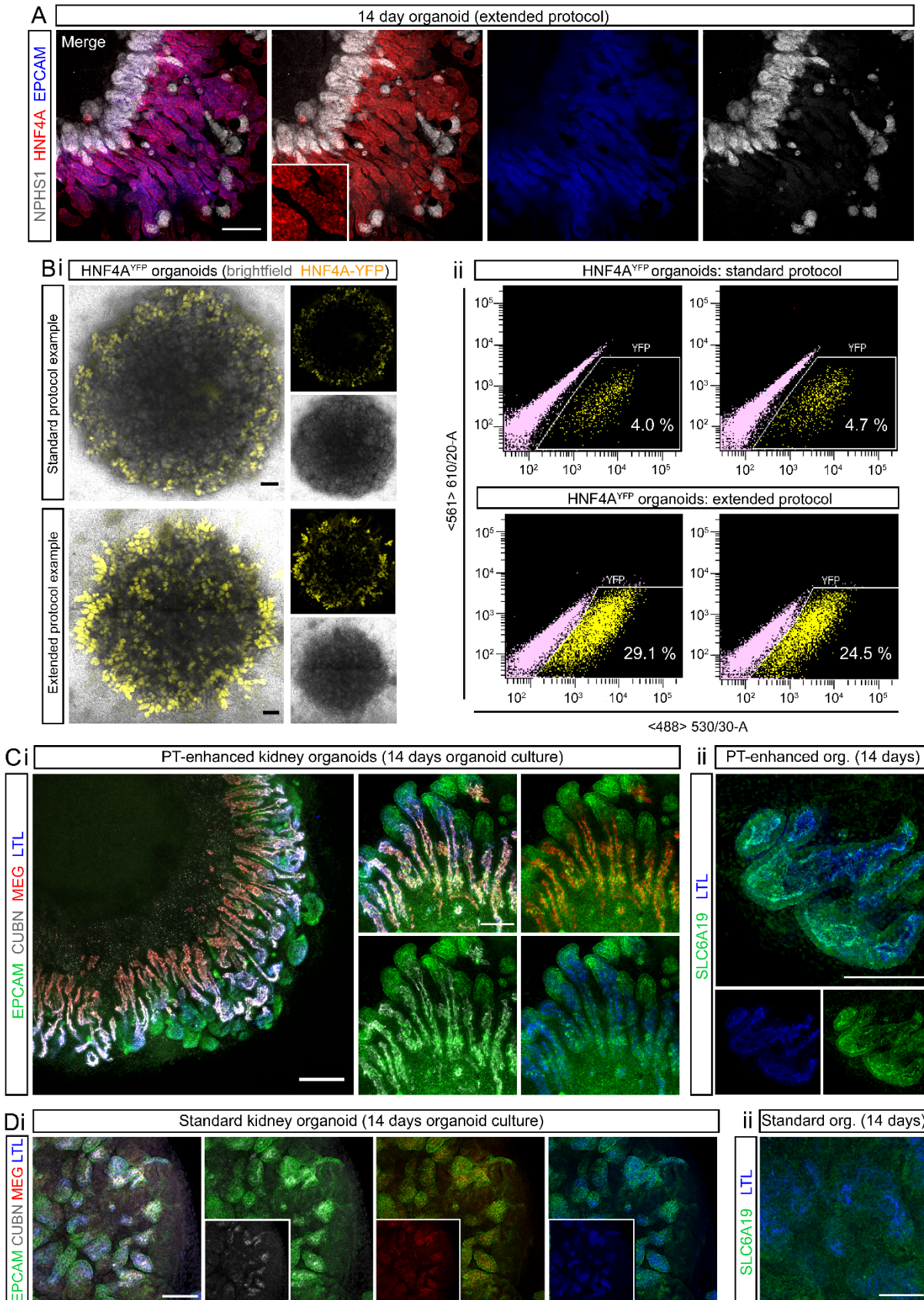
1530



1531
 1532 **Figure 2: Extended monolayer culture in CDBLY2 increases SIX2+ progenitor**
 1533 **contribution to nephrons and proximalisation. A.** Confocal immunofluorescence of D7+14
 1534 (standard protocol) and D13+14 (extended protocol) organoids derived from the
 1535 SIX2^{Cre/Cre}:GAPDH^{dual} lineage tracing iPSC line. Images depict merged and separated channels
 1536 showing lineage-traced SIX2+ cells (mCherry; red), distal tubules (ECAD; green), podocytes
 1537 (NPHS1; grey) and proximal tubules (LTL; blue). Scale bars represent 100 µm. **B.** Flow
 1538 cytometry of SIX2^{Cre/Cre}:GAPDH^{dual} lineage tracing organoids derived from extended (13 day

1539 + CDBLY2) and standard (7 day + E6 media) differentiations depicting mCherry contribution
1540 to the EPCAM+ (nephron) population. Flow plots shown in **(i)** are representative of the
1541 replicates across multiple experiments. Percentage mCherry contributions from flow cytometry
1542 are depicted in bar graph **(ii)**. Error bars in **(ii)** represent SEM from n = 4 biological replicates
1543 across 3 independent experiments. Statistical significance was determined using an unpaired t
1544 test. Asterisks represent P values adjusted for multiple comparisons using the Holm-Sidak
1545 method, alpha = 0.05 (*; P ≤ 0.05, **; P ≤ 0.01, ***; P ≤ 0.001, ****; P ≤ 0.0001). **C.** Confocal
1546 immunofluorescence of D13+14 organoids demonstrating **(i)** aligned nephron morphology
1547 with nephron segmentation makers (nephron epithelium [EPCAM; green], distal tubule/Loop
1548 of Henle [SLC12A1; red], proximal tubules [LTL; blue], and podocytes [NPHS1; grey]) and
1549 **(ii)** the presence of few GATA3+ connecting segment/ureteric epithelium structures (red), co-
1550 stained for nephron epithelium (EPCAM; green), podocytes (NPHS1; grey), and proximal
1551 tubules (LTL; blue). Inset in **(ii)** shows GATA3 and LTL alone. Scale bars in **(i)** and **(ii)**
1552 represent 200 μm and 100 μm, respectively. **C.** Confocal immunofluorescence of a D7+14
1553 (standard) organoid depicting homogenous distribution of podocytes (NPHS1; grey), proximal
1554 tubules (LTL; red), and nephron epithelium (EPCAM; green), as well as the presence of
1555 extended segments of centralised GATA3+ connecting segment/ureteric epithelium (also
1556 highlighted in insets). Scale bar represents 200 μm.

1557

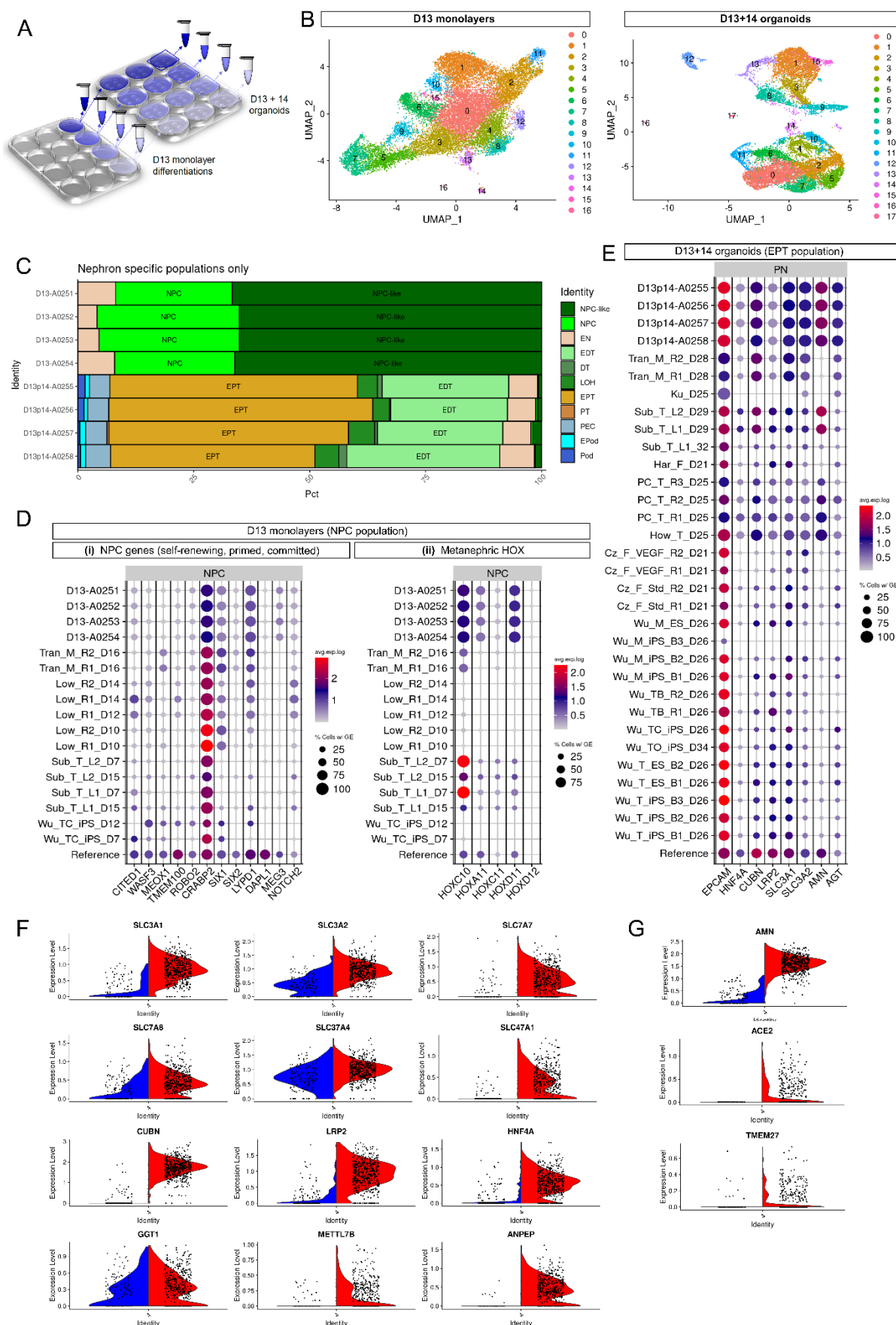


1559 **Figure 3: Enhanced organoids express mature and appropriately localised PT**
1560 **transporter proteins and transcription factors. A.** Confocal immunofluorescence of

1561 HNF4A protein expression (red) in EPCAM-positive PTs (blue) of a day 14 organoid derived
1562 from extended differentiation of iPSCs in CDBLY2. NPHS1 (grey) marks podocytes of the
1563 glomeruli. Inset depicts higher magnification of HNF4A-expressing PT segments emphasising
1564 nuclear localisation. Scale bar represents 100 μm . **Bi.** Live confocal microscopy of 2
1565 representative standard and extended protocol-derived organoids (also shown in [Bii])
1566 generated using the HNF4A^{YFP} fluorescent iPSC reporter line (PCS-201-010/HNF4A^{YFP}). YFP
1567 (yellow) marks proximal tubules. Transmitted light channel (brightfield) is shown as merged
1568 and separate images. Scale bars represent 200 μm . **Bii.** Flow cytometry plots of the 2
1569 representative HNF4A^{YFP} organoids from experiment depicted in (Bi), derived from standard
1570 and extended protocols. **C-D.** Confocal immunofluorescence of PT-enhanced (C) and standard
1571 (D) (D13+14) organoids showing PT markers within EPCAM+ (green) nephrons, including
1572 LTL (blue; [i] and [ii]), CUBILIN (CUBN; grey [i]), MEGALIN (MEG; red [i]), and SLC6A19
1573 (green [ii]). Scale bars represent 200 μm (**Ci**) and 100 μm (**Di-ii** and **Cii**).

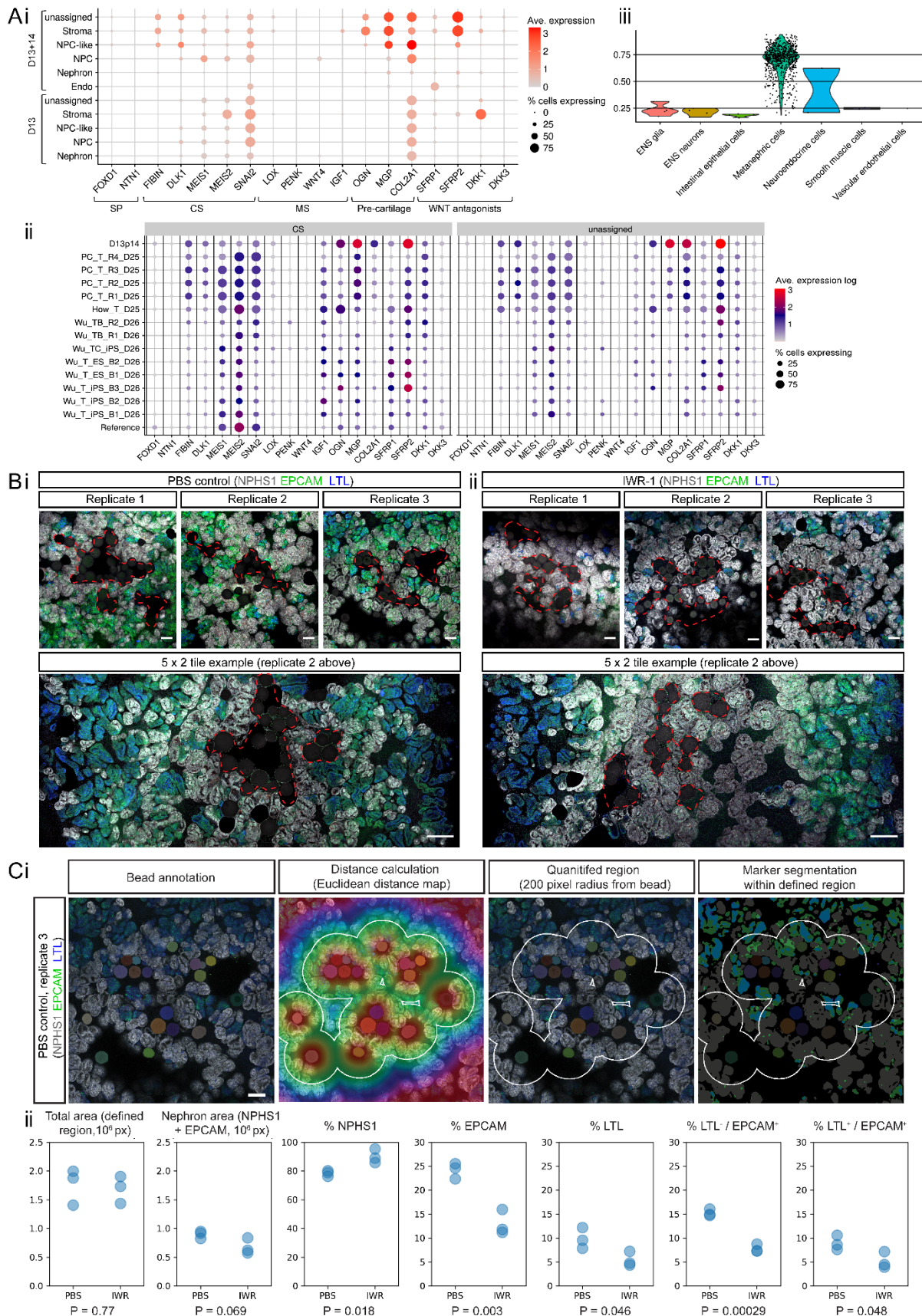
1574

1575

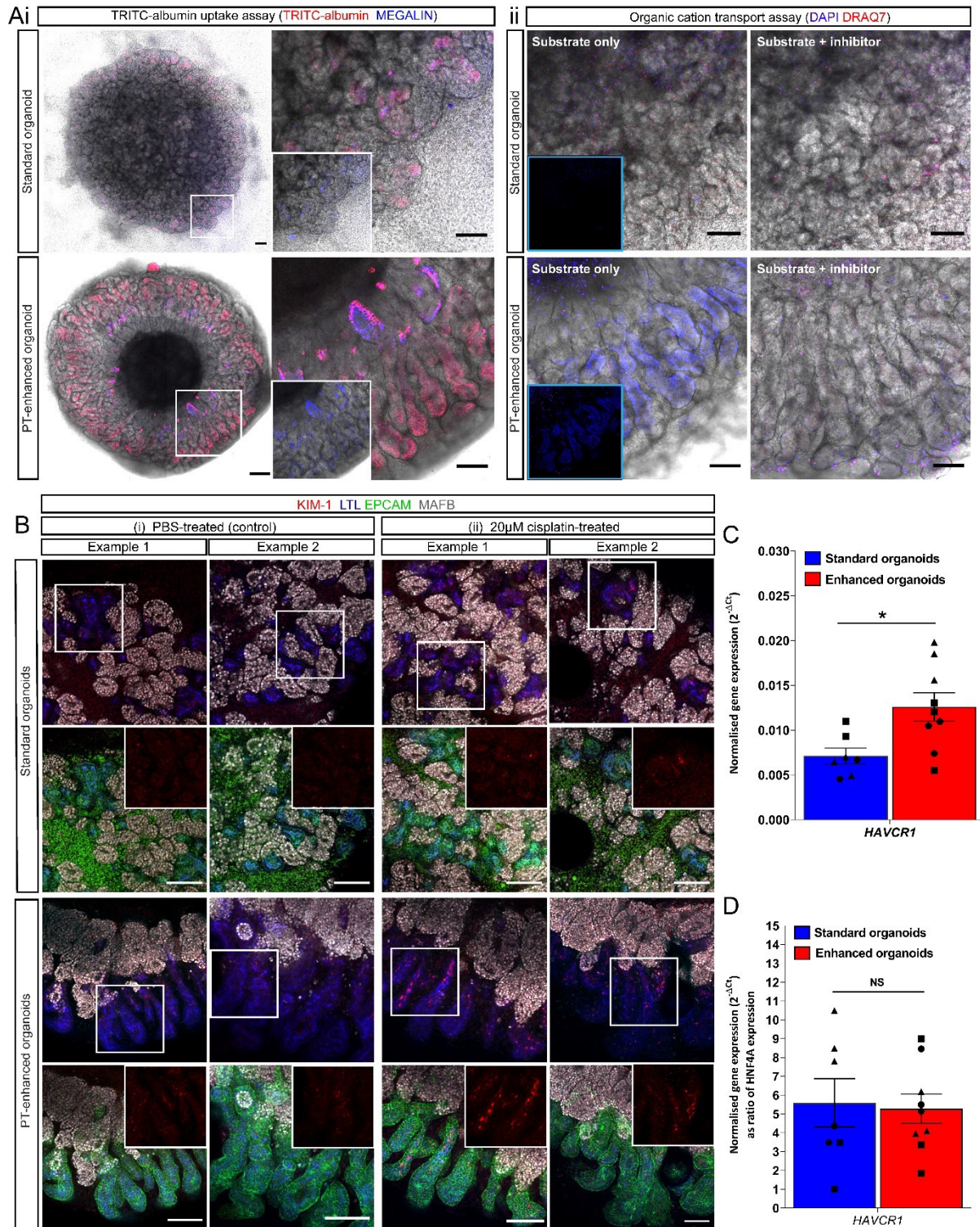


1577 **Figure 4: Single cell transcriptional profiling (scRNAseq) shows improved specification,**
1578 **patterning and maturation of proximal tubules and their progenitors.** **A.** Schematic
1579 depicting experimental design and profiled samples. Multiple organoids (2.5×10^5 cells per
1580 organoid) were generated from each of the 4 replicate differentiated cell monolayers at D13.
1581 The remaining portion of cells from each replicate monolayer were barcoded and pooled for
1582 generation of the D13 monolayer library. The resulting organoids were cultured for 14 days
1583 before being harvested and pooled within replicate wells, making 4 cell suspensions. These 4
1584 suspensions were individually barcoded and pooled into a single cell suspension for generation
1585 of the D13+14 organoid library. **B.** UMAP plots of D13 and D13+14 samples (pooled
1586 replicates) identifying 16 and 17 distinct cell clusters, respectively. **C.** *ComparePlots* depicting
1587 proportions of kidney cell types (nephron-specific populations only) in D13 and D13+14
1588 sample replicates as classified by *DevKidCC*. Population abbreviations: nephron progenitor
1589 cell (NPC), early nephron (EN), early distal tubule (EDT), DT (distal tubule), loop of Henle
1590 (LOH), early proximal tubule (EPT), proximal tubule (PT), parietal epithelial cell (PEC), early
1591 podocyte (EPod), podocyte (Pod). **D.** *DevKidCC* dot plots comparing the expression of gene
1592 signatures for **(i)** self-renewing (*SIX1*, *SIX2*, *CITED1*, *WASF3*, *DAPL1*, *MEOXI*, *TMEM100*,
1593 *ROBO2*, *CRABP2*), committed (*SIX1*, *SIX2*, *LYPDI*), and primed (*DAPL1*, *NOTCH2*, *MEG3*)
1594 NPC subsets, as well as **(ii)** metanephric HOX genes, within the D13 monolayer NPC
1595 population to that of published stem cell-derived kidney datasets and a mixed (week 11 – 18)
1596 human fetal kidney reference dataset (Hochane, *et al.*, 2019; Tran, *et al.*, 2019; Hollywood, *et*
1597 *al.*, 2020). Comparisons were made to published monolayer and early nephrogenic datasets
1598 (Subramanian, *et al.*, 2019; Wu, *et al.*, 2018; Low, *et al.*, 2019; Tran, *et al.*, 2019) as outlined
1599 previously (Wilson, *et al.*, 2021). **E.** *DevKidCC* dot plot comparing the expression of proximal
1600 nephron (PN) gene signatures within the EPT population of D13+14 organoids to that of
1601 published stem cell-derived kidney organoid datasets (Czerniecki, *et al.*, 2018; Harder, *et al.*,
1602 2019; Kumar, *et al.*, 2019) and the mixed week 11 - 18 fetal kidney reference dataset (Hochane,
1603 *et al.*, 2019; Tran, *et al.*, 2019; Hollywood, *et al.*, 2020) as outlined previously (Wilson, *et al.*,
1604 2021). **F-G.** Violin plots in **(F)** and **(G)** compare PT-specific gene expression of PT-enhanced
1605 organoids (red, right) with our existing standard organoid dataset of equivalent line and age
1606 (blue, left) (Howden, *et al.*, 2019). Genes encoding auxiliary proteins are shown in **(G)**.

1607



1609 **Figure 5. WNT signalling gradient influences nephron alignment and directionality. A.**
1610 Analyses of scRNASeq datasets for D13+14 PT-enhanced organoid replicates (**i - iii**) and D13
1611 monolayer replicates (**i** and **iii**) as classified by *DevKidCC*. Dot plot in (**i**) depicts expression
1612 of stroma compartment markers (England, *et al.*, 2020) and WNT antagonists in D13+14 and
1613 D13 samples. *DevKidCC*'s DotPlotCompare in (**ii**) shows the comparison of D13+14 to other
1614 relevant published datasets (cortical stroma [CS] and unassigned populations only). Dot colour
1615 and size in (**i - ii**) represents unscaled gene expression and percentage of cells expressing each
1616 gene, respectively. Violin plot (**iii**) depicts the similarity scores for all unassigned cells within
1617 D13 monolayer replicates as predicted by the Azimuth label transfer method
1618 (<https://azimuth.hubmapconsortium.org/>) with the human developmental reference dataset
1619 (Cao, *et al.*, 2020), where cells are grouped by population with the highest similarity score.
1620 Population abbreviations in (**i - iii**): nephron progenitor cell (NPC), endothelium (Endo),
1621 stroma progenitor (SP), cortical stroma (CS), medullary stroma (MS), enteric nervous system
1622 (ENS). **B.** Confocal immunofluorescence images of replicate standard organoids bioprinted in
1623 a patch conformation and in contact with either agarose beads soaked in PBS (control; **Bi**) or
1624 in 10 μ M IWR-1 (**Bii**). Clusters of beads are outlined with red dashed lines. Organoids are
1625 stained with markers of epithelium (EPCAM; green), proximal tubule (LTL; blue), and
1626 podocytes of the glomeruli (NPHS1; grey). Scale bars represent 100 μ m (all top panels) and
1627 200 μ m (bottom tile panels). **Ci.** Example image from (**Bi**) (PBS control, replicate 3)
1628 illustrating the image annotation approach used to segment and quantify the proportion of
1629 nephron structures (NPHS1+ [grey], EPCAM+ [green], and LTL+ [blue]) within a defined
1630 region 200 pixels from any bead (white outline). Solid colours represent masks for beads and
1631 nephrons. Scale bar represents 200 μ m. **Cii.** Quantification of PBS control and IWR-1 treated
1632 organoid images from (**Bi-ii**) using approach illustrated in (**Ci**), with n = 3 replicates per
1633 condition. Total area and nephron area values are shown in pixels (10^6 px). Percentage (%) of
1634 each structure (NPHS1+, EPCAM+, LTL+) are shown as a proportion of the total nephron
1635 area. P values are indicated below each plot.

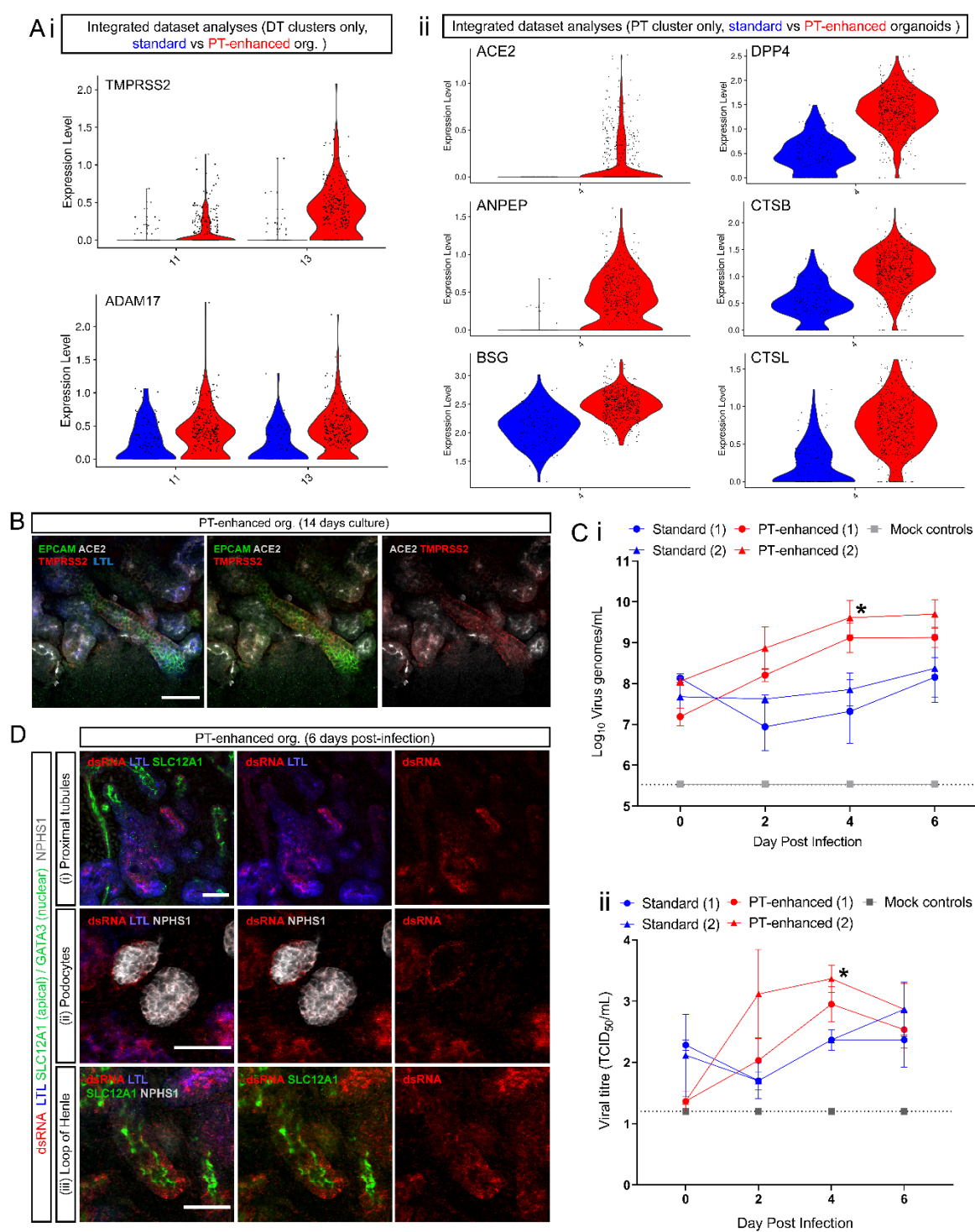


1637 **Figure 6: Enhanced organoids possess functional PT transporters and appropriate injury**
 1638 **response. A.** Live confocal images of standard and PT-enhanced organoids (transmitted light
 1639 and fluorescence overlays) depicting uptake of (i) TRITC-albumin (red) into MEGALIN-
 1640 positive PTs (blue) and (ii) uptake of DAPI (blue; surrogate for organic cation transport
 1641 capacity). White boxed areas on left images of (i) are shown as higher magnification on right

1642 (insets depict MEGALIN staining alone). Organic cation uptake image set **(ii)** depicts
1643 organoids exposed to substrate alone (DAPI; blue, left images) or a combination of
1644 substrate/DAPI + inhibitor/Cimetidine (right images). Dead cells in both panels of **(ii)** are
1645 labelled with DRAQ7 (red). Insets in **(ii)** depict blue channel only without brightfield overlay.
1646 Scale bars represent 200 μm (whole organoid images in **[i]**) and 100 μm (left images in **[i]**, all
1647 images in **[ii]**). **B.** Confocal immunofluorescence of representative D7+14 (standard; top
1648 panels) and D13+14 (PT-enhanced; bottom panels) line-matched organoids following 24 hours
1649 treatment with E6 media containing either **(ii)** 20 μM cisplatin or **(i)** an equivalent volume of
1650 PBS. Images depict KIM-1-expressing cells (red) in LTL+ proximal tubules (blue) with
1651 nephron epithelium co-stained with EPCAM (green). Insets of bottom row images for standard
1652 and PT-enhanced organoids show KIM-1 staining (red channel) alone from white boxed
1653 regions in top row images. Scale bars in all images represent 100 μm . **C-D.** qRT-PCR analyses
1654 depicting KIM-1 gene (*HAVCR1*) expression in standard (blue) and PT-enhanced (red)
1655 organoids from experiments shown in **(B)**. *HAVCR1* gene expression values are normalised to
1656 the expression of housekeeping gene *GAPDH* and depicted both with **(D)** and without **(C)**
1657 compensation for differences in proximal tubule proportion (expressed as a ratio of *HNF4A*).
1658 Error bars represent SEM from n = 8 (control) and n = 9 (cisplatin-treated) biological replicates
1659 across 3 replicate experiments as indicated. Statistical significance was determined using an
1660 unpaired t test. Asterisk represents P value (*; P \leq 0.05) adjusted for multiple comparisons
1661 using the Holm-Sidak method alpha = 0.05. NS = non-significant.

1662

1663



1664

1665

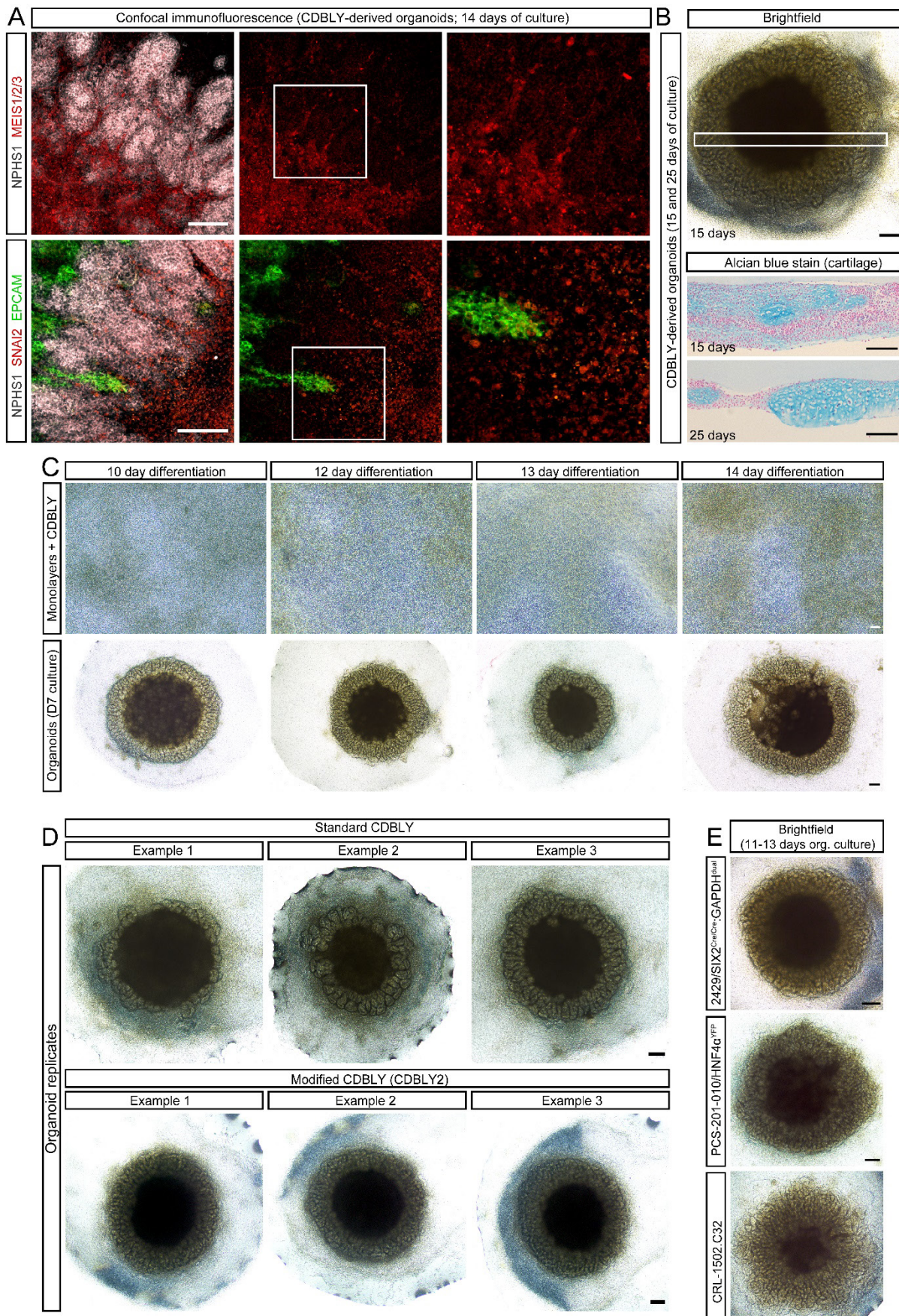
1666 **Figure 7: PT-enhanced organoids show improved SARS-CoV-2 entry factor expression,**
 1667 **infectivity, and viral replication. A.** scRNASeq analyses comparing the expression of SARS-
 1668 CoV-2 entry factors in PT-enhanced organoids (red) and our existing standard organoid dataset
 1669 (line- and age-matched) (Howden, *et al.*, 2019). Violin plots compare expression of genes
 1670 within integrated datasets from which (i) distal tubule (DT) and (ii) proximal tubule (PT)
 1671 clusters have been isolated. **B.** Confocal immunofluorescence of ACE2 (green) and TMPRSS2

1672 (red) demonstrating protein localisation in PT-enhanced kidney organoids. Nephron epithelium
1673 is stained with EPCAM (green). ACE2 and TMPRSS2 entry factors are depicted in grey and
1674 red, respectively. Scale bars represent 50 μ m. **Ci.** qRT-PCR for SARS-CoV-2 viral envelope
1675 (*E*) gene (genome copies per mL) in the same culture media samples as depicted in **(Cii)** below.
1676 Organoids from the two representative experiments are indicated (1, 2) for standard (blue), PT-
1677 enhanced (red), and mock-infected (grey line; representative of all mock results across the same
1678 4 independent experiments). Error bars represent SEM from n = 3 individual wells of organoids
1679 (3 organoids per well). Statistical significance was determined using a one-way ANOVA with
1680 Tukey's multiple comparisons test. Asterisk represents P value (*; P \leq 0.05). **Cii.** Viral titre
1681 determined by Vero cell assays (Median Tissue Culture Infectious Dose; TCID₅₀) of culture
1682 media sampled from SARS-CoV-2 infected standard and PT-enhanced organoids (blue and red
1683 lines, respectively), as well as mock-infected organoids (grey line; representative of all mock
1684 results across the same 4 independent experiments). Dotted line represents lower limit of
1685 detection (LOD). For both standard and PT-enhanced conditions, 2 representative independent
1686 experiments, replicated using the same iPSC line and culture conditions, are indicated as (1)
1687 and (2), with error bars representing SEM from n = 3 individual wells of organoids (3 organoids
1688 per well). Statistical significance was determined using a one-way ANOVA with Tukey's
1689 multiple comparisons test. Asterisk represents P value (*; P \leq 0.05). **D.** Confocal
1690 immunofluorescence of PT-enhanced organoids 6 days post-infection indicating viral dsRNA
1691 (red) localisation, co-stained for PTs (LTL; blue), Loop of Henle (SLC12A1; apical green),
1692 and podocytes (NPHS1; grey). Scale bars represent 50 μ m.

1693

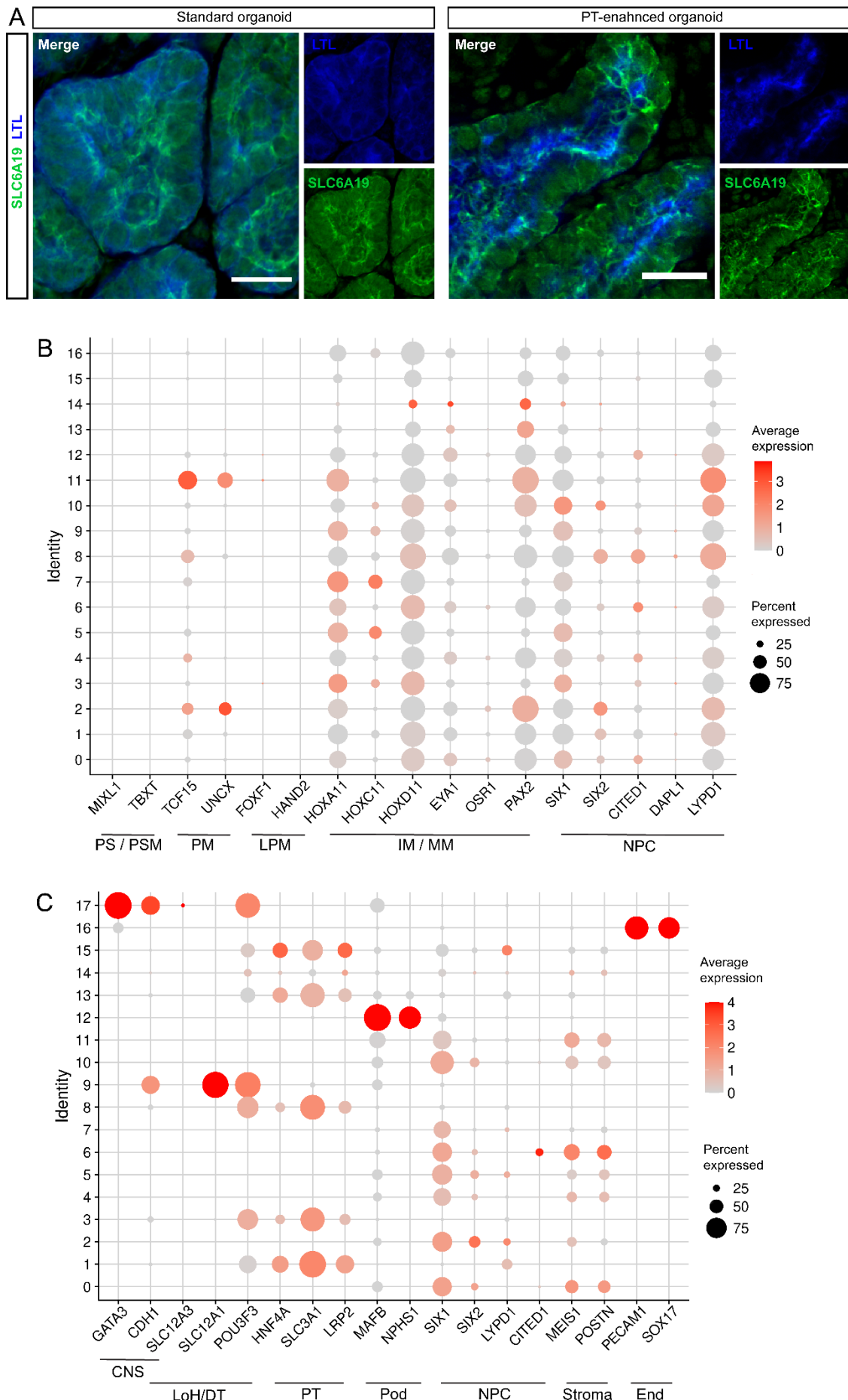
1694

1695 **Supplementary Figures and legends**



1697 **Supplementary Figure 1: Analyses of central core region and morphology of organoids**
1698 **resulting from extended monolayer differentiation in multiple cell lines.** **A.** Confocal
1699 immunofluorescence of stromal markers, MEIS1/2/3 (red; top panels) and SNAI2 (red; bottom
1700 panels) in central core region of organoids derived from CDBLY-exposed extended monolayer
1701 differentiations. Organoids are co-stained for podocytes (NPHS1; grey) and epithelium
1702 (EPCAM; green). Scale bars represent 100 μm . **B.** Representative brightfield image (top) of a
1703 day 13+15 organoid exposed to CDBLY at monolayer differentiation day 8. White box
1704 indicates approximate regions of cross sections shown in bottom panels stained with Alcian
1705 blue, indicating patchy cartilage formation in central core region (blue). Scale bars represent
1706 200 μm . **C.** Brightfield images of CDBLY-exposed monolayer differentiations extended for
1707 10, 12, 13, and 14 days and their resulting organoids. Scale bars represent 100 μm (monolayers)
1708 and 200 μm (organoids). **D.** Brightfield images showing 3 examples of representative organoid
1709 morphologies derived from CDBLY- (5 ng/mL BMP7) and CDBLY2-exposed (10 ng/mL
1710 BMP7) monolayer differentiations. Scale bars represent 200 μm . **E.** Brightfield images of
1711 D13+11 – D13+13 organoids generated from multiple iPSC lines using extended monolayer
1712 differentiation with 5 days x 6 μM CHIR exposure (CRL1502.C32; parental iPSC line derived
1713 from fetal female skin fibroblasts (Briggs, *et al.*, 2013), CRL-2429/SIX2^{Cre/Cre}:GAPDH^{dual};
1714 lineage tracing reporter iPSC line originally derived from neonatal male foreskin fibroblasts
1715 (Howden, *et al.*, 2019; Vanslambrouck, *et al.*, 2019), and PCS-201-010/HNF4 α ^{YFP}; PT-specific
1716 fluorescence reporter iPSC line originally derived from neonatal male skin fibroblasts
1717 (Vanslambrouck, *et al.*, 2019). Scale bars represent 200 μm .

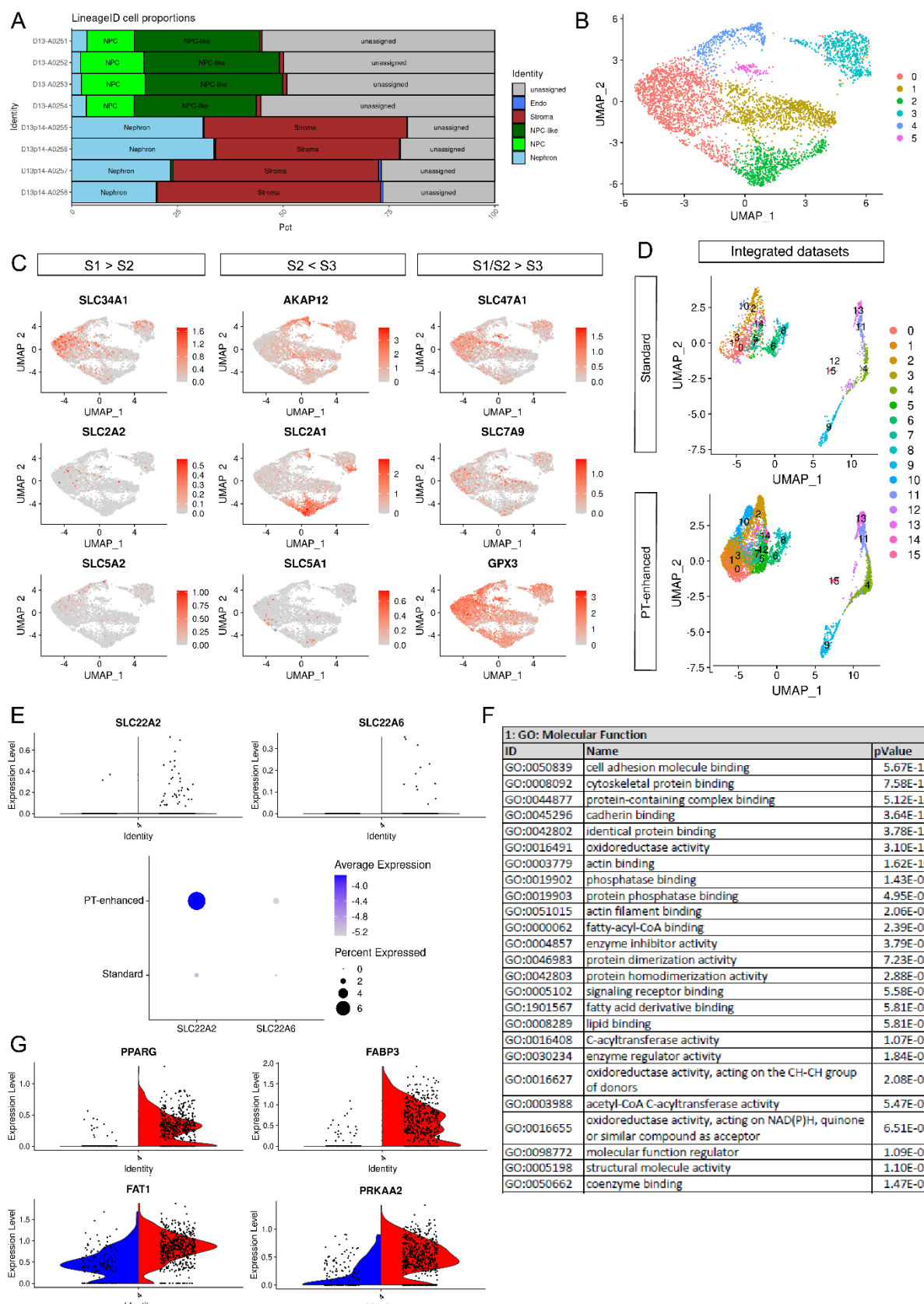
1718



1720 **Supplementary Figure 2: Brush border membrane marker visualisation and scRNaseq**
1721 **cluster marker analyses of D13 monolayers and D13+14 PT-enhanced organoids. A.** High-
1722 resolution confocal microscopy depicting immunofluorescence for apical PT brush border
1723 membrane marker LTL (blue) and SLC6A19 (green) in D7+14 (standard) and D13+14 (PT-
1724 enhanced) organoids. Scale bars represent 20μm. **B.** Dot plot of D13 combined replicate
1725 samples showing expression of early mesenchymal markers preceding metanephric kidney
1726 formation across all resolved clusters. Abbreviations: primitive streak (PS), presomitic
1727 mesoderm (PSM), paraxial mesoderm (PM), lateral plate mesoderm (LPM), intermediate
1728 mesoderm (IM), metanephric mesenchyme (MM), nephron progenitor cells (NPC). **C.** Dotplot
1729 of D13+14 combined replicate samples showing expression of kidney-specific markers across
1730 all resolved clusters. Abbreviations: connecting segments (CNS), loop of Henle (LoH), distal
1731 tubule (DT), proximal tubule (PT), podocyte (Pod), nephron progenitor cell (NPC),
1732 endothelium (End).

1733

1734



1735

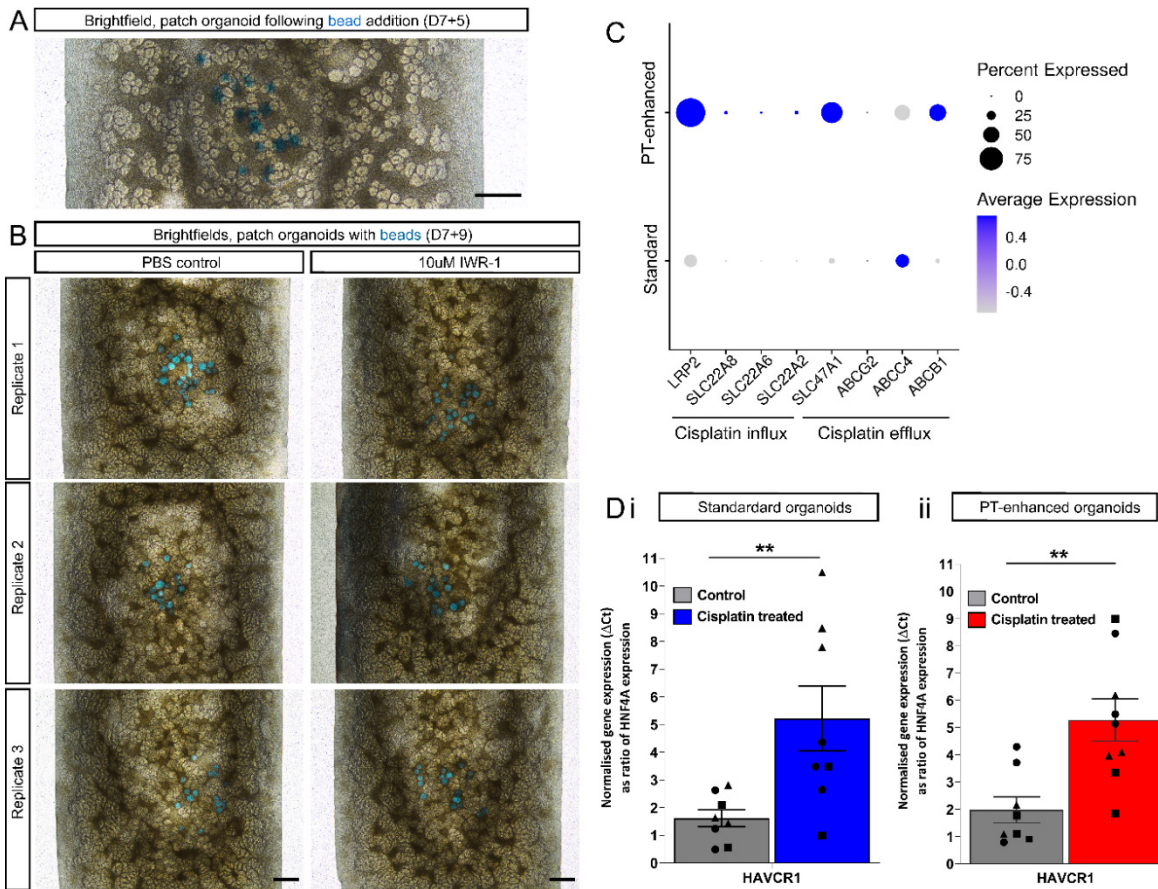
1736 **Supplementary Figure 3: Comparison of D13 monolayer, PT-enhanced organoid, and**
 1737 **published scRNAseq datasets. A. ComparePlot showing proportion of kidney cell types**
 1738 **within each D13 and D13+14 replicate. B. UMAP plot of isolated PT clusters from D13+14**

1739 PT-enhanced organoids, re-clustered to resolve 6 distinct cell populations. **C.** UMAP plots
1740 showing the expression of S1, S2, and S3 segment markers within the isolated PT population
1741 of D13+14 organoids. **D.** UMAP plots from integrated analyses of PT-enhanced organoids and
1742 our existing standard organoid dataset (Howden, *et al.*, 2019) (iPSC line- and age-matched).
1743 Clustering resolved 15 distinct cell populations for each sample in the integrated datasets. **E.**
1744 Violin (top panels) and dot plots (bottom panel) depicting *SLC22A2* and *SLC22A6* expression
1745 within the PT cluster of integrated PT-enhanced and standard organoid datasets from **(D)** (left
1746 and right on violin plots, respectively). **F.** Table depicting top 25 GO terms arising from
1747 unbiased ToppFun GO Molecular Function analyses of significantly differentially expressed
1748 genes between standard (blue, left) and PT-enhanced (red, right) organoid datasets from **(D)**.
1749 **G.** Violin plots comparing examples of genes involved in fatty acid metabolism in standard
1750 (blue, left) and PT-enhanced (red, right) organoid datasets from **(D)**.

1751

1752

1753

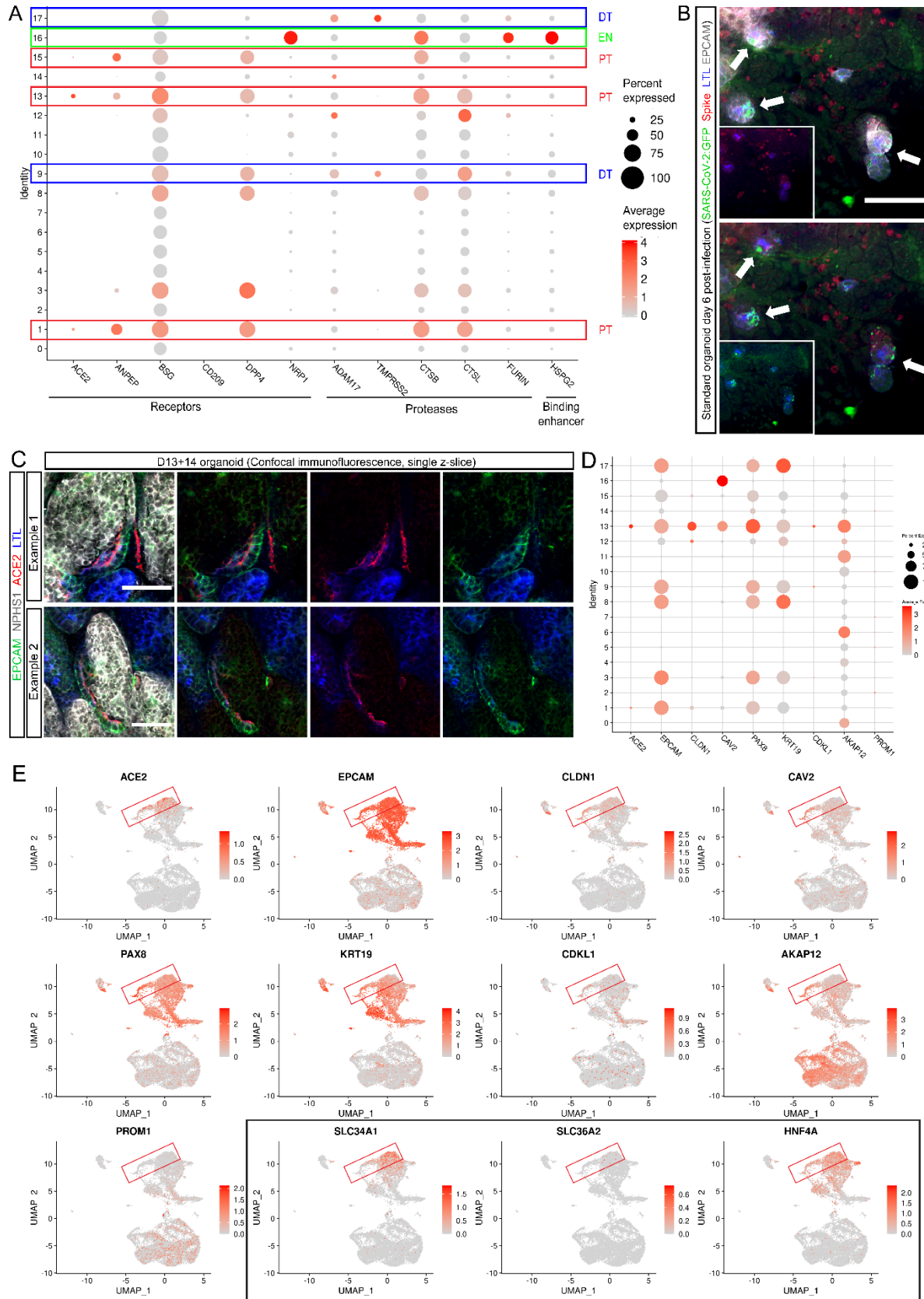


1755 **Supplementary Figure 4: Defining the mechanism of nephron directionality using IWR-
1-soaked agarose beads and exploring PT-enhanced organoid functionality through
cisplatin response.** A. Brightfield image of a D7+5 standard bioprinted patch organoid
1756 immediately after the addition of agarose beads (blue) depicting their contact with forming
1757 renal vesicle structures. Scale bar represents 200 μ m. C. Brightfield images of D7+9 bioprinted
1758 patch organoids containing PSB-soaked or IWR1-soaked (left and right panels, respectively)
1759 beads (blue). Scale bars represent 200 μ m. C. scRNAseq dotplot comparing the expression of
1760 cisplatin influx and efflux transporters within the PT cluster of integrated PT-enhanced and
1761 existing standard organoid datasets (Howden, et al., 2019) (iPSC line- and age-matched). D.
1762 qRT-PCR analyses depicting KIM-1 gene (*HAVCR1*) expression in (i) standard (blue) and (ii)
1763 PT-enhanced (red) organoids treated with cisplatin, compared to their respective PBS-treated
1764 controls (grey). *HAVCR1* gene expression values are normalised to the housekeeping gene
1765 *GAPDH* ($2^{-\Delta Ct}$) and expressed as a ratio of *HNF4A* to compensate for differences in proximal
1766 tubule proportion. Error bars represent SEM from n = 8 (control) and n = 9 (cisplatin-treated)
1767 biological replicates across 3 replicate experiments as indicated. Statistical significance was
1768 determined using an unpaired t test. Asterisks represent P values (**; P ≤ 0.01) adjusted for
1769 multiple comparisons using the Holm-Sidak method alpha = 0.05.

1770

1771

1772

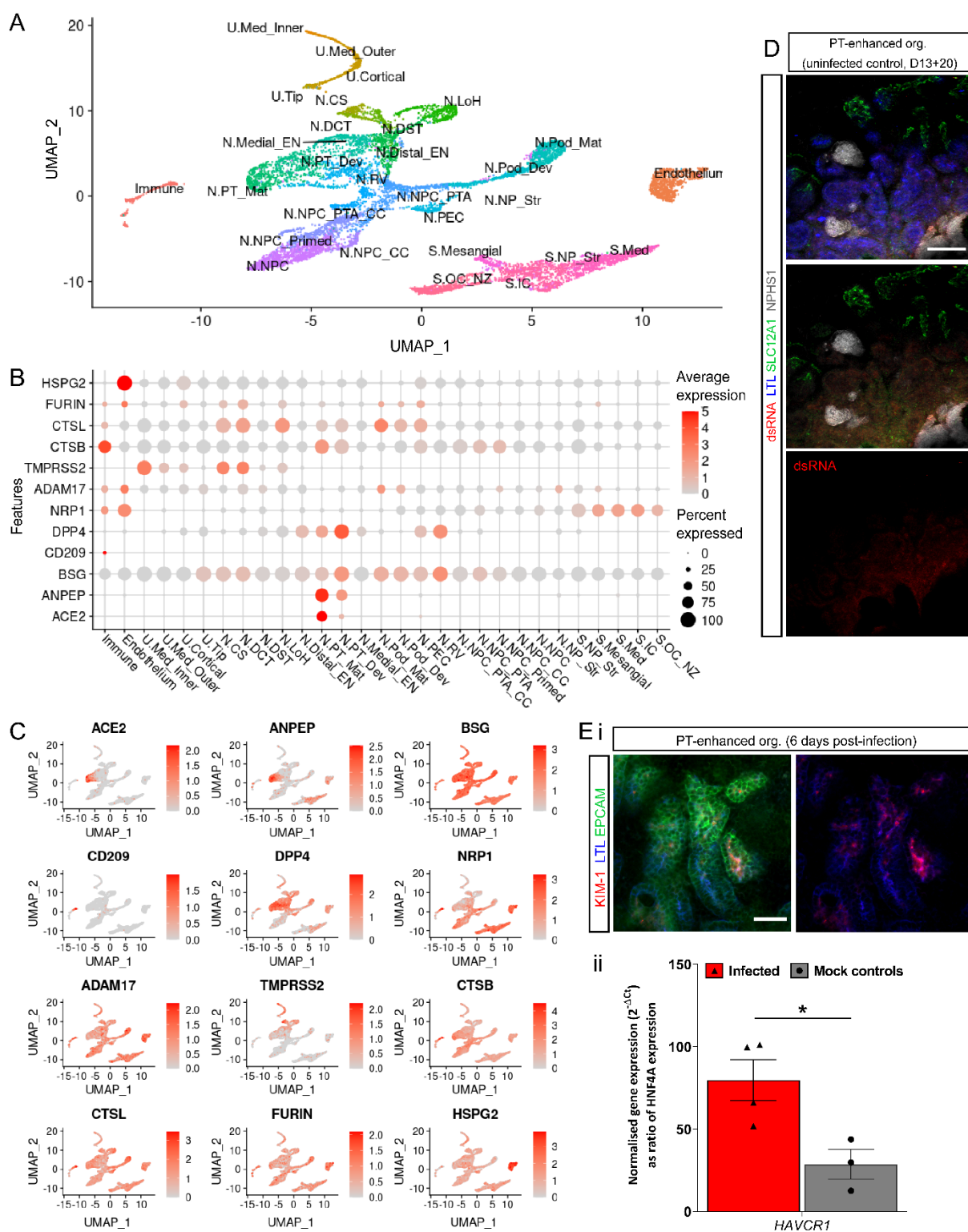


1773

1774

1775 **Supplementary Figure 5: Expression of SARS-CoV-2 entry factors and infectious**
1776 **particles in kidney organoids.** **A.** scRNAseq analysis of SARS-CoV-2 entry factor expression
1777 in D13+14 kidney organoids. Boxes outline proximal (red), distal (blue), and endothelial
1778 (green) clusters. **B.** Confocal immunofluorescence of a D13+20 organoid 6 days post-infection
1779 with GFP-tagged SARS-CoV-2 confirming the presence of GFP-positive (green) and spike
1780 protein-expressing (red) mature and replicating virus within EPCAM⁺/LTL positive (blue) PTs
1781 as well as the interstitium. Insets depict 2-channel overlays of larger merged images. Arrows
1782 indicate examples of viral GFP in LTL-positive tubules Scale bar represents 50μm. **C.**
1783 Confocal immunofluorescence of a D13+14 PT-enhanced organoid depicting apical ACE2
1784 (red) expression on EPCAM-positive (green) cells entering the early portion of Bowman's
1785 capsule surrounding NPHS1-positive (grey) podocytes of glomeruli. LTL (blue) marks PTs.
1786 Scale bars represent 50μm. **D-E.** Analyses of D13+14 scRNAseq dataset displayed as a dot
1787 plot (**D**) and feature plots (**E**), depicting expression of *ACE2* in clusters co-expressing markers
1788 of cuboidal and intermediate PECs, as well S1-specific markers of PT. Boxes in (**E**) highlight
1789 the key region of overlapping expression in the PT clusters.

1790



1791

1792 **Supplementary Figure 6: Distribution of SARS-CoV-2 entry factors in PT-enhanced**
 1793 **kidney organoids. A-C.** Single cell RNAseq analysis of existing week 11 – 18 mixed human
 1794 fetal kidney reference datasets (Hochane, *et al.*, 2019; Tran, *et al.*, 2019; Holloway, *et al.*, 2020)
 1795 displayed in UMAP (A and C) and dot plot (B) formats confirming the resolution of distinct
 1796 kidney cell clusters and the expression of SARS-CoV-2 entry factors within each cluster.

1797 Cluster abbreviations: ureteric (U), medullary (Med), nephron (N), connecting segment (CS),
1798 distal convoluted tubule (DCT), distal straight tubule (DST), loop of Henle (LoH), early
1799 nephron (EN), proximal tubule (PT), developing (Dev), maturing (Mat), podocyte (Pod),
1800 parietal epithelial cell (PEC), renal vesicle (RV), nephron progenitor cell (NPC), pre-tubular
1801 aggregate (PTA), cycling cells (CC), nephron progenitor (NP), stroma (S), stromal (Str), inner
1802 cortical (IC), outer cortical (OC), nephrogenic zone (NZ). **D.** Confocal immunofluorescence of
1803 a representative matched experimental control organoid for SARS-CoV-2 infection
1804 experiments (uninfected D13+20 organoid). Control organoids were stained for viral RNA
1805 (dsRNA; red), PT (LTL; blue), LoH (SLC12A1; green), and podocytes (NPHS1; grey). Scale
1806 bar represents 100µm. **Ei.** Confocal immunofluorescence of a PT-enhanced organoid 6 days
1807 post infection with SARS-CoV-2 depicting KIM-1 (red) expression within EPCAM-
1808 positive/LTL-positive (green/blue) PTs. Scale bar represents 50µm. **Eii.** qRT-PCR analysis
1809 depicting KIM-1 gene (*HAVCR1*) expression in infected (red) and mock control (grey;
1810 uninfected) PT-enhanced kidney organoids at 6 days post-infection. *HAVCR1* gene expression
1811 values are normalised to *GAPDH* housekeeping gene and expressed as a ratio of *HNF4A*
1812 expression to compensate for difference in proximal tubule proportion. Error bars represent
1813 SEM from n = 4 (infected) and n = 3 (mock) biological replicate organoids. Statistical
1814 significance was determined using an unpaired t test. Asterisks represent P values (*; P ≤ 0.05)
1815 adjusted for multiple comparisons using the Holm-Sidak method alpha = 0.05.

1816 **Supplementary Tables**

1817 **Supplementary Table 1:** Differentially expressed (DE) genes by cluster in day 13 (D13)
1818 monolayers derived from extended differentiation in CDBLY2 (see: Vanslambrouck JM et
1819 al_Supplementary Table 1).

1820 **Supplementary Table 2:** Differentially expressed (DE) genes by cluster in D13+14 organoids
1821 derived from D13 monolayers (see: Vanslambrouck JM et al_Supplementary Table 2).

1822 **Supplementary Table 3:** Quantification of nephron structures in organoids exposed to IWR1-
1823 soaked and PBS-soaked agarose beads (see: Vanslambrouck JM et al_Supplementary Table 3).